DTIC FILE COPY

AD-A202 762

(1)

VARIABLE WALL TEMPERATURE EFFECTS

ON MULTICELLULAR NATURAL CONVECTION

IN A HORIZONTAL ANNULUS

THESIS

AFIT/GAE/AA/88D-01

DAVID L. BENNETT

DTIC
ELECTE
JAN 1 8 1989
S D
D

DISTRIBUTION STATEMENT A
Approved for public release;
Distribution Unlimited

DEPARTMENT OF THE AIR FORCE

AIR UNIVERSITY

AIR FORCE INSTITUTE OF TECHNOLOGY

Wright-Patterson Air Force Base, Ohio

89 1 17 015

AFIT/GAE/AA/88D-01

DTIC
ELECTE
JAN 1 8 1989
S D
D

# VARIABLE WALL TEMPERATURE EFFECTS ON MULTICELLULAR NATURAL CONVECTION IN A HORIZONTAL ANNULUS

THESIS

AFIT/GAE/AA/88D-01 DAVID L. BENNETT

Approved for public release; distribution unlimited

AFIT/GAE/AA/88D-01

# VARIABLE WALL TEMPERATURE EFFECTS ON MULTICELLULAR NATURAL CONVECTION IN A HORIZONTAL ANNULUS

THESIS

Presented to the Faculty of the School of Engineering

of the Air Force Institute of Technology

Air University

In Partial Fulfillment of the

Requirements for the Degree of

Master of Science in Aeronautical Engineering

COPY INSPECTED 6

Accesion For
NTIS CRA&I
DTIC TAB
Unannounced
Justification
By
Distribution
Dist
A-1

David L. Bennett, B.S.

Captain, USAF

December 1988

Approved for public release; distribution unlimited

## Preface

The purpose of this thesis was to study the effects of variable inner wall temperature conditions in triggering or suppressing complex multicellular flow fields within a narrow horizontal annulus. Such research has practical applications in technological systems that employ the annular geometry to cool or insulate critical components. Some examples include nuclear reactor design, materials processing, aircraft cabin insulation and pressurized-gas underground electric transmission cables.

In all, ten inner cylinder temperature distributions were examined, offering insight into the nature of complex annular convective flow patterns and the thermal conditions that cause them. Since this research dealt only with low Prandtl-number fluids, follow-on studies of variable Prandtl-number effects should be undertaken to further explore this issue.

In preparing this thesis, I am deeply grateful for the assistance of others who helped see me through this project. I wish to thank my faculty advisor, Capt Daniel B. Fant, whose superb technical expertise in this area filled many gaps and whose dedicated assistance made this effort a valuable learning experience. I also wish to thank the computer science technicians of Systems Research Laboratories for answering all my questions about the ISC computer system. Finally, I want to thank my wife [redacted] for her understanding and support during all those long days and nights I had to spend on the computer.

David L. Bennett

## Table of Contents


| | Page |
|---|---|
| Preface | ii |
| List of Figures | iv |
| List of Symbols | ix |
| Abstract | xiii |
| I. Introduction | 1 |
| Literature Review | 2 |
| II. Mathematical Analysis | 10 |
| The Physical Model | 10 |
| The Dimensional Formulation | 10 |
| The Dimensionless Formulation | 14 |
| III. Analytical Analysis | 20 |
| IV. Numerical Analysis | 30 |
| The Numerical Method | 30 |
| The Computational Procedure | 38 |
| V. Results and Discussion | 42 |
| Inner Cylinder Temperature Distributions | 42 |
| Numerical Results | 44 |
| VI. Conclusions and Recommendations | 85 |
| Appendix A: Supplementary Flow Field Data | 87 |
| Bibliography | 130 |
| Vita | 133 |

## List of Figures


| Figure | | Page |
|---|---|---|
| 1. | 2-D Concentric Cylinder Geometry . . . . . | 11 |
| 2. | Computational Mesh with Variable Increments . . . . . | 32 |
| 3. | Inner Cylinder Temperatur Distributions . . . . . | 43 |
| 4. | Isotherms for $T_I(\psi) = \sin \psi$ . . . . . | 45 |
| 5. | Numerical Streamlines for $T_I(\psi) = \sin \psi$ at $\hat{G} = 4.93$ . . . | 46 |
| 6. | Numerical Streamlines for $T_I(\psi) = \sin \psi$ at $\hat{G} = 4.95$ . . . | 47 |
| 7. | Analytical Streamlines for $T_I(\psi) = \sin \psi$ at $G = 4.95$ . . . | 48 |
| 8. | Angular Variation of the Center-Line Stream Function . . . for $T_I(\psi) = \sin \psi$ at $\hat{G} = 4.93$ | 49 |
| 9. | Radial Variation of Vorticity at 90° for $\hat{G} = 4.93$ . . . . $T_I(\psi) = \sin \psi$ | 50 |
| 10. | Radial Variation of the Stream Function at 90° . . . . . for $\hat{G} = 4.93$, $T(\psi) = \sin \psi$ | 51 |
| 11. | Radial Variation of the Stream Function at 90° . . . . . for $\hat{G} = 4.95$, $T_I(\psi) = \sin \psi$ | 52 |
| 12. | Radial Variation of Vorticity at 90° for $\hat{G} = 4.95$ . . . . $T_I(\psi) = \sin \psi$ | 53 |
| 13. | Angular Variation of the Center-Line Stream Function . . . for $T_I(\psi) = \sin \psi$ at $\hat{G} = 4.95$ | 54 |
| 14. | Isotherms for $T_I(\psi) = -\cos(2\psi)$ . . . . . | 56 |
| 15. | Numerical Streamlines for $T_I(\psi) = -\cos(2\psi)$ at $\hat{G} = 3.0$ . . | 57 |
| 16. | Numerical Streamlines for $T_I(\psi) = -\cos(2\psi)$ . . . . . at $\hat{G} = 4.40$ | 58 |
| 17. | Analytical Streamlines for $T_I(\psi) = -\cos(2\psi)$ . . . . . at $\hat{G} = 4.40$ | 59 |
| 18. | Angular Variation of the Center-Line Stream Function . . . for $T_I(\psi) = -\cos(2\psi)$ at $\hat{G} = 4.40$ | 60 |

19. Radial Variation of Vorticity at 90° for $\hat{G}$ = 4.40 . . . . 61
$T_I(\psi) = -\cos(2\psi)$

20. Radial Variation of the Stream Function at 90° . . . . . 62
for $\hat{G}$ = 4.40 $T_I(\psi) = -\cos(2\psi)$

21. Isotherms for the Triple Hot Spot Distribution . . . . . 64

22. Numerical Streamlines at $\hat{G}$ = 3.0 for the Triple Hot . . . 65
Spot Distribution

23. Numerical Streamlines at $\hat{G}$ = 4.40 for the Triple Hot . . . 66
Spot Distribution

24. Analytical Streamlines at $\hat{G}$ = 4.40 for the Triple Hot . . 67
Spot Distribution

25. Angular Variation of the Center-Line Stream Function . . . 68
at $\hat{G}$ = 4.40 for the Triple Hot Spot Distribution

26. Radial Variation of Vorticity at 90° for $\hat{G}$ = 4.40 . . . . 69
for the Triple Hot Spot Distribution

27. Radial Variation of the Stream Function at 90° . . . . . 70
at $\hat{G}$ = 4.40 for the Triple Hot Spot Distribution

28. Isotherms for the Cold Spot Condition . . . . . 71

29. Numerical Streamlines for the Cold Spot Condition . . . . 72
at $\hat{G}$ = 3.0

30. Numerical Streamlines for the Cold Spot Condition . . . . 73
at $\hat{G}$ = 4.40

31. Analytical Streamlines for the Cold Spot Condition . . . . 74
at $\hat{G}$ = 4.40

32. Angular Variation of the Center-Line Stream Function . . 75
at $\hat{G}$ = 4.40 for the Cold Spot Condition

33. Radial Variation of Vorticity at 90° for $\hat{G}$ = 4.40 for . . 76
the Cold Spot Condition

34. Radial Variation of the Stream Function at 90° . . . . . 77
for $\hat{G}$ = 4.40 for the Cold Spot Condition

35. Unsteady Flow Field at $\hat{t}$ = 200, $\hat{G}$ = 4.99, $T(\psi) = \sin\psi$ . . 81

36. Unsteady Flow Field at $\hat{t}$ = 400, $\hat{G}$ = 4.99, $T(\psi) = \sin\psi$ . . 82

37. Unsteady Flow Field at $\hat{t}$ = 600, $\hat{G}$ = 4.99, $T(\psi) = \sin\psi$ . . 83

38. Unsteady Flow Field at $\hat{t}$ = 800, $\hat{G}$ = 4.99, $T(\psi) = \sin\psi$ . . 84

39. Isotherms for $T_I(\psi) = 1 + \cos\psi$ Imposed on the . . . . . 88
Upper Half-Cylinder

40. Numerical Streamlines for $\hat{G}$ = 3.0, . . . . . 89
$T_I(\psi) = 1 + \cos\psi$ Imposed on the Upper Half Cylinder

41. Numerical Streamlines for $\hat{G}$ = 4.71, . . . . . 90
$T_I(\psi) = 1 + \cos\psi$ Imposed on the Upper Half Cylinder

42. Analytical Streamlines for $\hat{G}$ = 4.71, . . . . . 91
$T_I(\psi) = 1 + \cos\psi$ Imposed on the Upper Half Cylinder

43. Angular Variation of the Center-Line Stream Function . . . 92
at $\hat{G}$ = 4.71 for $T_I(\psi) = 1 + \cos\psi$ Imposed on the Upper
Half-Cylinder

44. Radial Variation of Vorticity at 88° for $\hat{G}$ = 4.71 for . . 93
$T_I(\psi) = 1 + \cos\psi$ Imposed on the Upper Half-Cylinder

45. Radial Variation of the Stream Function at 88° . . . . . 94
for $\hat{G}$ = 4.71 for $T_I(\psi) = 1 + \cos\psi$ Imposed on
the Upper Half-Cylinder

46. Isotherms for $T_I(\psi) = 1 - \cos\psi$ Imposed on . . . . . 95
the Upper Half-Cylinder

47. Numerical Streamlines at $\hat{G}$ = 3.0 . . . . . 96
for $T_I(\psi) = 1 - \cos\psi$ Imposed on the Upper Half-Cylinder

48. Numerical Streamlines at $\hat{G}$ = 4.40 . . . . . 97
for $T_I(\psi) = 1 - \cos(\psi)$ Imposed on the Upper Half-Cylinder

49. Analytical Streamlines at $\hat{G}$ = 4.40 . . . . . 98
for $T_I(\psi) = 1 - \cos\psi$ Imposed on the Upper Half-Cylinder

50. Angular Variation of the Center-Line Stream Function . . . 99
at $\hat{G}$ = 4.40 for $T_I(\psi) = 1 - \cos\psi$ Imposed on the Upper
Half-Cylinder

51. Radial Variation of Vorticity at 120° for $\hat{G}$ = 4.40 for . . 100
$T_I(\psi) = 1 - \cos\psi$ Imposed on the Upper Half-Cylinder

52. Radial Variation of the Stream Function at 120° for . . . 101
$\hat{G}$ = 4.40 for $T_I(\psi) = 1 - \cos\psi$ Imposed on the Upper
Half-Cylinder

53. Isotherms for $T_I(\psi) = \cos \psi$ . . . . . 102

54 Numerical Streamlines for $T_I(\psi) = \cos \psi$ at $\hat{G} = 3.0$ . . . . 103

55. Numerical Streamlines for $T_I(\psi) = \cos \psi$ at $\hat{G} = 5.75$ . . . 104

56. Analytical Streamlines for $T_I(\psi) = \cos \psi$ at $\hat{G} = 5.75$ . . . 105

57. Angular Variation of the Center-Line Stream Function . . . 106
for $\hat{G} = 5.75$, $T_I(\psi) = \cos(\psi)$

58. Radial Variation of Vorticity at 45° for $\hat{G} = 5.75$ . . . . 107
$T_I(\psi) = \cos(\psi)$

59. Radial Variation of the Stream Function at 45° . . . . . 108
for $\hat{G} = 5.75$, $T_I(\psi) = \cos(\psi)$

60. Isotherms for $T_I(\psi) = - \cos \psi$ . . . . . 109

61. Numerical Streamlines for $T_I(\psi) = - \cos(\psi)$ at $\hat{G} = 3.0$ . . 110

62. Numerical Streamlines for $T_I(\psi) = - \cos(\psi)$ at $\hat{G} = 4.40$ . . 111

63. Analytical Streamlines for $T_I(\psi) = - \cos(\psi)$ at $\hat{G} = 4.40$ . 112

64. Angular Variation of the Center-Line Stream Function . . . 113
at $\hat{G} = 4.40$, $T_I(\psi) = - \cos(\psi)$

65. Radial Variation of Vorticity at 315° for $\hat{G} = 4.40$ . . . . 114
$T_I(\psi) = - \cos \psi$

66. Radial Variation of the Stream Function at 315° . . . . . 115
for $\hat{G} = 4.40$, $T_I(\psi) = - \cos \psi$

67. Isotherms for the Single Hot Spot Condition . . . . . 116

68. Numerical Streamlines for $\hat{G} = 3.0$ for the Single Hot . . . 117
Spot Condition

69. Numerical Streamlines for $\hat{G} = 4.40$ for the Single Hot . . 118
Spot Condition

70. Analytical Streamlines for $\hat{G} = 4.40$ for the Single . . . . 119
Hot Spot Condition

71. Angular Variation of the Center-Line Stream Function . . . 120
for $\hat{G} = 4.40$ for the Single Hot Spot Condition

72. Radial Variation of Vorticity at 90° for $\hat{G} = 4.40$ . . . . 121
for the Single Hot Spot Condition

73. Radial Variation of the Stream Function at 90° for . . . . 122
$\hat{G}$ = 4.40 for the Single Hot Spot Condition

74. Isotherms for the Dual Hot Spot Condition . . . . . 123

75. Numerical Streamlines for $\hat{G}$ = 3.0 for the Dual Hot . . . . 124
Spot Condition

76. Numerical Streamlines for $\hat{G}$ = 4.40 for the Dual Hot . . . 125
Spot Condition

77. Analytical Streamlines for $\hat{G}$ = 4.40 for the Dual . . . . . 126
Spot Condition

78. Angular Variation of the Center-Line Stream Function . . . 127
for $\hat{G}$ = 4.40 for the Dual Hot Spot Condition

79. Radial Variation of Vorticity at 90° for $\hat{G}$ = 4.40 . . . . 128
for the Dual Hot Spot Condition

80. Radial Variation of the Stream Function at 90° for . . . . 129
$\hat{G}$ = 4.40 for the Dual Hot Spot Condition

## List of Symbols

| | |
|---|---|
| $a$ | Inner cylinder radius |
| $b$ | Outer cylinder radius |
| $\hat{e}_r$ | Radial unit vector |
| $\hat{e}_\psi$ | Angular unit vector |
| $f$ | $\frac{\bar{f}}{\nu}$, dimensionless stream function in N-S equations |
| $\tilde{f}$ | Dimensionless stream function in finite-Pr boundary- |
| $F$ | Dimensionless stream function in zero-Pr boundary-layer |
| $\bar{F}$ | Dimensional body force term |
| $g$ | Acceleration of gravity |
| $G$ | $\frac{b-a}{a}$, dimensionless gap number in N-S equations |
| $\tilde{G}$ | $Ra^{1/4}$ G, dimensionless scaled gap number in finite-Pr boundary-layer equations |
| $\hat{G}$ | $(\frac{Ra}{Pr})^{1/4}$ G, dimensionless scaled gap number in zero-Pr boundary-layer equations |
| $H$ | $h_f/h_b$, radial icrement ratio |
| $h_b, h_f$. | Variable radial increments |
| $k_b, k_{b1}, k_f, k_{f1}$ | Variable angular increments |
| NR | Number of nodes in radial direction |
| NS | Number of nodes in angular direction |
| P,Q | Dummy variables |
| Pr | $\nu/\alpha$, Prandtl number |
| $r$ | $\frac{\bar{r}-a}{b-a}$, dimensionless radial coordinate |

| | |
|---|---|
| Ra | $\frac{g\beta a^3\left[T_I(\psi) - T_0\right]}{\nu\alpha}$, Rayleigh number based on the inner radius, a |
| S | Source term in numerical method |
| t | $\bar{t}\,\frac{\nu}{a^2}$, dimensionless radial coordinate |
| $\tilde{t}$ | $Ra^{1/2}t$, dimensionless scaled time in finite-Pr boundary-layer equations |
| $\hat{t}$ | $(\frac{Ra}{Pr})^{1/2}$, dimensionless scaled time in zero-Pr boundary-layer equations |
| T | $\frac{\bar{T} - T_o}{T_i - T_o}$, dimensionless temperature in N-S equations |
| $\tilde{T}$ | Dimensionless temperature in finite-Pr boundary-layer equations |
| $T_i$ | Inner cylinder temperature |
| $T_o$ | Outer cylinder temperature |
| $T_I(\psi)$ | Variable inner cylinder temperature |
| u | $\bar{u}(\frac{a}{\nu}) = \frac{-1}{G(r + \frac{1}{G})}\frac{\partial f}{\partial \psi}$, dimensionless radial velocity |
| $\tilde{u}$ | Dimensionless radial velocity in finite-Pr boundary-layer equations |
| v | $\bar{v}(\frac{a}{\nu}) = \frac{1}{G}\frac{\partial f}{\partial r}$, dimensionless angular velocity in N-S equations |
| $\tilde{v}$ | Dimensionless angular velocity in finite-Pr boundary-layer equations |
| w | $\bar{w}(\frac{a^2}{\nu})$, dimensionless vorticity in N-S equations |

| | |
|---|---|
| $\tilde{W}$ | Dimensionless vorticity in finite-Pr boundary-layer equations |
| $W$ | Dimensionless vorticity in zero-Pr boundary-layer equations |

Greek symbols

| | |
|---|---|
| $\alpha$ | $\frac{k}{\rho c}$, thermal diffusivity |
| $\beta$ | Coefficient of thermal expansion |
| $\delta$ | Boundary-layer thickness |
| $\epsilon$ | Convergence criterion, or dimensionless eccentricity variable |
| $\lambda$ | Parameter in finite-difference equations |
| $\mu$ | Dynamic viscosity, or parameter in finite-difference equation |
| $\nu$ | $\frac{\mu}{\rho}$, momentum diffusivity |
| $\psi$ | $\bar{\psi}$, dimensionless angular coordinate |
| $\rho$ | Density |
| $\tau$ | Time increment in numerical method |
| $\phi$ | Arbitrary dependent variable |
| $\Gamma$ | Parameter in finite-difference equations |
| $\Omega_1, \Omega_2$ | Relaxation parameters in numerical method |
| $\bar{\nabla}$ | Gradient differential operator |
| $\nabla 1, \nabla 2, \tilde{\nabla}$ | Parameters in finite-difference equations |
| $\nabla^2, \nabla_2^2$ | Second-order differential operators |

Superscripts

| | |
|---|---|
| m | Iteration number |

| | |
|---|---|
| n | Time level |

<u>Subscripts</u>

| | |
|---|---|
| i | Radial position, or heated inner cylinder surface |
| j | Angular position |
| o | Outer cylinder surface |
| 0,1,...,10,12 | Node position in computational molecule |

## Abstract

The purpose of this study was to examine natural convection within a narrow horizontal annulus subject to variable inner cylinder temperature distributions. Both numerical and analytical approaches were taken in determining the effects of variable temperature conditions imposed on the inner cylinder in triggering or suppressing multicellular flow instabilities.

The two-dimensional Navier-Stokes equations are simplified into boundary-layer equations for the assumptions of large Rayleigh number, small annular gap, and small Prandtl number. These 2-D unsteady boundary-layer equations are discretized using finite-differencing techniques. Numerical solutions to these governing equations are then obtained by using a stable second-order, fully-implicit, time-accurate, Gauss-Siedel iterative procedure.

In addition, analytical steady-state solutions to these simplified equations are obtained using perturbation methods. For most inner cylinder temperature distributions considered in the steady flow regime, these analytical results yield excellent agreement with numerical results. Although both schemes predict the formation of thermal-like instabilities induced by localized hot and cold spots in the horizontal annular regions, the analytical model failed to predict the steady-state multicellular hydrodynamic instabilities found numerically for the sin $\psi$ temperature distribution at $\hat{G} = 4.95$ in the vertical portions of the

annulus. The analytical model also fails to capture unsteady multicellullar flow behavior found numerically for the sinusoidal temperature distribution at $\hat{G} = 4.99$. Limited unsteady numerical results for this test case indicated oscillatory behavior in the strength of this flow field.

# VARIABLE WALL TEMPERATURE EFFECTS ON MULTICELLULAR NATURAL CONVECTION IN A HORIZONTAL ANNULUS

## I. Introduction

The study of natural convection in concentric cylindrical annuli receives considerable attention from researchers due to its practical applications in the areas of nuclear reactor design, aircraft cabin insulation, cooling of electronic equipment, thermal storage systems, and material processing. The horizontal concentric cylinder geometry is used in pressurized-gas underground electric transmission cables (Kuehn and Goldstein, 1975).

The purpose of this study was to examine the effects of variable wall temperature conditions on natural convective flows in a narrow horizontal annulus. Of particular interest is the effects of variable inner-cylinder wall temperature distributions in suppressing or triggering hydrodynamic instabilities that give rise to the formation of convective cell patterns within the annulus. Understanding the boundary conditions that give rise to these multicellular flow fields is important, since convective cells are the primary cooling mechanism for the annular geometry. Such knowledge may aid in the design of efficient concentric-cylinder cooling devices or related technological systems.

This thesis involves two approaches in accomplishing the stated objective.

First, the 2-D Navier-Stokes equations are simplified into

boundary-layer equations for the conditions of large Rayleigh number, small annular gap, and small Prandtl number. These 2-D unsteady boundary-layer equations are discretized using finite-differencing techniques. The governing equations in discretized form are then solved using the AFIT VAX 8650 computer system to obtain the flow field.

The second approach involves determining analytical steady-state solutions to these simplified equations using perturbation methods. These solutions serve to support and compare related numerical results.

Before beginning a detailed discussion of these topics, a review of the related literature is presented to examine recent work in this area of study. Chapters II - IV discuss the background theory and analysis of this problem, and Chapters V and VI present the key results and conclusions.

## Literature Review

The natural convection of flow between horizontal concentric cylinders has been the subject of many investigations. In most of these, the focus has been on numerical studies of fluids with low Rayleigh numbers or high Prandtl numbers of order 1 or larger that show close agreement with experimental work. The convective behavior of low Prandtl number fluids such as liquid metals has received little attention. These fluids are often used as the working fluid in several powergenerating cycles due to their excellent heat-transfer characteristics.

This thesis considers natural convection of high Rayleigh number/low Prandtl number fluids in a narrow horizontal annulus with variable temperature distributions imposed on the inner cylinder wall. By

contrast, most recent work deals with isothermal boundary conditions, with numerical work incorporating variable temperature effects nearly nonexistent. Analytical approaches in modeling this flow regime are equally rare.

This literature review covers three main topics; the analytical approaches, the numerical studies, and the experimental analyses.

Analytical Studies. Only two analytical studies of natural convection of low Prandtl-number fluids between concentric cylinders were found. Both used perturbation methods to model high Rayleigh number flow fields within the annulus.

Using the assumption of small annular gap width, Fant (1987), derived a three-term perturbation expansion to obtain steady-state solutions for the high Rayleigh number/low Prandtl number flow regime. He obtained stream function and vorticity solutions that agreed well with pretransitional numerical flow-field results. Since this thesis adopts both his analytical and numerical methods, discussion is deferred to the next three chapters for a detailed treatment of this procedure.

Custer and Shaughnessy (1977) studied natural convection of low Prandtl-number fluids within a horizontal annulus by solving the dimensionless thermal energy and vorticity equations with a double perturbation expansion in powers of Grashof and Prandtl numbers. The temperature and stream function expansions were as follows:

$$T(r,\theta) = \sum_{j=0}^{\infty} \sum_{k=0}^{\infty} Pr^{j}\, Gr_{r_0}^{k}\, T_{jk}(r,\theta) \qquad (1.1a)$$

$$\psi(r,\theta) = \sum_{n=0}^{\infty} \sum_{m=0}^{\infty} Pr^n \, Gr_{r_0}^m \, \psi_{nm}(r,\theta) \quad . \tag{1.1b}$$

The authors described the evolution of the flow for several radius ratios, where in both cases the flow was composed of a single eddy in each half-annulus for low Grashof number. As Grashof number was increased, they observed that the eddy in high Prandtl-number fluids fell, while the eddy in low Prandtl number fluids rose. Custer and Shaughnessy indicated that only further experimental and numerical studies of the unsteady flow regime could resolve multicellular flow behavior.

Numerical Studies. As previously stated, the majority of the numerical studies of natural convection in horizontal annuli have dealt with low Rayleigh-number/high Prandl-number flows under isothermal boundary conditions. Special emphasis shall be placed on the formation and nature of multicellular flow fields and the numerical schemes which were used to model them.

Charrier-Mojtabi et al. (1978) studied natural convection flows between two horizontal concentric annuli with constant surface temperatures. They solved the problem using an implicit alternating direction scheme with a vorticity and stream function formulation. Rayleigh numbers varying between $10^2$ and $5 \times 10^4$, radius ratios between 1.2 and 5 and Prandtl numbers of 0.7 and 0.02 were examined. For R = 1.2 and Rayleigh numbers of 6000 and 7000, no multicellular flow fields resulted using air as the fluid (Pr = 0.7). However, for Pr = 0.02 and R = 2, the flow regime became multicellular for large Rayleigh numbers and began to oscillate, as the flow became unsteady.

Rao et al. (1985) studied flow patterns of natural convection in horizontal cylindrical annuli. They used an unsteady formulation of the 2-D energy and vorticity-stream function equations which were solved by using an ADI scheme with central-differencing. A radius ratio of 1.175 and a Rayleigh number of 4,000 resulted in the formation of two small counter-rotating cells just above the main kidney-shaped cells in the upper annulus. Their results contrast with those obtained by Charrier-Mojtabi et al. using the ADI method, who failed to achieve multicellular flow patterns in their study of narrow-gap geometries.

Date (1985) studied natural convection in a horizontal annular gap in which the isothermal inner cylinder was hotter than the cool outer cylinder. His numerical prediction scheme involved solving the governing equations for the primitive variables of pressure, velocities and temperatures. This is in contrast to most other numerical schemes which use the stream function-vorticity equations to generate solutions. His numerical predictions for natural convection heat transfer for a gap width/internal diameter ($L/D_i$) ratio of 0.15 for air compare poorly with computed heat transfer rates of Boyd (1981) and Grigull and Hauf (1966).

Farouk and Guceri (1981) examined both laminar and turbulent natural convection between horizontal concentric cylinders held at constant temperatures. Solutions for the laminar flow case were obtained up to a Rayleigh number (based on gap width) of $10^5$. Turbulent flow results were obtained for Rayleigh numbers of $10^6$ - $10^7$. For the laminar case, the 2-D elliptic partial differential equations of vorticity, stream function, and temperature with specified boundary conditions were solved. An outside-to-inside diameter ratio of 2.6 was used with air in the

numerical formulation. For these conditions, the typical crescent-shaped cellular pattern emerged which has been found in previous studies. Similar fluid circulation patterns were obtained in the turbulent studies. However, the location of maximum stream function was found to move upward.

Kumar (1988) investigated natural convection in horizontal annuli for a wide range of Rayleigh numbers extending from conduction to the convection-dominated steady flow regime for diameter ratios of 1.2 - 10. Here, the inner cylinder is heated by a constant heat flux and the outer cylinder is isothermally cooled. As found by other researchers, a crescent-shaped eddy dominated for the small diameter ratioo, while a kidney-shaped flow pattern emerged for a diameter ratio of 5. At high Rayleigh numbers, as the diameter ratio is increased, more stagnant fluid exists at the bottom of the annulus coincident with the prescence of the kidney-shaped flow pattern.

Fusegi and Farouk (1986) conducted a three-dimensional analysis for natural convective flows of air in an annulus having differentially heated concentric isothermal horizontal cylinders using the vorticity-velocity formulation. The Rayleigh numbers used were $10^3$ and $10^4$. The ratio of the gap width to the inner cylinder radius studied was 1.6. The authors pointed out that 3-D numerical solutions were better suited for modeling convective flow fields since 2-D numerical studies could not capture all the important flow characteristics of a confined fluid. Flow field results were graphically compared for both cases. Radial velocity plots at $\phi = 180^\circ$ indicated that the 3-D flow motion is much more vigorous than the 2-D case due to the formation of a

three-dimensional plume in this annular region. This was but one phenomenon Fusegi and Farouk contended that the 2-D solutions overlooked.

Kumar and Keyhani (1988) obtained detailed numerical results of natural convection in a horizontal annulus with a constant heat flux enforced on the inner cylinder and an isothermal outer wall. Prandtl numbers studied were 0.7, 5.0 and 100 for radius ratios of $1,8 \leq R \leq 15$. The Navier-Stokes equations were recast as vorticity-stream function equations. The vorticity transport equation and the energy equation were solved using the false transient Alternating Direction Implicit (ADI) method, and the stream function equation was solved by the successive over-relaxation (SOR) method. Prandtl number effects on flow field characteristics in horizontal annuli were found to be insignificant for $Pr > 0.7$ for the range of radius ratios studied. The results also indicated that the important flow parameter for heat transfer due to convection only is the conventional Rayleigh number.

Experimental Studies. Although many articles on experimental studies of natural convection within enclosures exist in the literature, only those that deal with the concentric cylinder geometry are discussed below. As with numerical studies of this problem, experimental work has dealt mainly with the isothermal condition imposed on the annulus, while variable inner cylinder wall temperature conditions are scarce or nonexistent.

Kuehn and Goldstein (1976) performed an experimental and numerical study of natural convection within horizontal concentric cylinders. The experimental results were obtained using a Mach-Zehnder interferometer to visualize the temperature field in the enclosure which can be analyzed to

determine the local heat flux. The flow field is assumed steady with no axial variation in properties, except for end effects. The cylinders had an annular gap width/inner cylinder diameter of 0.8. Two sets of experimental runs were made; one with air, the other using water.

Quantities obtained experimentally included temperature distributions and local and averaged heat-transfer coefficients. The numerical solutions confirmed these experimental results, and provided the related velocity distributions and extended the results to lower Rayleigh numbers. The temperature distributions for both air and water were nearly identical at similar Rayleigh numbers. The flow was steady for all Rayleigh numbers investigated ($Ra \leq 10^5$).

Kuehn and Goldstein (1978) later examined the effects of eccentricity and Rayleigh number on natural convection heat transfer through a horizontal cylindrical annulus. They found that eccentricity of the inner cylinder caused large changes in the local heat transfer on both cylinders, but the overall heat transfer coefficient for an eccentric geometry is within 10 percent of that for the concentric case at the same Rayleigh number. At large Rayleigh numbers, the flow was observed to become unsteady first in the plume above the inner cylinder. This unsteadiness was seen to increase as the Rayleigh number was increased. This turbulence rapidly decayed as the flow moved downward along the outer cylinder such that the bottom half of the annulus remained virtually steady. Hence, laminar and turbulent flows were seen to exist in the annulus at the same time.

Sun and Zhang (1986) made an experimental study of natural convection heat transfer in concentric and eccentric horizontal

cylindrical enclosures. They employed a Mach-Zehnder interferometer to gauge the temperature distribution within the annulus. The objective of this study was to determine the effect of the diameter ratio K and the eccentricity $\varepsilon$ on the heat transfer in the horizontal cylindrical annulus. Experiments were performed using air at atmospheric pressure with radius ratios K varying from 1.77 to 2.68 and eccentricities from -0.50 to 0.35.

The local and overall heat transfer coefficients were obtained by analyzing the interferograms over a range of Grashof numbers from $4.6 \times 10^2$ to $3.8 \times 10^4$. The shape of the interferometer fringes indicated that the thermal boundary layer for air formed around the inner cylinder and partly at the upper surface of the outer cylinders. For the case of $\varepsilon = -0.5$, temperature inversion and thermal boundary-layer separation effects were strongest in the upper portion of the annuli, and to a lesser degree for $\varepsilon = 0$ and $\varepsilon = 0.353$. The stagnation zone at the annulus bottom decreased when $\varepsilon$ increased from negative to positive values. The thermal plume formed over the top of the inner cylinder became more prominent with increasing eccentricity, since there was more space and less flow resistance in the upper portion of the annulus.

Rao et al. (1985) experimentally obtained results for steady 3-D natural convection in a horizontal cylindrical annulus. The objective was to confirm the complex structure of the 3-D numerical results obtained by the authors of this paper. Flow patterns were examined for the large Rayleigh number/large Prandtl number regime. An increase in the number of cells observed with increasing Ra confirmed numerical studies of similar flows.

# II. Mathematical Analysis

In this chapter, a vorticity-stream function formulation of the Navier-Stokes equations is described in dimensionless form (based on Fant, 1987). By using this approach, the pressure terms are completely eliminated while automatically satisfying the conservation of mass principle. In addition, the resulting stream function and vorticity contours are useful for visualizing and analyzing the flow field. The dimensionless equations in final form are given in Eqs (2.26 to 2.28).

## The Physical Model

a. The flow is unsteady and two-dimensional (see Figure 2.1).

b. The fluid is initially at rest.

c. The cylinders are assumed horizontal with an isothermal outer cylinder and a variable temperature distribution imposed on the inner cylinder.

d. Laminar fluid motion is induced by buoyancy effects. The fluid is Newtonian.

e. All material properties are assumed constant. Density variations are allowed to occur via the Boussinesq approximation.

## The Dimensional Formulation

Governing Equations Using the Stream Function-Vorticity Approach. The vorticity-transport equation is derived by taking the curl of the Navier-Stokes equations. This equation can be written as:

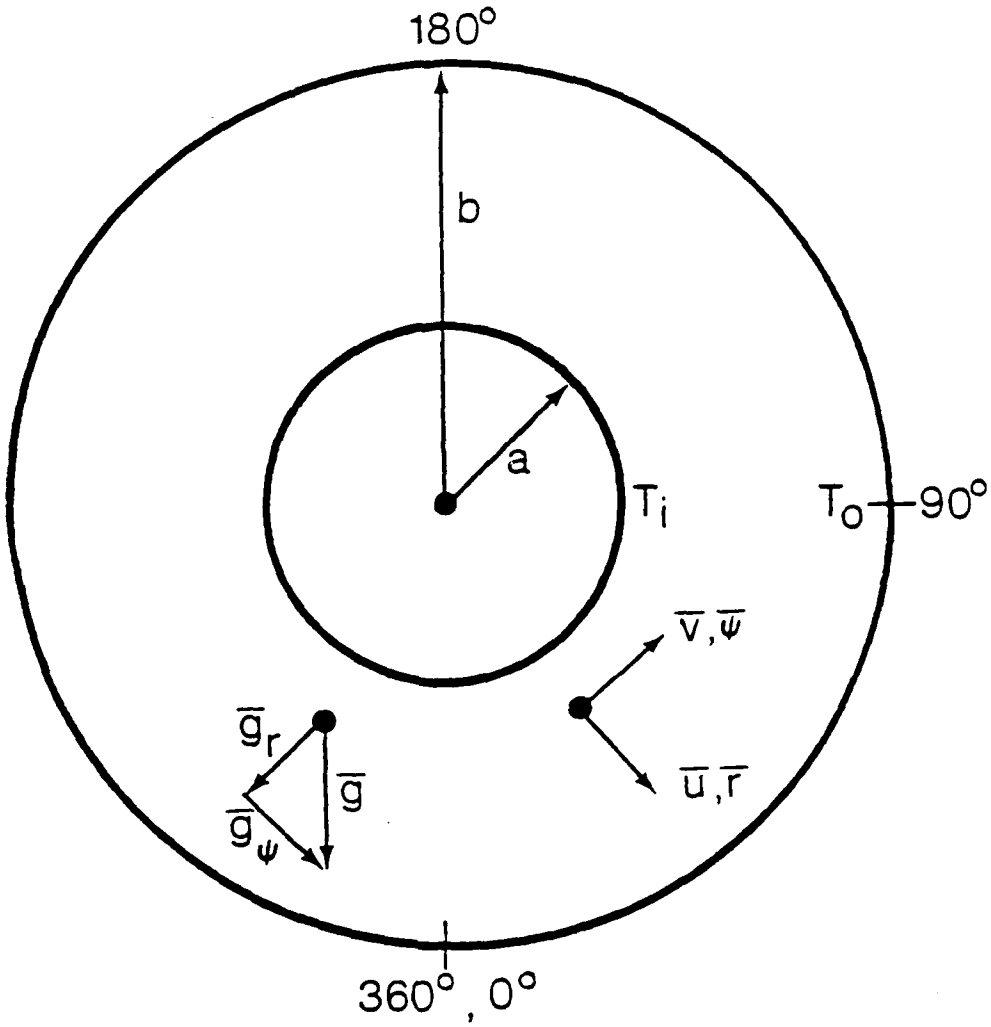


Figure 2.1. 2-D concentric cylinder geometry

$$\frac{\partial \bar{w}}{\partial \bar{t}} + (\bar{v} \cdot \bar{\nabla})\bar{w} = (\bar{w} \cdot \bar{\nabla})\bar{v} + \nu\nabla^2\bar{w} + \bar{\nabla} \times \bar{F}_B \tag{2.1}$$

The bar over the variables signifies dimensional quantities. $\bar{w}$ and $\bar{v}$ represent the vorticity and velocity vectors, respectively. The left side of this equation desribes the total rate change of particle vorticity. The term $(\bar{w} \cdot \bar{\nabla})\bar{v}$ is identically zero for 2-D flows due to the vorticity vector always being perpendicular to the plane of flow. The term $\nu\nabla^2\bar{w}$ represents the net rate of vorticity diffusion due to viscous effects. The last term, $\bar{\nabla} \times \bar{F}_B$, is the rate of internal vorticity generation due to body forces, resulting from large density perturbations in natural convective flows. The fact that pressure does not appear explicitly in Eq (2.1) enables the determination of the vorticity and stream function (velocity) fields without prior knowledge of the pressure distribution. Using the Boussinesq approximation for the net body force:

$$-g\beta(\bar{T} - T_0)\hat{j} = -g\beta(\bar{T} - T_0)\cos\psi\,\hat{e}_r + g\beta(\bar{T} - T_0)\sin\psi\,\hat{e}_\psi \tag{2.2}$$

where $\beta$ is the coefficient of thermal expansion. The final form of the vorticity-transport equation is:

$$\frac{\partial \bar{w}}{\partial \bar{t}} + \frac{1}{\bar{r}}\frac{\partial(\bar{f},\bar{w})}{\partial(\bar{r},\bar{\psi})} = g\beta\left[\sin\bar{\psi}\frac{\partial \bar{T}}{\partial \bar{r}} + \frac{\cos\bar{\psi}}{\bar{r}}\frac{\partial \bar{T}}{\partial \bar{\psi}}\right] + \nu\nabla^2\bar{w} \tag{2.3}$$

and the thermal-energy and stream function equations are:

$$\frac{\partial \bar{T}}{\partial \bar{t}} + \frac{1}{\bar{r}}\frac{\partial(\bar{f},\bar{T})}{\partial(\bar{r},\bar{\psi})} = \alpha\nabla^2\bar{T} \tag{2.4}$$

and

$$\bar{w} = \nabla^2\bar{f} \quad . \tag{2.5}$$

In the above equations, $\bar{r}$ and $\bar{\psi}$ represent the radial and angular coordinates. $\bar{T}$ is the temperature and $\bar{t}$ denotes time. $\nu$ and $\alpha$ denote the momentum and thermal diffusivities, respectively. The radial velocity, $\bar{u}$, and the angular velocity, $\bar{v}$, have been written in terms of the stream function, $\bar{f}$, defined as:

$$\bar{u} = \frac{-1}{\bar{r}} \frac{\partial \bar{f}}{\partial \bar{\psi}} \quad \text{and} \quad \bar{v} = \frac{\partial \bar{f}}{\partial \bar{r}} \quad . \tag{2.6}$$

The number of dependent variables has now been reduced by one. The convective terms are then given in terms of the Jacobian, $\partial(P,Q)/\partial(x,y)$, where

$$\frac{\partial(P,Q)}{\partial(x,y)} = \frac{\partial P}{\partial x}\frac{\partial Q}{\partial y} - \frac{\partial P}{\partial y}\frac{\partial Q}{\partial x} \quad . \tag{2.7}$$

The three coupled governing equations (2.3, 2.4 and 2.5) describe the vorticity, temperature and stream function for the horizontal annulus.

<u>Boundary Conditions</u>. For temperature boundary conditions, the outer cylinder is assumed to be isothermal, while the inner cylinder has a variable temperature distribution that is a function of the angular position.

$$\bar{T} = T_I(\bar{\psi}) \quad \text{at} \quad \bar{r} = a$$

and

$$\bar{T} = T_0 \quad \text{at} \quad \bar{r} = b \quad . \tag{2.8}$$

Both $\bar{u}$ and $\bar{v}$ are identically zero at both cylinder walls due to the no-slip condition, yielding the boundary conditions:

$$\bar{f} = 0, \quad \bar{w} = \frac{\partial^2 \bar{f}}{\partial \bar{r}^2} \quad \text{at } \bar{r} = a \text{ and } \bar{r} = b. \tag{2.9}$$

To ensure a computational continuous condition in the complete annulus (0 - $2\pi$) the following boundary conditions (in $\bar{\psi}$) are enforced at zero and $2\pi$ radians:

$$\phi = \phi_{2\pi}$$

and

$$\left.\frac{\partial \phi}{\partial \bar{\psi}}\right|_0 = \left.\frac{\partial \phi}{\partial \bar{\psi}}\right|_{2\pi} \quad \text{for } a \le \bar{r} \le b, \tag{2.10}$$

where $\phi$ represents the dependent variable for temperature, vorticity, or stream function.

<u>Initial Conditions</u>. Since there is no fluid motion initially,

$$\bar{f} = \bar{w} = 0 \text{ and } \bar{T} = T_0 \tag{2.11}$$

*throughout the annulus*, except at the walls where:

$$\bar{T} = T_I(\bar{\psi}) \text{ and } \bar{T} = T_0 \tag{2.12}$$

is enforced at $\bar{r}$ = a and b, respectively.

## The Dimensionless Formulation

Casting equations in dimensionless form has several advantages. First, it transforms the mathematical or numerical results into a simpler form, allowing for better graphical interpretation. Secondly, measurement scales are no longer an intrinsic part of the physical quantities, therefore, any laws governing physical variables are valid for all different measurement systems (Fant, 1987). Finally, when a problem is nondimensionalized, fewer variables are used and the proper dimensionless groups characterizing a particular flow model are usually

brought forth.

Coordinate Transformation. The radial coordinate is nondimensionalized so that the outer boundary at $\bar{r} = b$ is transformed into the unit circle, $r = 1$. The inner boundary, $\bar{r} = a$, is transformed into the pole, $r = 0$. The following coordinate transformation results:

$$r = \frac{\bar{r} - a}{b - a}, \quad \psi = \bar{\psi} \quad . \tag{2.13}$$

The other independent variable, time, scales as

$$t = \frac{\bar{t}\nu}{a^2} \quad . \tag{2.14}$$

Governing Equations. The remaining dependent variables can now be scaled to produce the following:

$$T = \frac{\bar{T} - T_0}{T_I(\psi) - T_0} \qquad \text{(temperature)} \tag{2.15}$$

$$w = \frac{\bar{w}a^2}{\nu} \qquad \text{(vorticity)} \tag{2.16}$$

$$f = \frac{\bar{f}}{\nu} \qquad \text{(stream function)} \tag{2.17}$$

Eqs (2.13 to 2.17) are now substituted into Eqs (2.3 to 2.5) resulting in the following nondimensional governing equations:

$$Pr \left\{ G^2 \frac{\partial w}{\partial t} + \left[ r + \frac{1}{G} \right]^{-1} \frac{\partial(f,w)}{\partial(r,\psi)} \right\} = Pr \cdot \nabla_2^2 w$$

$$+ G \cdot Ra \left\{ \sin\psi \frac{\partial T}{\partial r} + \cos\psi \left[ r + \frac{1}{G} \right]^{-1} \frac{\partial T}{\partial \psi} \right\} \tag{2.18}$$

$$G^2 \frac{\partial T}{\partial t} + \left[ r + \frac{1}{G} \right]^{-1} \frac{\partial(f,T)}{\partial(r,\psi)} = \frac{1}{Pr} \left[ \nabla_2^2 T \right] \tag{2.19}$$

$$\nabla_2^2 = G^2 w \tag{2.20}$$

where

$$\nabla_2^2 = \frac{\partial^2}{\partial r^2} + \left[ r + \frac{1}{G} \right]^{-1} \frac{\partial}{\partial r} + \left[ r + \frac{1}{G} \right]^{-2} \frac{\partial^2}{\partial \psi^2} \ .$$

Also,

$$Pr = \frac{\nu}{\alpha} \qquad \text{(Prandtl number)} \tag{2.21}$$

$$Ra = \frac{g\beta a^3 \left[ T_I - T_o \right]}{\nu\alpha} \qquad \text{(Rayleigh number based on the inner radius, a)} \tag{2.22}$$

and

$$G = \frac{b - a}{a} \qquad \text{(gap number)} \ . \tag{2.23}$$

The three dimensionless parameters that arise from this analysis are G, Pr and Ra. These key variables are used to simulate various flow conditions and geometries. The magnitude of the Rayleigh number reflects the ratio of destabilizing buoyant forces to the more stabilizing viscous forces. It also predicts the onset of thermal and/or hydrodynamic instability. The Prandtl number characterizes the fluid and the gap number defines the annular geometry.

In deriving Eqs (2.18 to 2.20), the variables w, f and t are non-dimensionalized with $\nu$ instead of $\alpha$. This was done in order to reflect a thermal-diffusion dominated energy equation for small Prandtl

numbers, which was the focus of this study. For further details on this procedure see Fant (1987).

In Eqs (2.18 to 2.20) the Jacobian terms can be expressed in terms of the velocity variables, u and v, where

$$u = \frac{-1}{G}\left[r + \frac{1}{G}\right]^{-1}\frac{\partial f}{\partial \psi} = \bar{u}\left[\frac{a}{\nu}\right] \qquad \text{(radial velocity)} \qquad (2.24)$$

and

$$v = \frac{1}{G}\frac{f}{r} = \bar{v}\left[\frac{a}{\nu}\right] \qquad \text{(tangential velocity)} \qquad (2.25)$$

With these substitutions, the dimensionless governing equations become:

Energy:

$$G^2\frac{\partial T}{\partial t} + uG\frac{\partial T}{\partial r} + vG\left[r + \frac{1}{G}\right]^{-1}\frac{\partial T}{\partial \psi}$$

$$= \frac{1}{Pr}\left\{\frac{\partial^2 T}{\partial r^2} + \left[r + \frac{1}{G}\right]^{-1}\frac{\partial T}{\partial r} + \left[r + \frac{1}{G}\right]^{-2}\frac{\partial^2 T}{\partial \psi^2}\right\} \qquad (2.26)$$

Vorticity:

$$Pr\left\{G^2\frac{\partial w}{\partial t} + uG\frac{\partial w}{\partial r} + vG\left[r + \frac{1}{G}\right]^{-1}\frac{\partial w}{\partial \psi}\right\}$$

$$= Pr\left\{\frac{\partial^2 w}{\partial r^2} + uG\frac{\partial w}{\partial r} + vG\left[r + \frac{1}{G}\right]^{-1}\frac{\partial w}{\partial \psi}\right\}$$

$$+ G(Ra)\left\{\sin\psi\frac{\partial T}{\partial r} + \cos\psi\left[r + \frac{1}{G}\right]^{-1}\frac{\partial T}{\partial \psi}\right\} \qquad (2.27)$$

Stream Function:

$$\frac{\partial^2 f}{\partial r^2} + \left[ r + \frac{1}{G} \right]^{-1} \frac{\partial f}{\partial r} + \left[ r + \frac{1}{G} \right]^{-2} \frac{\partial^2 f}{\partial \psi^2} = G^2 w \quad . \tag{2.28}$$

The form of Eqs (2.26 - 2.28) facilitates the asymptotic analysis that follows in Chapter III, where the limits of $Ra \to \infty$, $G \to 0$ and $Pr \to 0$ are separately examined.

<u>Boundary Conditions</u>. The nondimensional boundary conditions for this problem are obtained by substituting Eqs (2.13 - 2.17) into Eqs (2.8 - 2.10). They are at $r = 0$ (inner cylinder):

$$T = T_I(\psi)$$

$$w = \frac{1}{G^2} \frac{\partial^2 f}{\partial r^2}$$

$$f = 0 \tag{2.29}$$

and at $r = 1$ (outer cylinder):

$$T = 0$$

$$w = \frac{1}{G^2} \frac{\partial^2 f}{\partial r^2}$$

$$f = 0 \quad . \tag{2.30}$$

The computational continuous condition at zero and $2\pi$ radians still applies, except that dimensional quantities are now nondimensionalized.

<u>Initial Conditions</u>. The dimensionless initial conditions are virtually identical to Eqs (2.11 and 2.12) for the entire annulus:

$$T = f = w = 0, \tag{2.31}$$

except at the inner and outer cylinder walls, where:

$$T = T_I(\psi) \text{ at } r = 0$$

and

$$T = 0 \quad \text{at } r = 1 \quad . \tag{2.32}$$

These initial conditions assume a motionless fluid (Ra = 0), where the problem becomes the steady-state conduction case for a cylindrical annulus. However, when numerically searching for transitional or unsteady flow behavior, initial conditions other than zero are used. These procedures are discussed in Chapter IV.

## III. Analytical Analysis

In this section, simplified boundary-layer equations are derived from the 2-D Navier-Stokes equations for certain limiting conditions (see Fant, 1987). Analytical steady-state solutions to these equations are then determined.

### The Boundary Layer Equations

Using the governing Navier-Stokes equations as shown in Chapter II (Eqs 2.26 to 2.28), Fant (1987) obtained the following expansions of the dependent variables for the conditions of infinite Rayleigh number ($Ra \to \infty$) and small annular gap width ($G \to 0$):

$$u = Ra^{1/4}\tilde{u} + O(Ra^{-1/4})$$

$$v = Ra^{1/2}\tilde{v} + O(1)$$

$$w = Ra^{3/4}\tilde{w} + O(Ra^{1/4})$$

$$f = Ra^{1/4}\tilde{f} + O(Ra^{-1/4})$$

$$T = \tilde{T} + O(Ra^{-1/2}) \quad . \tag{3.1}$$

Using these expansions, the Navier-Stokes equations reduce to the following Cartesian-like, boundary-layer equations:

Energy:

$$\tilde{G}^2 \frac{\partial \tilde{T}}{\partial \tilde{t}} + \tilde{G} \left\{ - \frac{\partial \tilde{f}}{\partial \psi} \frac{\partial \tilde{T}}{\partial r} + \frac{\partial \tilde{f}}{\partial r} \frac{\partial \tilde{T}}{\partial \psi} \right\} = \frac{1}{Pr} \frac{\partial^2 \tilde{T}}{\partial r^2} \tag{3.2}$$

Vorticity:

$$\tilde{G}^2 \cdot Pr \frac{\partial \tilde{w}}{\partial \tilde{t}} + \tilde{G} \cdot Pr \left\{ - \frac{\partial \tilde{f}}{\partial \psi} \frac{\partial \tilde{w}}{\partial r} + \frac{\partial \tilde{f}}{\partial r} \frac{\partial \tilde{w}}{\partial \psi} \right\} = Pr \frac{\partial^2 \tilde{w}}{\partial r^2} + \tilde{G} \sin\psi \frac{\partial \tilde{T}}{\partial r} \quad (3.3)$$

Stream Function:

$$\frac{\partial^2 \tilde{f}}{\partial r^2} = \tilde{G}^2 \tilde{w} \quad (3.4)$$

with related boundary conditions,

$$\tilde{T}(0,\psi) = T_I(\psi), \quad \tilde{T}(1,\psi) = T_0(\psi) \quad (3.5)$$

$$\tilde{f}(0,\psi) = \tilde{f}(1,\psi) = 0 \quad (3.6)$$

$$\tilde{w}(0,\psi) = \tilde{w}(1,\psi) = \frac{1}{G^2} \frac{\partial^2 \tilde{f}}{\partial r^2} \bigg|_{r = 0,1} \quad . \quad (3.7)$$

Note that the annular curvature effects appear through $\sin\psi$ in the buoyancy term of the vorticity equation above. Variable wall temperature influence comes in through $T_I$ and $T_0$ in Eq (3.5). These governing equations are valid for finite Prandtl number. Importantly, the Rayleigh number and gap number dependency has vanished and is replaced by a single scaled gap parameter

$$\tilde{G} = Ra^{1/4} G \quad . \quad (3.8)$$

To maintain the unsteady term, time was scaled as

$$\tilde{t} = t \, Ra^{1/2} \quad . \quad (3.9)$$

The scaling of these equations is based on the scaling typical of laminar

natural convective boundary-layer flows, which come forth under the conditions of high Rayleigh number and small-gap width, namely,

$$\delta \sim Ra^{-1/4} \quad . \tag{3.10}$$

In this study, the finite Prandtl number boundary-layer equations are simplified for the limiting condition of $Pr \to 0$, characteristic of liquid-metal fluids. As discussed in the literature review, other studies of natural convection in narrow annuli have mostly concentrated on air as the working fluid. The study of small Prandtl number effects on flow instability for this particular geometry are rare, especially with regard to the variable wall temperature influence. The derivation that follows addresses this issue.

First, let vorticity and stream function scale as:

$$\tilde{w} = \lambda_1 W + \ldots . \tag{3.11}$$

$$\tilde{f} = \lambda_2 F + \ldots . \quad . \tag{3.12}$$

The stream function equation (3.4) requires

$$\lambda_2 \sim \tilde{G}^2 \lambda_1 \quad . \tag{3.13}$$

With Eqs (3.11) and (3.12), the vorticity equation (3.3) becomes

$$\tilde{G}^2 Pr \lambda_1 \frac{\partial W}{\partial \tilde{t}} + Pr\ \tilde{G} \lambda_2 \lambda_1 \left\{ - \frac{\partial F}{\partial \psi} \frac{\partial W}{\partial r} + \frac{\partial F}{\partial r} \frac{\partial W}{\partial \psi} \right\}$$

$$= Pr\ \lambda_1 \frac{\partial^2 W}{\partial r^2} + \tilde{G} \sin\psi \frac{\partial T}{\partial r} \tag{3.14}$$

or,

$$\frac{\tilde{G}^2 Pr\lambda_1}{\tilde{t}} \sim Pr\ \tilde{G}\ \lambda_2\ \lambda_1 \sim Pr\ \lambda_1 \sim \tilde{G} \tag{3.15}$$

in order to retain the physics of the problem. Balancing the viscous term with the buoyancy term gives

$$\lambda_1 \sim \frac{\tilde{G}}{Pr} \tag{3.16}$$

then Eq (3.13) yields,

$$\lambda_2 \sim \frac{\tilde{G}^3}{Pr} \quad . \tag{3.17}$$

Eqs (3.16) and (3.17) are then substituted into Eq (3.15) to get

$$\tilde{G} \sim 0(Pr^{1/4}) \tag{3.18a}$$

and $\tilde{t} \sim \tilde{G}^2$, which yields from Eq (3.18a)

$$\tilde{t} \sim 0(Pr^{1/2}) \quad . \tag{3.18b}$$

With these relations, new scaled variables can be defined:

$$\tilde{G} = \hat{G}\ Pr^{1/4} \tag{3.19a}$$

and

$$\tilde{t} = \hat{t}\ Pr^{1/2} \quad . \tag{3.19b}$$

Therefore,

$$\lambda_1 \sim Pr^{-3/4} \tag{3.20}$$

$$\lambda_2 \sim Pr^{-1/4} \tag{3.21}$$

which yield the following expansions:

$$\tilde{w} \sim Pr^{-3/4}\, W + O(Pr^{1/4}) \tag{3.22}$$

$$\tilde{f} \sim Pr^{-1/4}\, F + O(Pr^{3/4}) \tag{3.23}$$

$$\tilde{T} \sim T + O(Pr) \quad . \tag{3.24}$$

Scaled gap number and time can now be expressed in terms of the key dimensionless variables:

$$\hat{G} = Pr^{-1/4}\, \tilde{G} = \left(\frac{Ra}{Pr}\right)^{1/4} G \tag{3.25}$$

$$\hat{t} = Pr^{-1/2}\, \tilde{t} = \left(\frac{Ra}{Pr}\right)^{1/2} t \quad . \tag{3.26}$$

These new scaled variables show a unique dependency on Ra, Pr, G and t. Substitution of Eqs (3.22 - 3.26) into Eqs (3.2 - 3.4) yields the following simplified set of governing equations:

Energy:

$$\frac{\partial^2 T}{\partial r^2} = 0 \tag{3.27}$$

Vorticity:

$$\hat{G}^2 \frac{\partial W}{\partial \hat{t}} + \hat{G} \left\{ - \frac{\partial F}{\partial \psi} \frac{\partial W}{\partial r} + \frac{\partial F}{\partial r} \frac{\partial W}{\partial \psi} \right\} = \frac{\partial^2 W}{\partial r^2} + \hat{G} \sin\psi \frac{\partial T}{\partial r} \tag{3.28}$$

Stream Function:

$$\frac{\partial^2 F}{\partial r^2} = \hat{G}^2\, W \quad . \tag{3.29}$$

The energy equation is completely uncoupled from the vorticity equation. The boundary conditions for the energy equation are as follows,

$$T(0,\psi) = T_I(\psi) \tag{3.30}$$

$$T(1,\psi) = T_o(\psi) \tag{3.31}$$

where $T_I(\psi)$ and $T_0(\psi)$ denote inner and outer wall temperatures, respectively. The isothermal outer wall temperature for this model is taken to be zero, while the inner wall remains variable, or

$$T(0,\psi) = T_I(\psi) \tag{3.32}$$

$$T(1,\psi) = 0 \quad . \tag{3.33}$$

Integrating equation (3.27) twice yields,

$$T = C_1 r + C_2 \tag{3.34}$$

and applying the boundary conditions of Eqs (3.32) and (3.33) results in the following expansion for temperature across the annulus:

$$T(r,\psi) = (T_o - T_I)\, r + T_I \tag{3.35}$$

and

$$\frac{\partial T}{\partial r} = (T_o - T_I) \quad . \tag{3.36}$$

Using Eq (3.36), the governing equations reduce to their final form:

Vorticity:

$$\hat{G}\,\frac{\partial W}{\partial \hat{t}} + \hat{G}\left\{ -\frac{\partial F}{\partial \psi}\frac{\partial W}{\partial r} + \frac{\partial F}{\partial r}\frac{\partial W}{\partial \psi} \right\} = \frac{\partial^2 W}{\partial r^2} + \hat{G}\,\sin\psi\,(T_o - T_I) \tag{3.37}$$

Stream Function:

$$\frac{\partial^2 F}{\partial r^2} = \hat{G}\, W \tag{3.38}$$

with boundary conditions

$$F(0,\psi) = F(1,\psi) = 0 \tag{3.39}$$

$$\frac{\partial F}{\partial r}(0,\psi) = \frac{\partial F}{\partial r}(1,\psi) = 0 \quad . \tag{3.40}$$

These equations will be solved numerically in Chapter 5 using various inner wall temperature profiles in order to study flow behavior and the multicellular instabilities that may arise.

<u>The Steady-State Perturbation Solution</u>

Rearranging Eq (3.38) results in the following expression for vorticity:

$$W = \hat{G}^{-2} \frac{\partial^2 F}{\partial r^2} \quad . \tag{3.41}$$

Assuming steady-state conditions and substituting Eq (3.41) in Eq (3.37) yields:

$$\hat{G} \left\{ - \frac{\partial F}{\partial \psi} \frac{\partial^3 F}{\partial r^3} + \frac{\partial F}{\partial r} \frac{\partial^3 F}{\partial r^2\, \partial \psi} \right\} = \frac{\partial^4 F}{\partial r^4} + \hat{G}^3 (T_o - T_I) \sin \psi \quad . \tag{3.42}$$

Taking the limit of $\hat{G} \to 0$, one can derive a perturbative solution to the governing equations. By examining Eq (3.42) one can deduce the expansion for stream function to be

$$F = \hat{G}^3 F_1 + \hat{G}^7 F_2 + 0(\hat{G}^{11}) \tag{3.43}$$

and from Eq (3.41), vorticity can be expressed as

$$W = \hat{G}\, W_1 + \hat{G}^5\, W_2 + O(\hat{G}^9) \quad . \tag{3.44}$$

The first effects of the convective terms come in through $F_2$ and $W_2$. Substituting expansion (3.43) into Eq (3.42), and matching terms of like coefficients yields the following steady-state result:

$$\hat{G}^3: \quad \frac{\partial^4 F_1}{\partial r^4} = -\,(T_o - T_I)\, \sin\psi \tag{3.45}$$

$$\hat{G}^7: \quad \frac{\partial^4 F_2}{\partial r^4} = -\,\frac{\partial F_1}{\partial \psi}\,\frac{\partial^3 F_1}{\partial r^3} + \frac{\partial F_1}{\partial r}\,\frac{\partial^3 F_1}{\partial r^2\,\partial \psi} \quad . \tag{3.46}$$

Integrating Eq (3.45) yields,

$$F_1 = \frac{r^4}{4!}\,(T_I - T_o)\,\sin\psi + C_1\,\frac{r^3}{3!} + C_2\,\frac{r^2}{2} + C_3\, r + C_4 \quad . \tag{3.47}$$

The constants of integration are obtained from the boundary conditions of Eqs (3.39) and (3.40) and result in:

$$F_1 = r^2\,(r-1)^2\,(T_I - T_o)\,\frac{\sin\psi}{24} \quad . \tag{3.48}$$

Differentiating Eq (3.47) twice with respect to r yields

$$W_1 = \left\{ r\,(r-1) + \frac{1}{6} \right\} (T_I - T_o)\,\frac{\sin\psi}{2} \quad . \tag{3.49}$$

Substituting Eq (3.48) into Eq (3.46) yields

$$\frac{\partial^4 F_2}{\partial r^4} = \left\{ 6r^5 - 15r^4 + 14r^3 - 6r^2 + r \right\} (T_I - T_o)^2 \frac{2 \sin 2\psi}{24^2} \quad . \qquad (3.50)$$

Integrating Eq (3.50) four times and applying boundary conditions (Eqs 3.39 and 3.40) yields

$$F_2 = (T_I - T_o)^2 \frac{\sin 2\psi}{96} \left\{ \frac{r^9}{1512} - \frac{r^8}{336} + \frac{r^7}{180} - \frac{r^6}{180} + \frac{r^5}{360} - \frac{r^3}{1512} + \frac{r^2}{5040} \right\} \qquad (3.51)$$

and $W_2$ becomes

$$W_2 = (T_I - T_o)^2 \frac{\sin 2\psi}{96} \left\{ \frac{r^7}{21} - \frac{r^6}{6} + \frac{7r^5}{30} - \frac{r^4}{6} + \frac{r^3}{18} - \frac{r}{252} + \frac{1}{2520} \right\} \qquad (3.52)$$

The expressions for $F_2$ and $W_2$ contain the term $\sin 2\psi$, which may contribute to the multicellular behavior of the flow field at some critical value of $\hat{G}$. The one-term expansions, found to be

$$F = \hat{G}^3 r^2 (r - 1)^2 (T_I - T_o) \frac{\sin \psi}{24} \qquad (3.53)$$

$$W = \hat{G} \left\{ r (r - 1) + \frac{1}{6} \right\} (T_I - T_o) \frac{\sin \psi}{2}, \qquad (3.54)$$

provide good approximations in modeling pretransitional flow behavior for $Pr \to 0$. Since many terms in the perturbation expansion may be required to capture complex flow behavior, one expects the two-term equations to be valid for only weakly-nonlinear flow instability. In this study, the full effects of the nonlinear convective terms were handled by solving

the partial diferential equations numerically (see Chapter 4).

Eqs (3.53) and (3.54) represent analytical solutions for the steady-state pretransitional stream function and vorticity, applicable throughout the annulus (0 - $2\pi$). In this form, a variety of variable wall temperature conditions can be considered. These temperature profiles, which can vary with the angular coordinate $\psi$, may be used to model various hot and cold spots on the cylinder walls. Several interesting variations of the inner cylinder wall temperature are described in detail in Chapter 5. Numerical and analytical solutions relating to each inner wall temperature variation are also presented and compared in this chapter.

# IV. Numerical Analysis

There are two topics of discussion in this chapter. The first describes the finite-differencing method used in solving the coupled set of governing partial differential equations. These equations are the 2-D unsteady boundary-layer equations developed in Chapter 3. The second topic deals with the computational procedure employed to solve the resulting finite-difference equations. Here, the iteration sequence, convergence criterion, and relaxation parameters for the numerical procedure are described.

The basic numerical approach, relating to the zero-Prandtl number flow regime, was adopted from Fant (1987). In this study, however, the buoyancy term in the vorticity equation was modified to account for nonisothermal effects.

In handling the streamwise nonlinear convective terms, a corrected second-order upwind scheme was used for the boundary-layer equations. For the radial convective terms, a corrected second-order central difference expression was employed. This approach ensured numerical stability when solving highly convective flow problems. The unsteady form of the equations provided the opportunity to capture both steady and unsteady behavior when solved in a time-accurate fashion.

## The Numerical Method

The 2-D unsteady boundary-layer equations presented in Eqs (3.37) and (3.38) are discretized using finite-differencing techniques. The governing equations in discretized form are well-suited for solving on a

high-speed computer system. The computational domain consists of a cellular mesh formed by the intersection of variably spaced radial lines with circular arcs concentric with r = 1. The grid nodes are the points where these radial lines and concentric arcs intersect. The cellular mesh generalized for variable increments is shown in Figure 4.1. Since the angular distance between the nodes was kept constant in this model, the variables ($K_b$, $K_f$, ...) in Figure 4.1 were simply replaced by the constant K. In general, the use of variable increments in the computational domain permits the concentration of nodes in areas of large gradients, such as the boundary-layer regions near the inner and outer cylinder walls.

For all temperature distributions imposed on the inner cylinder, the complete annular flow field (0 - $2\pi$) was numerically resolved. Vertical symmetry was not assumed.

<u>Variable Increment Finite-difference Formulas</u>. The derivatives in the governing equations are transformed into variable increment finite-difference expressions using Taylor series expansions.

Standard expressions for forward, backward and central differences, taking into account formal truncation errors for variable increments, are given in Fant (1987).

For the unsteady term in the equations, a stable forward-difference molecule is used:

$$\left.\frac{\partial\phi}{\partial\hat{t}}\right|_0 = \frac{\phi_0^{n+1} - \phi_0^n}{\Delta\hat{t}} + 0(\Delta\hat{t}) \tag{4.1}$$

where n is the time level at which the dependent variable $\phi$ is evaluated.

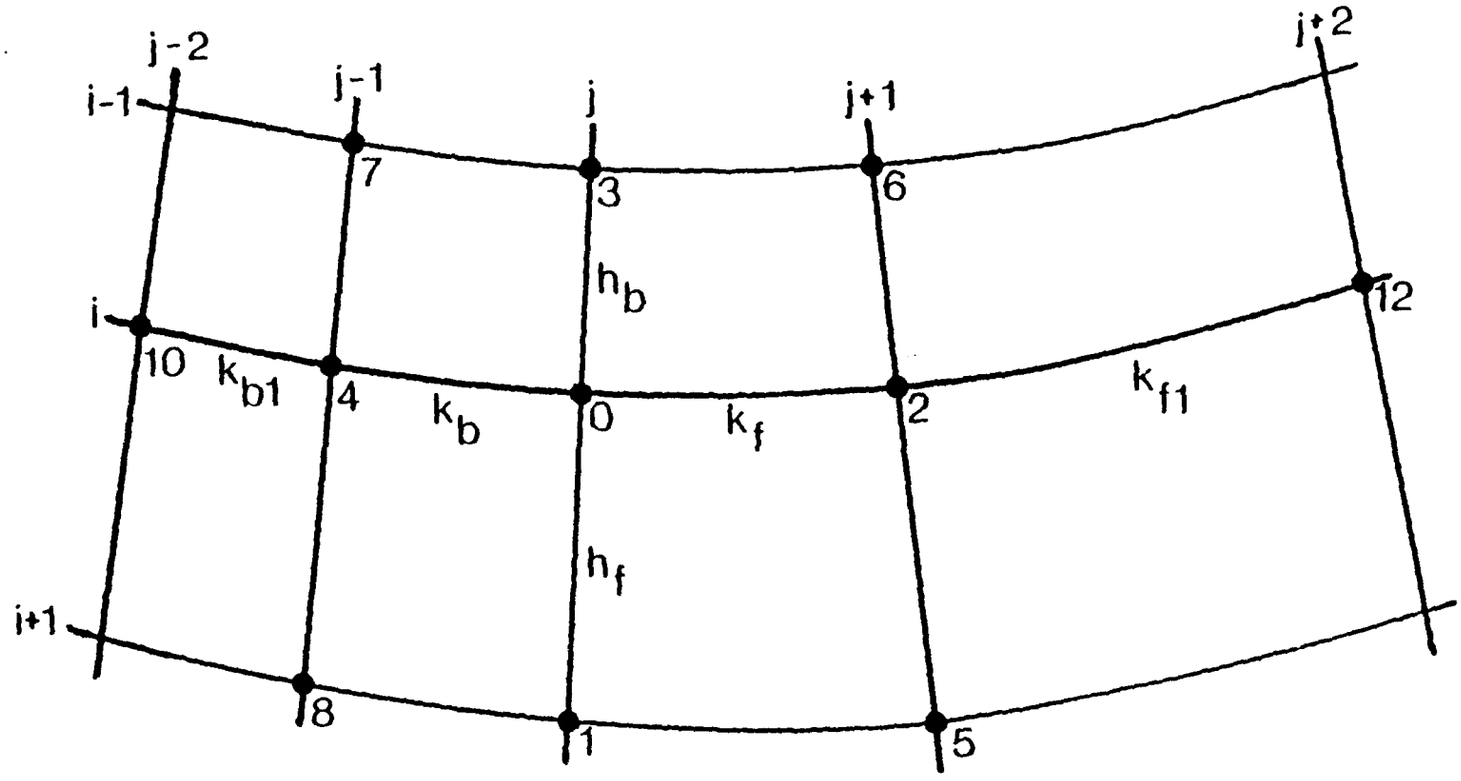


Figure 4.1. Computational mesh with variable increments

Finite-Difference Equations for the Dependent Variables. All spatial derivatives in the governing equations are second-order centrally (or upwind) differenced. This includes the convective terms in the vorticity equation (3.37) which are represented by a first-order upwind expression together with a correction term for second-order accuracy. The convective terms are split in this manner in order to enhance numerical stability when resolving secondary flow behavior. This procedure is explained in greater detail in Fant (1987). For the zero-Prandtl boundary-layer equations, only the vorticity and stream function equations (Eqs 3.37 and 3.38) had to be solved numerically in a coupled manner. The following one-equation format is used to represent these two coupled equations:

$$\Delta 2 \left\{ - \tilde{\Delta}\hat{G}^2 \frac{\partial \phi}{\partial \hat{t}} + \frac{\partial^2 \phi}{\partial r^2} \right\} + 2\lambda \frac{\partial \phi}{\partial r} + 2\mu \frac{\partial \phi}{\partial \psi} + S = 0 \qquad (4.2)$$

with the nonlinear convective terms expressed as:

$$2\lambda \frac{\partial \phi}{\partial r} = (\lambda - |\lambda|) \left\{ \frac{\phi_0 - \phi_3}{h_b} + \frac{\phi_1 + H\phi_3 - (1 + H)\,\phi_0}{h_b + h_f} \right\}$$

$$+ (\lambda + |\lambda|) \left\{ \frac{\phi_1 - \phi_0}{h_f} - \frac{\phi_1/H + \phi_3 - (1 + 1/H)\,\phi_0}{h_b + h_f} \right\} \qquad (4.3)$$

and

$$2\mu \left.\frac{\partial\phi}{\partial\psi}\right|_0 = (\mu - |\mu|)\left\{\frac{\phi_0 - \phi_4}{K} + \frac{\phi_0 - 2\phi_4 + \phi_{10}}{}\right\}$$

$$+ (\mu + |\mu|)\left\{\frac{\phi_2 - \phi_0}{K} + \frac{2\phi_2 - \phi_1 - \phi_{12}}{2K}\right\} \qquad (4.4)$$

where $\phi$ represents the dependent variables T or W, and

$$H = \frac{h_f}{h_b} \quad .$$

Also,

$$2\lambda = \Delta 1 \cdot \frac{\partial F}{\partial\psi} \qquad (4.5a)$$

and

$$2\mu = - \Delta 1 \cdot \frac{\partial F}{\partial\tau} \qquad (4.5b)$$

where

$$\Delta 1 = \begin{cases} \hat{G}, & \phi = W \\ 0, & \phi = F \end{cases} \qquad \Delta 2 = \begin{cases} 1, & \phi = W \\ 1, & \phi = F \end{cases}$$

with

$$\tilde{\Delta} = \begin{cases} 1, & \phi = W \\ 0, & \phi = F \end{cases} \quad .$$

For the radial convective terms (Eq 4.3), the first terms within the brackets are the first-order upwind-difference components and the second terms are the added corrections which bring the differencing up to second-order accuracy. The $\lambda$ terms within the parenthesis ensure that stable differencing 'into-the-wind' is enforced. since the boundary-layer equations are only first order in $\psi$, a corrected second-order upwind-differenced expression was used to represent the streamwise convective terms (Eq 4.4). Here, the second term within the brackets represents the added correction to achieve second-order accuracy.

Using the above results, the boundary-layer equations are written in the following finite-difference form:

$$C_0\phi_0^{n+1} = \frac{(\Delta 2)\ \tilde{\Delta}\ \hat{G}^2}{\tau}\phi_0^{n} + C_1\phi_1^{n+1} + C_2\phi_2^{n+1} + C_3\phi_3^{n+1}$$

$$+ C_4\phi_4^{n+1} + E^{n+1} + S^{n+1} \qquad (4.6a)$$

where

$$C_0 = \frac{(\Delta 2)\ \tilde{\Delta}\ \hat{G}^2}{\tau} + \frac{2(\Delta 2)}{h_b h_f} + \Gamma\lambda\left[\frac{1}{h_f} - \frac{1}{h_b}\right] + \Gamma|\lambda|\left[\frac{1}{h_b} + \frac{1}{h_f}\right]$$

$$+ \Gamma\ |\mu|\left[\frac{2}{K}\right] \qquad (4.6b)$$

$$C_1 = \frac{2(\Delta 2)}{h_f\ (h_f + h_b)} + \Gamma\left[\frac{\lambda + |\lambda|}{h_f}\right] \qquad (4.6c)$$

$$C_2 = \Gamma \left[ \frac{\mu + |\mu|}{K} \right] \tag{4.6d}$$

$$C_3 = \frac{2(\Delta 2)}{(h_f + h_b)\, h_b} - \frac{\Gamma\,(\lambda - |\lambda|)}{h_b} \tag{4.6e}$$

$$C_4 = \frac{-\Gamma\,(\mu - |\mu|)}{K} \tag{4.6f}$$

with

$$\Gamma = \begin{cases} 1, & \phi = W \\ 0, & \phi = F \end{cases} . \tag{4.6g}$$

The correction term $E^{n+1}$ is defined as follows:

$$\begin{aligned} E^{n+1} = {} & \Gamma \left[ \frac{\lambda}{h_f + h_b} \right] \left\{ \phi_1^{n+1} \left[ 1 - \frac{1}{H} \right] + \phi_3^{n+1} (H - 1) - \phi_0^{n+1} \left[ H - \frac{1}{H} \right] \right\} \\ & - \Gamma \left[ \frac{|\lambda|}{h_f + h_b} \right] \left\{ \phi_1^{n+1} \left[ 1 + \frac{1}{H} \right] + \phi_3^{n+1} (1 + H) - \phi_0^{n+1} \left[ 2 + H + \frac{1}{H} \right] \right\} \\ & + \mu\Gamma \left\{ \phi_2^{n+1} \left[ \frac{1}{K} \right] - \phi_4^{n+1} \left[ \frac{1}{K} \right] + \phi_{10}^{n+1} \left[ \frac{1}{2} \right] - \phi_{12}^{n+1} \left[ \frac{1}{K} \right] \right\} \\ & + |\mu|\Gamma \left\{ \phi_2^{n+1} \left[ \frac{1}{K} \right] + \phi_4^{n+1} \left[ \frac{1}{K} \right] - \phi_0^{n+1} \left[ \frac{1}{K} \right] - \phi_{10}^{n+1} \left[ \frac{1}{K} \right] \right. \\ & \left. - \phi_{12}^{n+1} \left[ \frac{1}{K} \right] \right\} . \end{aligned} \tag{4.6h}$$

In addition,

$$S^{n+1} = \begin{cases} \hat{G} \sin \psi_0 \{ T_{OUTER}(\psi_0) - T_{INNER}(\psi_0) \}, & \phi = W \\ - \hat{G}^2 W_0^{n+1}, & \phi = F \end{cases} \tag{4.6i}$$

where the buoyancy term (Eq 4.6i) permits variations in temperature with $\psi$ on the inner and outer cylinders.

<u>Boundary Conditions</u>. Considering the complete annulus, the finite-difference form of the boundary conditions are:

Energy:

$$T_{i,j}^{n+1} = T_I(\psi) \tag{4.7a}$$

$$T_{NR,j}^{n+1} = 0 \tag{4.7b}$$

Vorticity:

$$W_{1,j}^{n+1} = \frac{2F_{2,j}^{n+1}}{(\hat{G}h_1)^2} \tag{4.7c}$$

$$W_{NR,j}^{n+1} = \frac{2F_{NR-1,j}^{n+1}}{(\hat{G}h_{NR-1})^2} \tag{4.7d}$$

Stream Function:

$$F_{1,j}^{n+1} = 0 \tag{4.7e}$$

$$F_{NR,j}^{n+1} = 0 \quad . \tag{4.7f}$$

To satisfy continuity at zero and $2\pi$ radians, a computational continuous condition must be defined such that:

$$\phi_{i,1}^{n+1} = \phi_{i,NS+1}^{n+1} \tag{4.7g}$$

where $\phi$ represents the temperature, vorticity, or stream function. Again, for further discussion of this differencing procedure, see Fant (1987).

## The Computational Procedure

The system of coupled finite-difference equations (as described in the preceding section) are solved implicitly in time using a point iterative Gauss-Siedel method with underrelaxation. At a given time level, the dependent variables are found by repeated iterations of the governing equations.

With the inner and outer wall temperature distributions preset, the dependent variables were initialized by setting them to zero. Previously converged results at a particular time level were used as initial conditions to start the next time level calculations. This procedure was repeated until steady-state was achieved or unsteady behavior developed.

Iteration Sequence and Convergence Criterion. The boundary-layer governing equations in finite-difference form were numerically iterated in the following order:

i. vorticity equation

ii. stream function equation.

For the small-Prandtl number limiting condition, the energy equation was integrated analytically.

The above sequence was repeated until successive iterations were within a prescribed tolerance. The maximum modulus of the difference

between vorticity and stream function for two successive iteration values defined the relative convergence constraint, or

$$\max \left| \frac{\phi^{m+1,n+1} - \phi^{m,n+1}}{(\phi^{m+1,n+1})_{max}} \right| < 1 \times 10^{-6} \tag{4.8}$$

where $\phi$ again represents vorticity or stream function. When Eq (4.8) was satisfied, the numerical solution was considered converged. Here, m refers to the iteration level and n denotes the time level.

<u>Relaxation Parameters</u>. Two independent relaxation parameters, $\Omega_1$ and $\Omega_2$ were incorporated into the finite-difference equations to control the rate of convergence of the iterations. The relaxation parameter, $\Omega_1$, was used in conjunction with the vorticity boundary conditions. For example, on the inner cylinder:

$$W_{1,j}^{m+1,n+1} = \Omega_1 \{ 2F_2^{m,n+1}/(\hat{G}h_1)^2 \} + (1 - \Omega_1) W_{1,j}^{m,n+1} \tag{4.9}$$

along r = 0, where $h_1$ denotes the radial spacing between the first adjacent node and the wall. Typically, $.1 \leq \Omega_1 \leq .5$ was the range used to help stabilize the numerical computations. The second relaxation parameter, $\Omega_2$, was used with the second-order upwind differenced correction terms which were based on the new time level ($E^{n+1}$). The interior point equations for the vorticity were computed according to:

$$W_0^{m+1,n+1} = \frac{(\Delta 2)\tilde{\Delta}\ \hat{G}^2}{C_0 \tau} W_0^n + \{ C_1 W_1^{m,n+1} + C_2 W_2^{m,n+1} + C_3 W_3^{m+1,n+1} + C_4 W_4^{m+1,n+1}$$

$$+ S^{m+1,n+1} \}/ C_0 + \{ \Omega_2 E^{m+1,n+1} + (1 - \Omega_2) E^{m,n+1} \}/ C_0 \tag{4.10}$$

For $\Omega_2 < 1$, the differencing of the correction term became a weighted

average of Gauss-Siedel (current level) and Jacobi (previous level) iterations. Generally, $.1 \leq \Omega_2 \leq .5$ was used in the numerical computations. For further details on the computational procedure, see Fant (1987).

Computational Details and Discussion. All computational runs were made using 31 radial nodes and 241 angular nodes for the entire annulus ($0 - 2\pi$). The mesh spacing was slightly compressed by a factor of 1.5 near the inner and outer walls.

For all calcualtions, a scaled time step ($\Delta\hat{t}$) of 0.5 was chosen. This size time step translates to small actual time increments since $\hat{t} = (Ra/Pr)^{1/2}t$. For each test case (inner cylinder temperature distribution), $\hat{G}$ values of increasing magnitude were considered until unsteady behavior resulted. All test cases were started by obtaining the $\hat{G} = 1.0$ flow field. Then for each slightly higher value of $\hat{G}$, the flow conditions from the previous $\hat{G}$ value served as reference data for the new set of results. When flow instability developed at some value of $\hat{G}$, the number of iterations for convergence and the computer CPU-time increased significantly. Only one test case, $T_I(\psi) = \sin \psi$, was used to gain unsteady flow results (see Chapter 5). All other test cases were studied within the steady-state regime.

Generally, steady-state solutions were achieved within 40 time steps, although solutions were taken to 500 time steps to ensure convergence. The amount of CPU-time required to achieve the steady-state condition was approximately 38.4 seconds, or an average of 0.96 seconds per time step on the AFIT VAX 8650 computer system. Conversely, about 4 hours CPU-time was required to run 200 time steps when dealing with the

unsteady multicellular flow regime. Such time-consuming operations restricted the amount of unsteady flow studies that could be conducted for this thesis.

## V. Results and Discussion

In this chapter, the flow fields resulting from various temperature distributions imposed on the inner cylinder wall are examined. For each variable inner wall temperature distribution, $T_I(\psi)$, a set of isotherm and streamline contour plots are presented for flow visualization. In the streamline contour plots, the numbers embedded in the streamlines denote stream function strength, where negative values denote counter-clockwise fluid rotation and positive values denote clockwise rotation. Positive and negative isotherm lines represent hot and cold regions, respectively, on the inner cylinder. Steady-state analytical results are directly compared using plots of vorticity and stream function data in areas of interest within the annular flow field. In addition, the unsteady flow regime shall be examined for one of the test cases described below.

### Inner Cylinder Temperature Distributions

Figure 5.1 displays the ten inner cylinder temperature distributions considered in this study. Test cases (a - f) were chosen to impose regions of gradual temperature variation around the annulus, as modeled by simple trignometric functions. More localized hot and cold spots were modeled in cases (g - j). The presence of localized heating on the inner cylinder wall reflects a more realistic condition than the isothermal boundary condition that dominates similar studies in this area. Note that the circles in Figure 5.1 represent the inner cylinder with the important features of the temperature distribution drawn in for clarity.

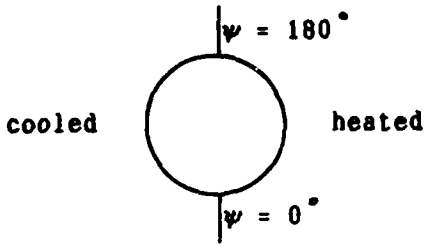


a. $T_I(\psi) = \sin \psi$

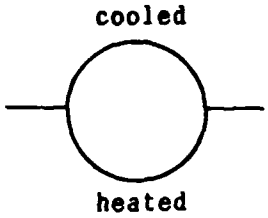


b. $T_I(\psi) = \cos \psi$

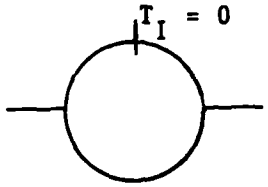


uniform heating @ $T_I = 1$

c. $T_I(\psi) = \begin{cases} 1 + \cos \psi, & 90^\circ < \psi < 270^\circ \\ 1, & 270^\circ < \psi < 90^\circ \end{cases}$

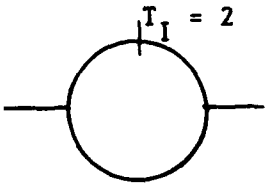


uniform heating @ $T_I = 1$

d. $T_I(\psi) = \begin{cases} 1 - \cos \psi, & 90^\circ < \psi < 270^\circ \\ 1, & 270^\circ < \psi < 90^\circ \end{cases}$

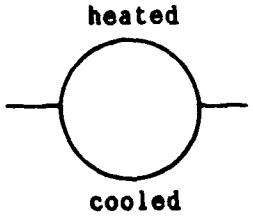


e. $T_I(\psi) = -\cos \psi$

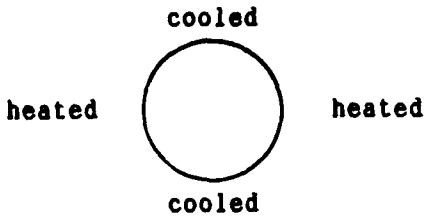


f. $T_I(\psi) = -\cos(2\psi)$

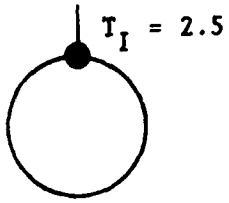


g. Single Hot Spot

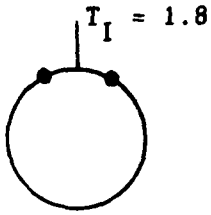


h. Dual Hot Spot

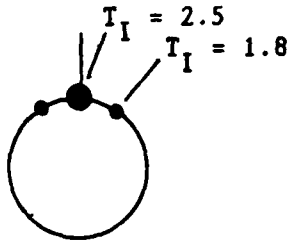


i. Triple Hot Spot

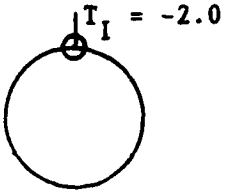


j. Cold Spot

Figure 5.1. Inner cylinder temperature distributions

The functional form of the annular temperature variation is presented to the left of sketch. More detailed isotherm representations of these test cases are given in the next section and in Appendix A.

## Numerical Results

In this section, several test cases which illustrate the variety of flow characteristics encountered in this study are discussed. Results of other temperature distributions are mentioned only briefly, with their stream function and vorticity plots included in Appendix A for completeness. In all but a few cases, numerical results were obtained for (scaled) gap numbers of 3.0 and 4.40 to examine low and moderate buoyancy effects on the flow circulation within the annulus. Three inner wall temperature distributions were examined up to the unsteady flow transition point, with one case ran at a gap number high enough to induce unsteady effects.

Steady-State Results. Case a, $T_I = \sin \psi$, was found to yield steady-state results for gap numbers up to 4.95. The isotherms for this temperature distribution are shown in Figure 5.2a. For gap numbers up to 4.93, the flow field exhibited the familiar kidney-shaped cell pattern, shown in Figure 5.2b, associated with an isothermal inner cylinder ($T_I = 1$). As Figure 5.2c illustrates, a steady multicellular flow develops in the vertical portions of the annulus when gap number is increased to 4.95. This type of flow instability appears to be hydrodynamic in origin, induced by fluid buoyancy shear effects. The instability occurs near the hottest/coldest parts of the inner cylinder ($\psi = 90^\circ, 270^\circ$). This makes sense physically since this is where the largest temperature difference between the inner and outer cylinders

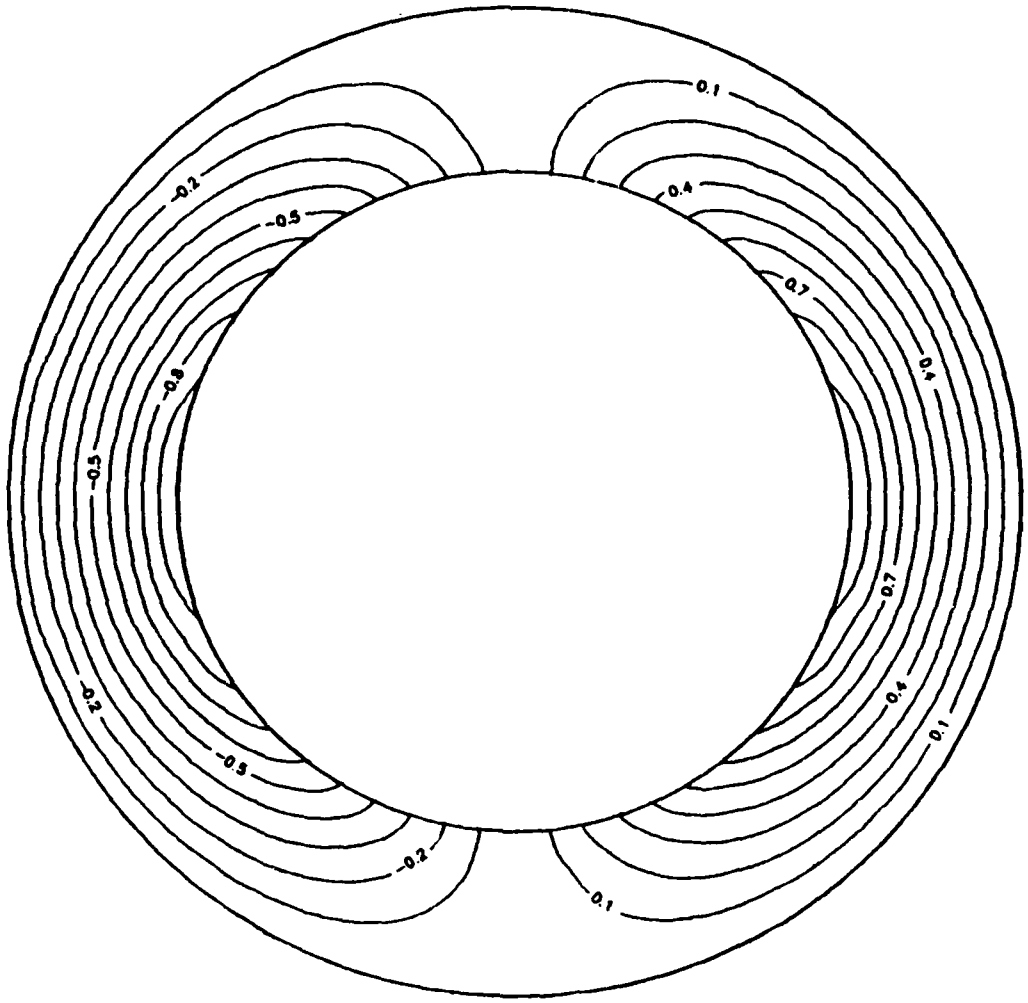


Figure 5.2a. Isotherms for $T_I(\psi) = \sin \psi$

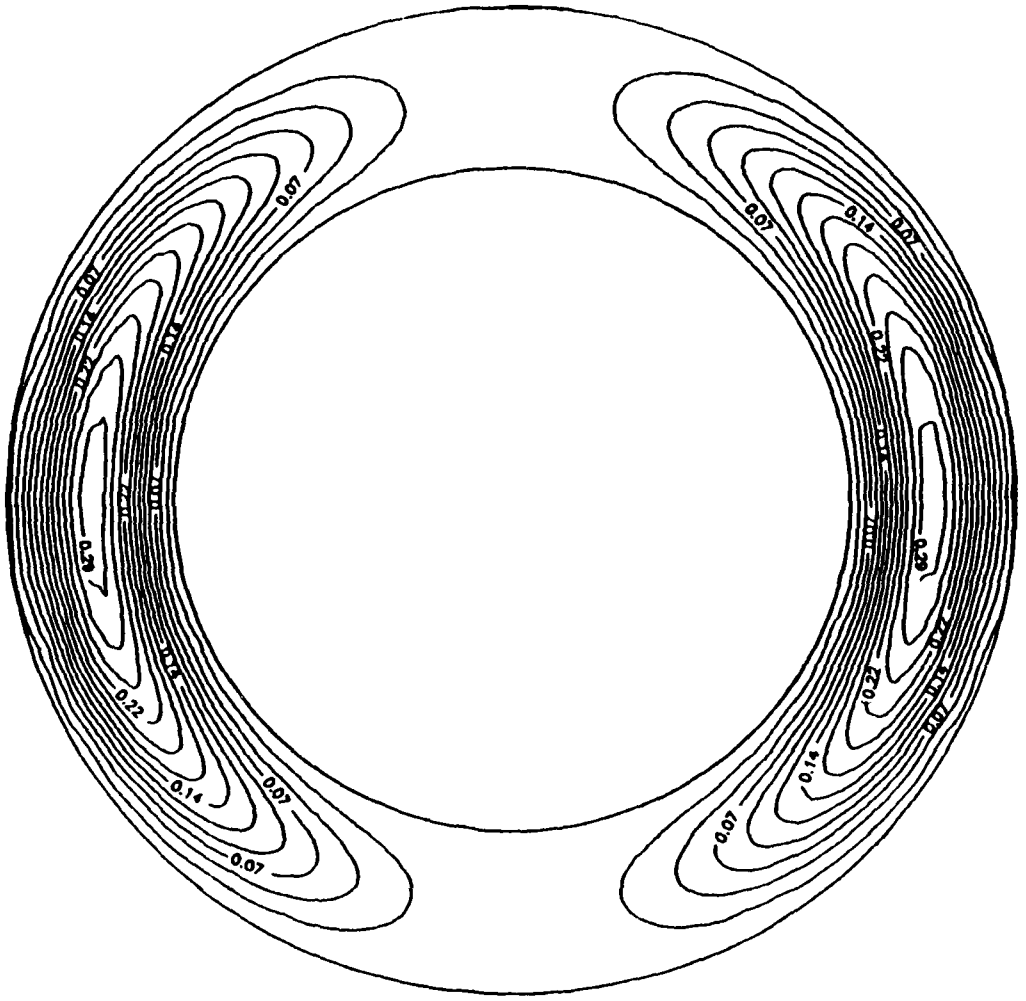


Figure 5.2b. Numerical streamlines for $T_I(\psi) = \sin \psi$ at $\hat{G} = 4.93$

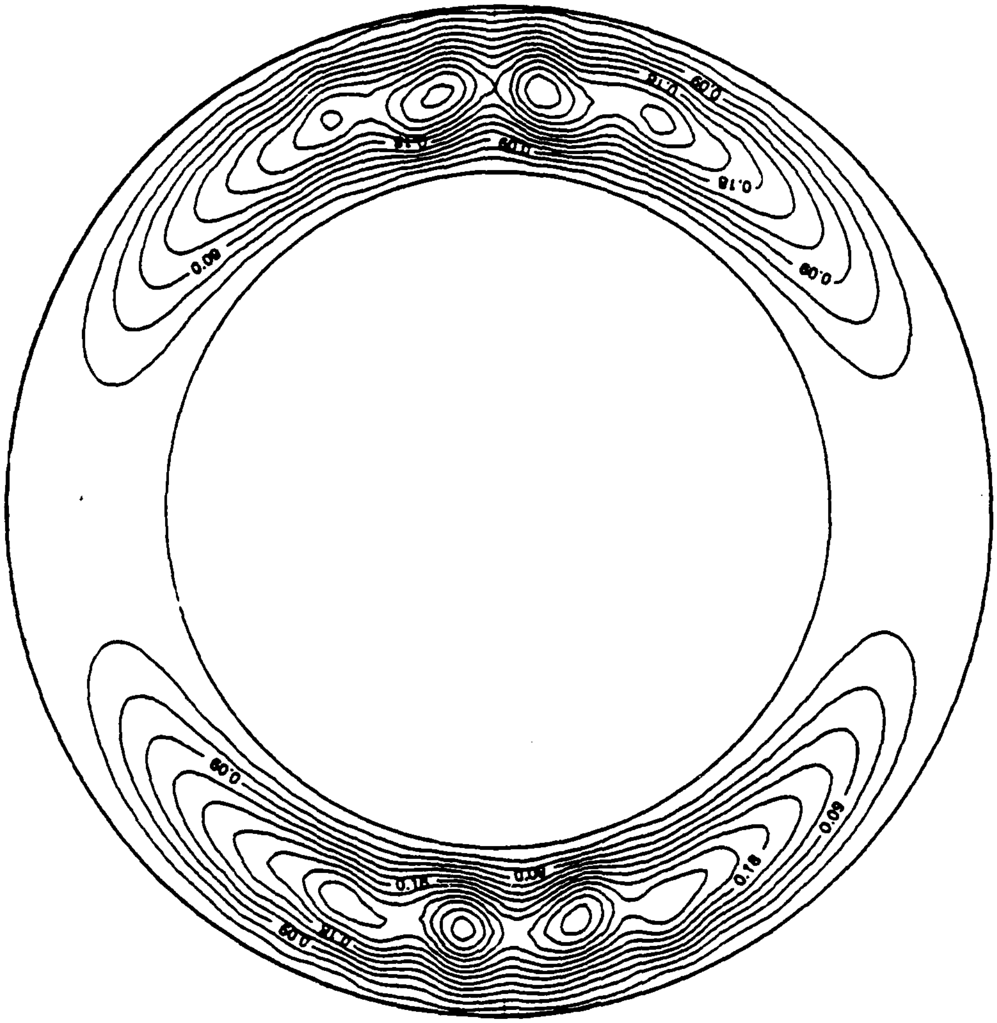


Figure 5.2c. Numerical streamlines for $T_I(\psi) = \sin \psi$ at $\hat{G} = 4.95$

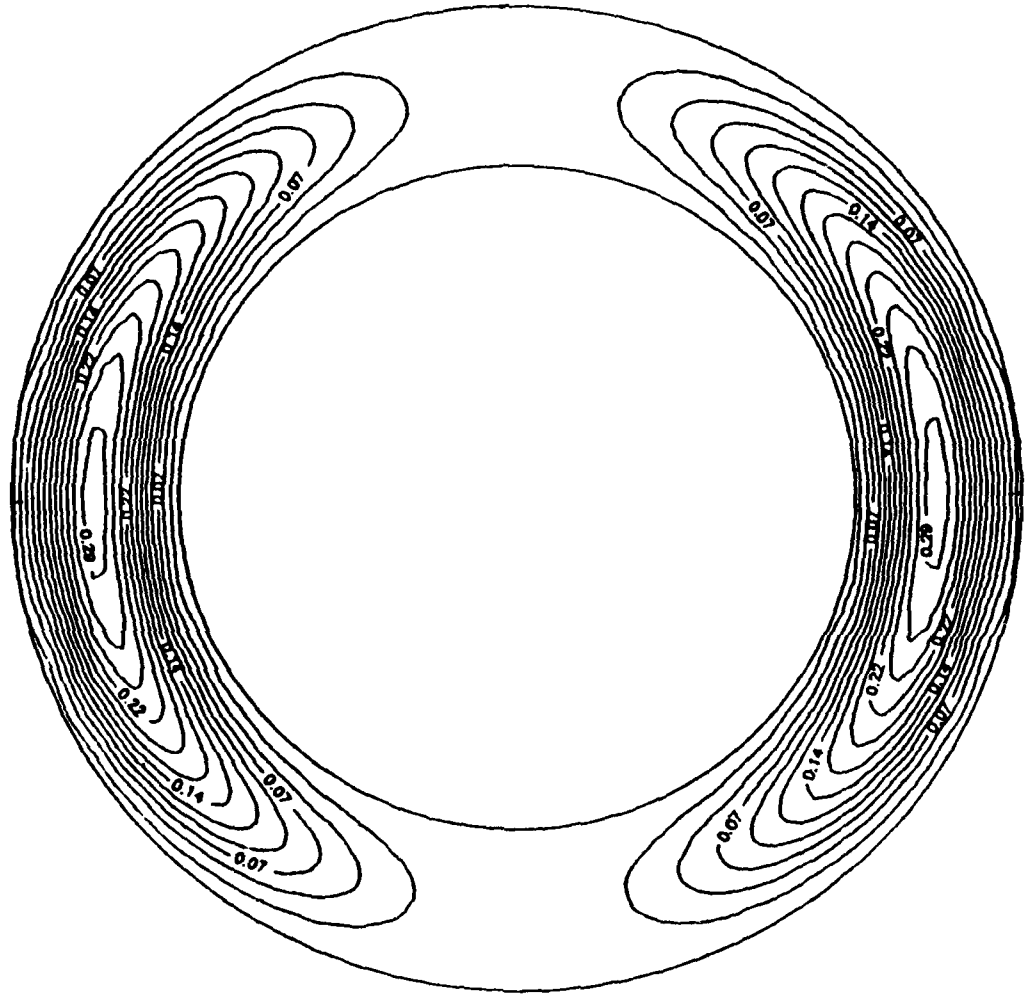


Figure 5.2d. Analytical streamlines for $T_I(\psi) = \sin \psi$ at $\hat{G} = 4.95$

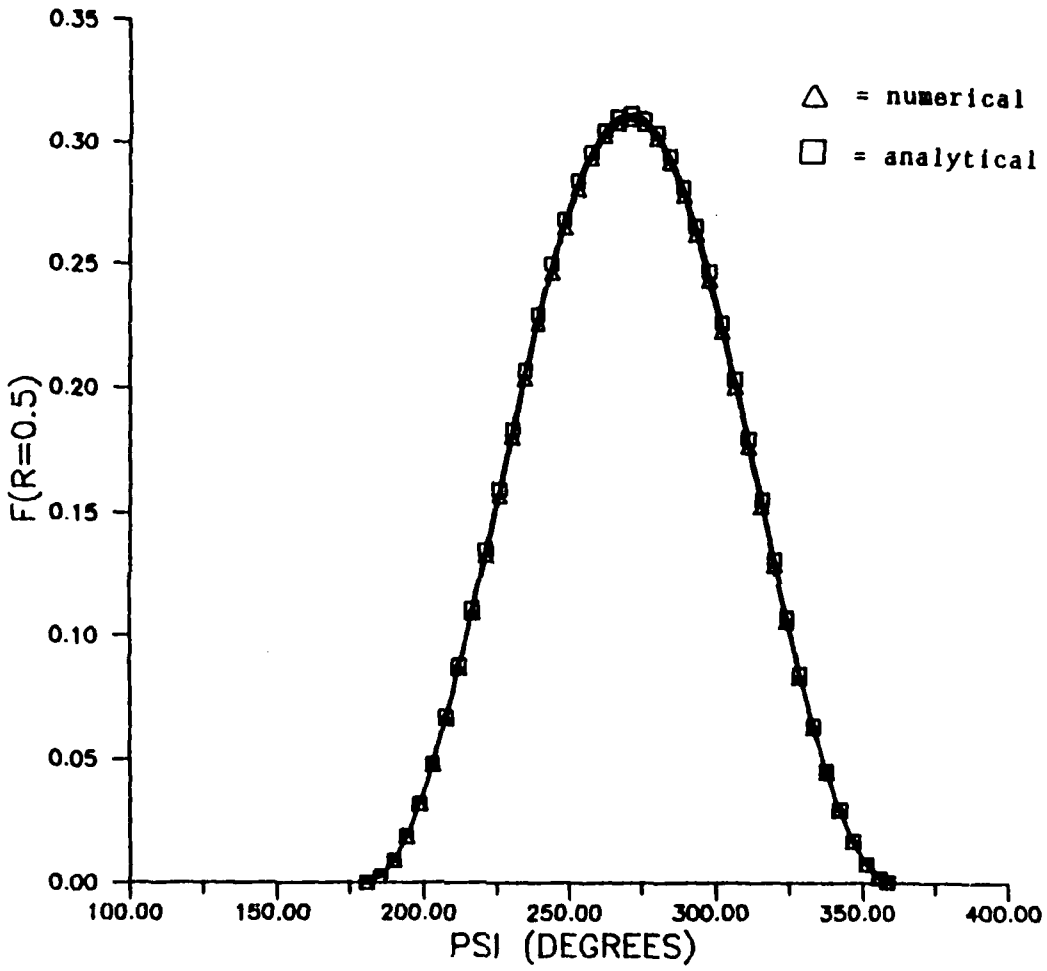


Figure 5.2e. Angular variation of the center-line stream function for $T_I(\psi) = \sin \psi$ at $G = 4.93$

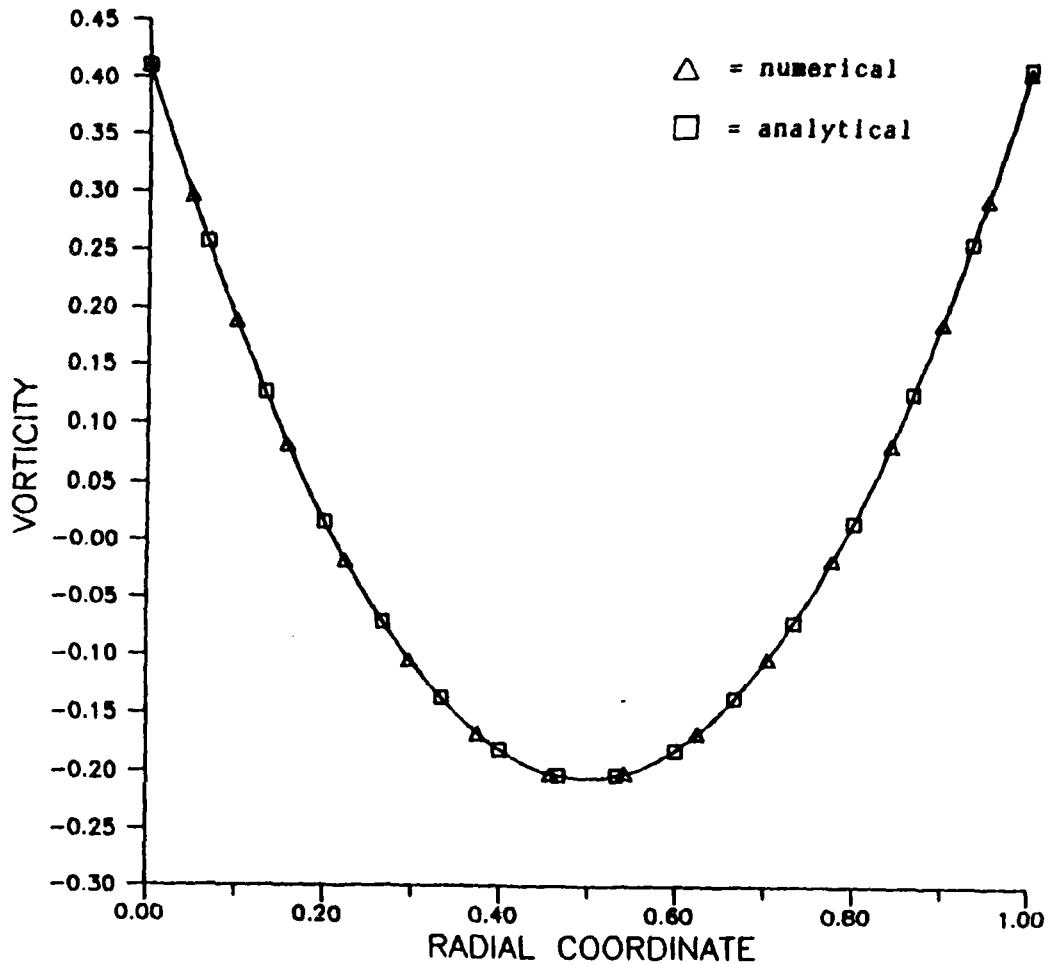


Figure 5.2f. Radial variation of vorticity at 90° for $\hat{G} = 4.93$
$T_I(\psi) = \sin \psi$

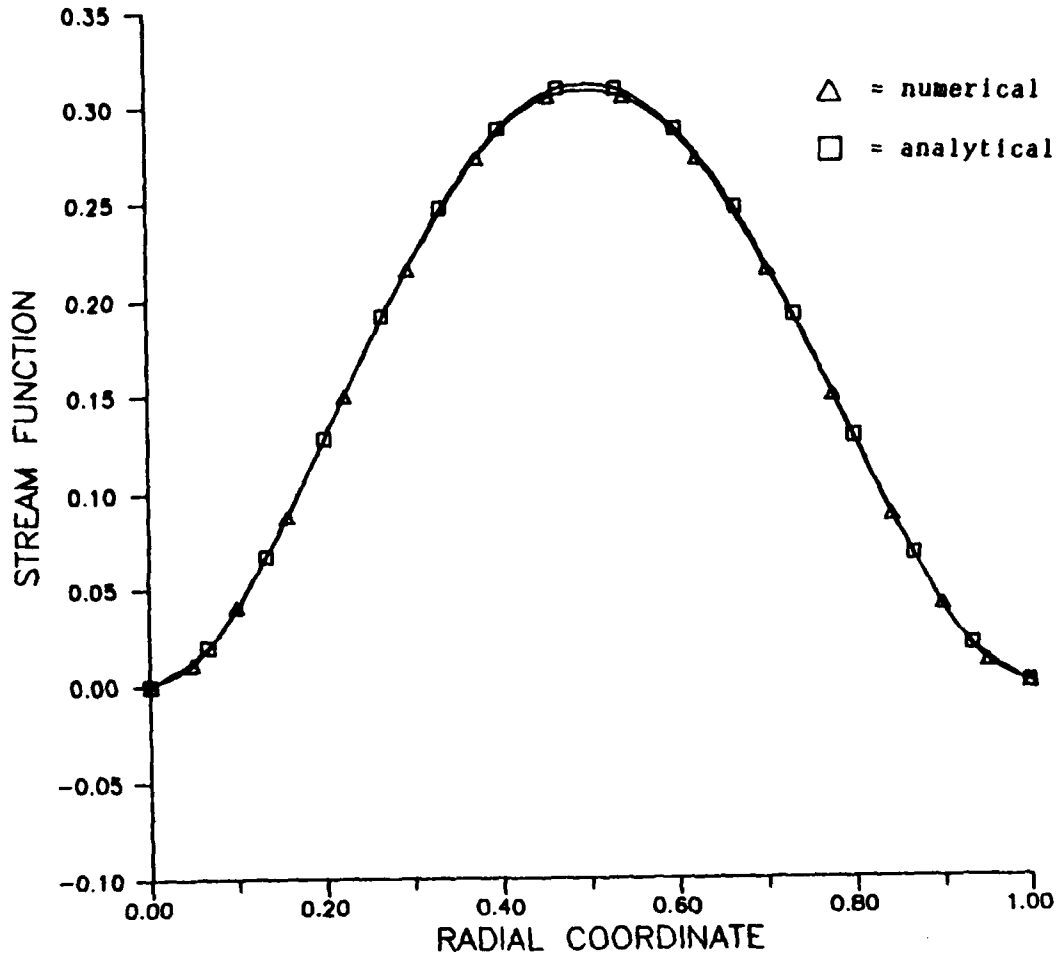


Figure 5.2g. Radial variation of the stream function at 90° for $\hat{G}$ = 4.93
$T_I(\psi) = \sin \psi$

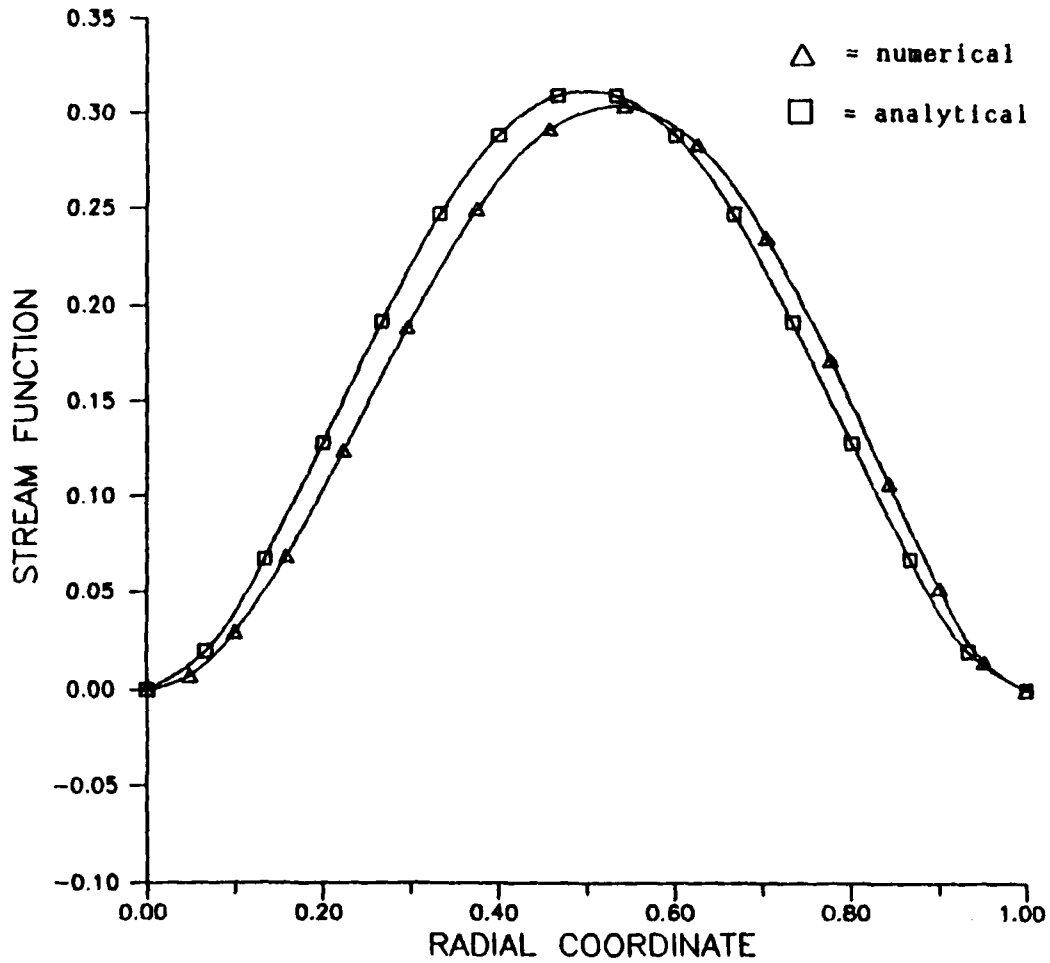


Figure 5.2h. Radial variation of the stream function at 90° for $\hat{G} = 4.95$
$T_I(\psi) = \sin \psi$

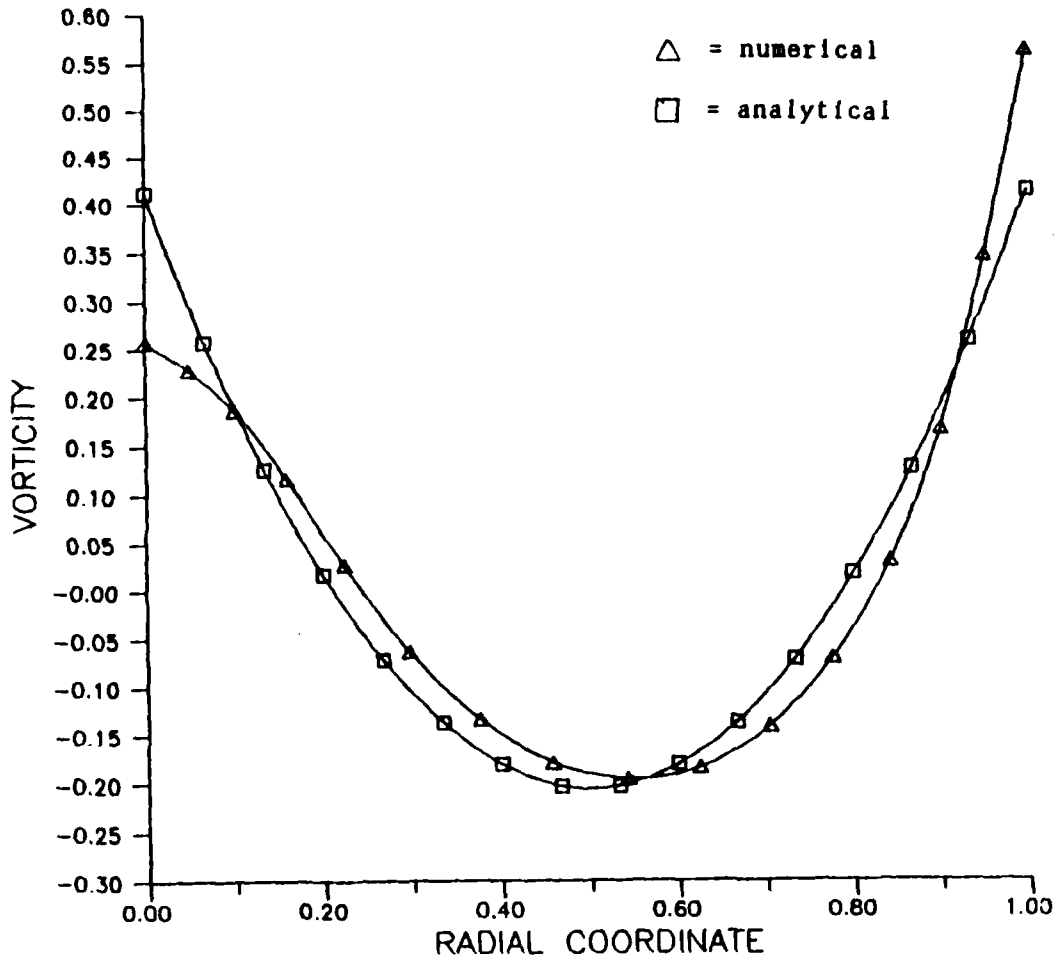


Figure 5.2i. Radial variation of vorticity at 90° for $\hat{G}$ = 4.95
$T_I(\psi) = \sin \psi$

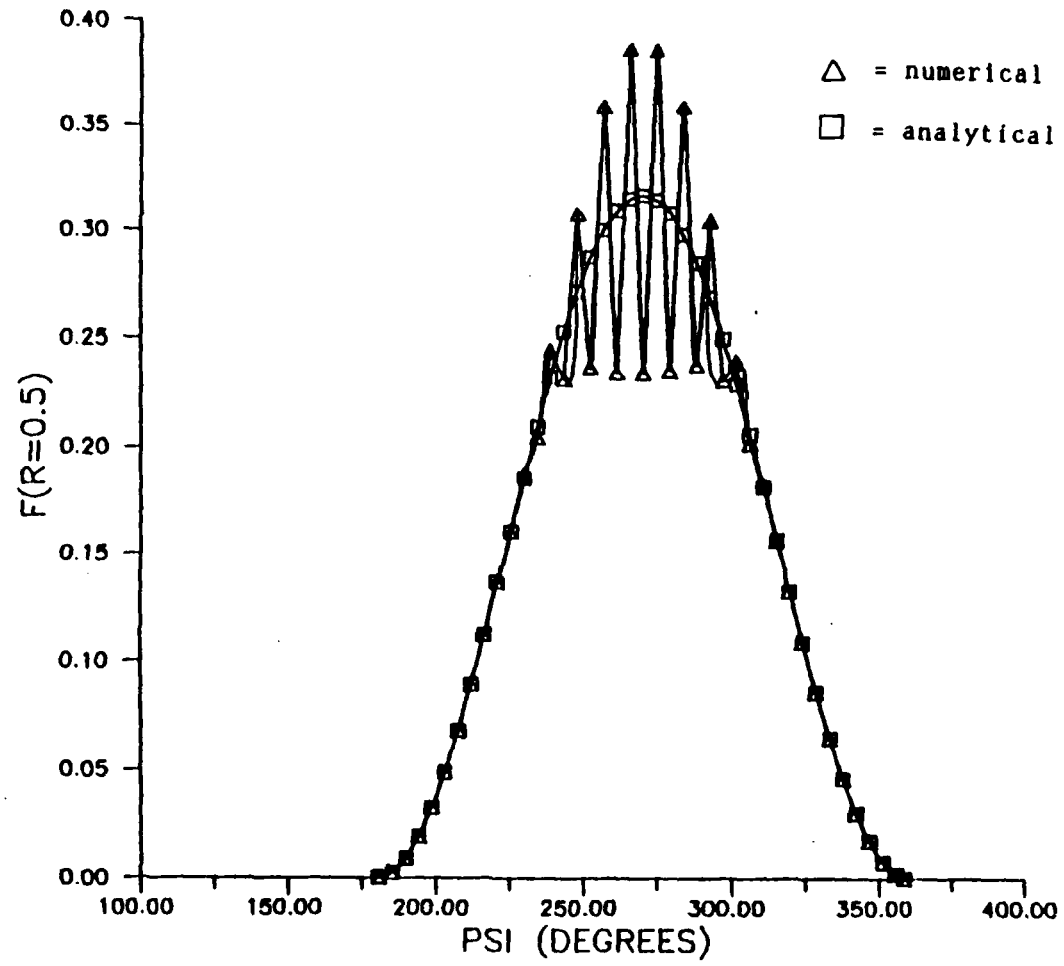


Figure 5.2j. Angular variation of the center-line stream function for $T_I(\psi) = \sin \psi$ at $G = 4.95$

occurs for this case (see Figure 5.2a), thus providing the maximum buoyancy force for flow convection in the annulus. Note that both cells are rotating in the same manner, clockwise. Unsteady results for this case using $\hat{G} = 4.99$ are discussed in section 5.2.3.

Kidney-shaped cellular patterns were also prevalent in cases c and d, where the upper half of the inner cylinder was cooled or heated while maintaining isothermal conditions ($T_I = 1$) on the lower half. Here,the cosine function was employed to produce the greatest nondimensional temperature diference between the inner and outer cylinders at $\psi = 180^\circ$, where $T_I(\pi) = 0$ for the cooled case (case d) and $T_I(\pi) = 2$ for the heated case (case c). As shown in Figures (A1 a - c) the effect of cooling on the upper half-cylinder was to shift the convective circulation toward the bottom of the annulus. The opposite effect occurs when the upper half-cylinder is heated (Figures A2 a - c). Increasing $\hat{G}$ from 3.0, increased the stream function strength but did not change the basic cell structure. Another type of flow field encountered was the formation of discrete counter-rotating cells induced by alternating hot and cold regions distributed evenly around the inner annulus wall. The temperature distribution of $T_I = -\cos(2\psi)$ shown in Figure 5.3a, produced the most complex of these multicellular flow patterns. Figures 5.3 b and c show the six-cell streamline contours for gap numbers of 3.0 and 4.40, respectively. Although the temperature peaks, which occur every 90 degrees, produce identical nondimensional inner and outer wall temperature differences of 1, the convective cells at $\psi = 90^\circ$ and $270^\circ$ are much larger than the other four. This phenomenon is due to the influence of buoyancy effects being strongest at these

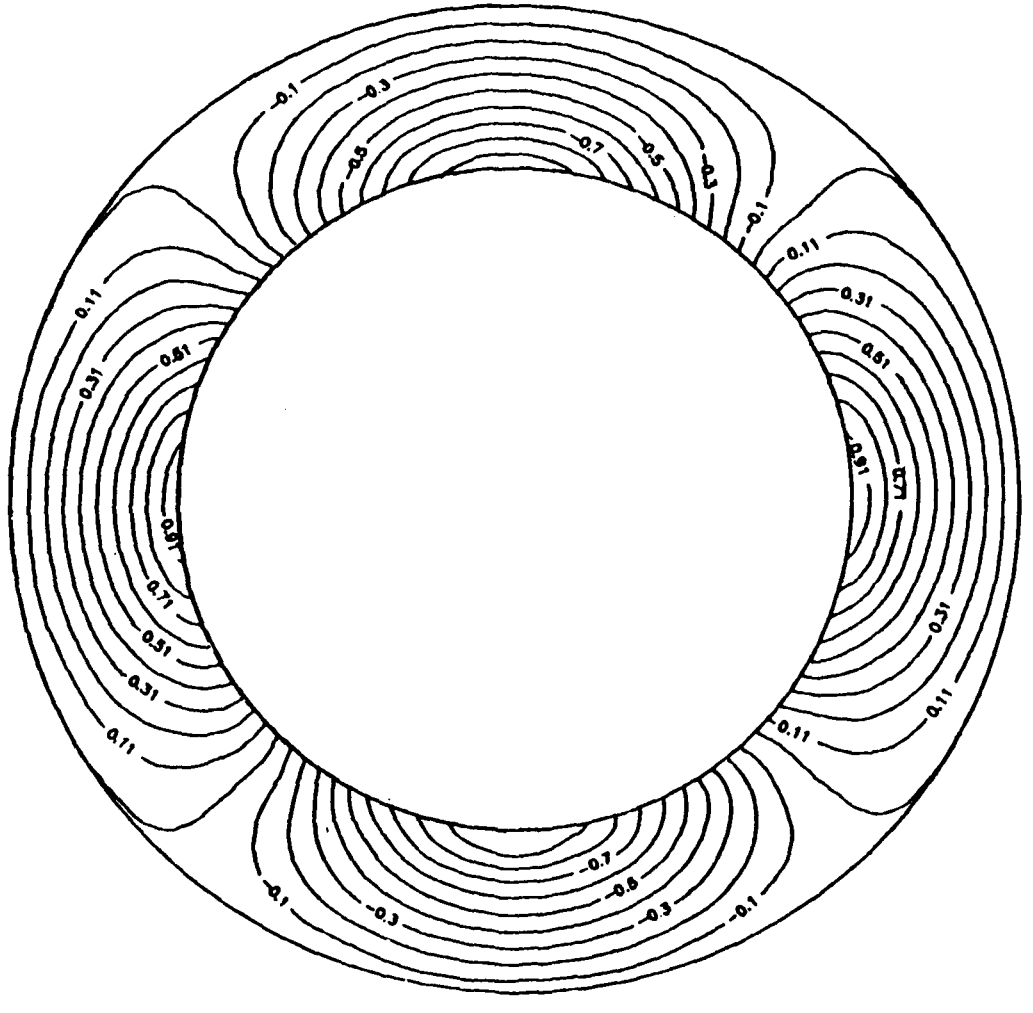


Figure 5.3a. Isotherms for $T_I(\psi) = -\cos(2\psi)$

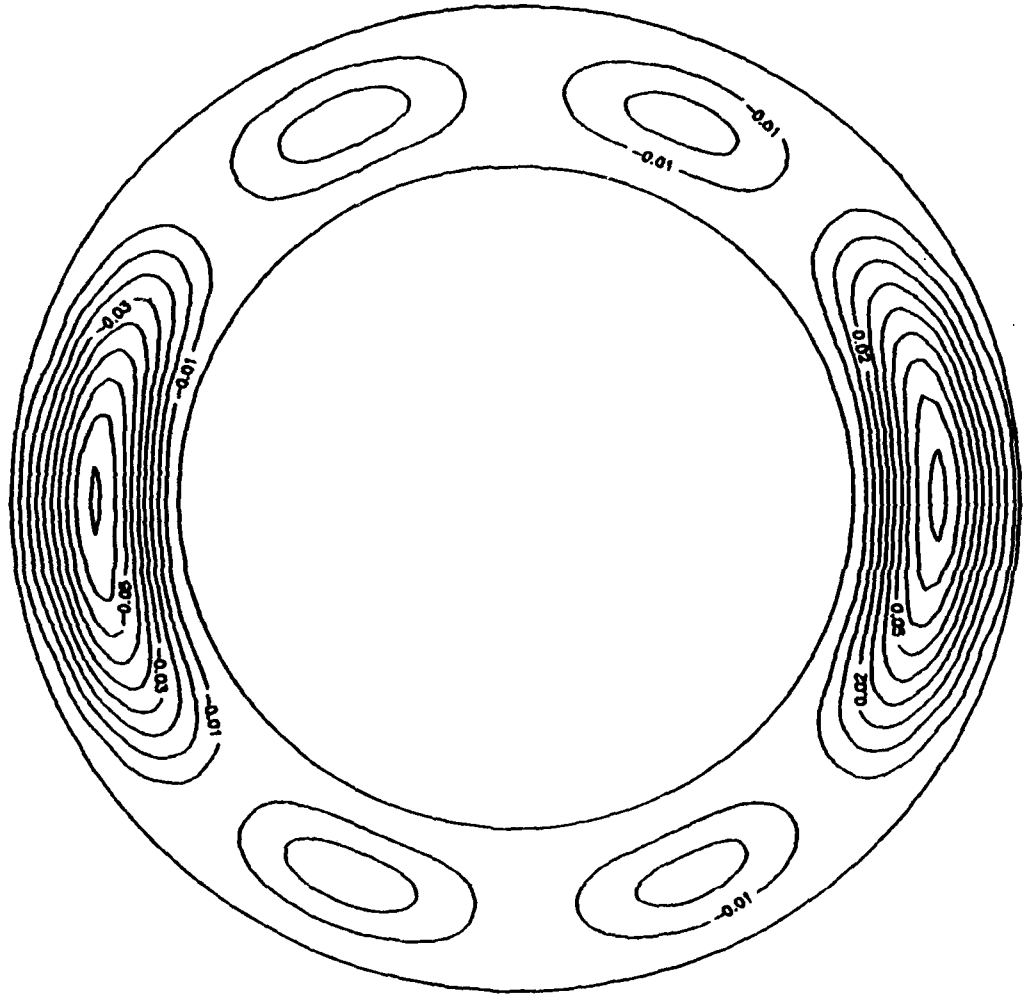


Figure 5.3b. Numerical streamlines for $T_I(\psi) = -\cos(2\psi)$ at $\hat{G} = 3.0$

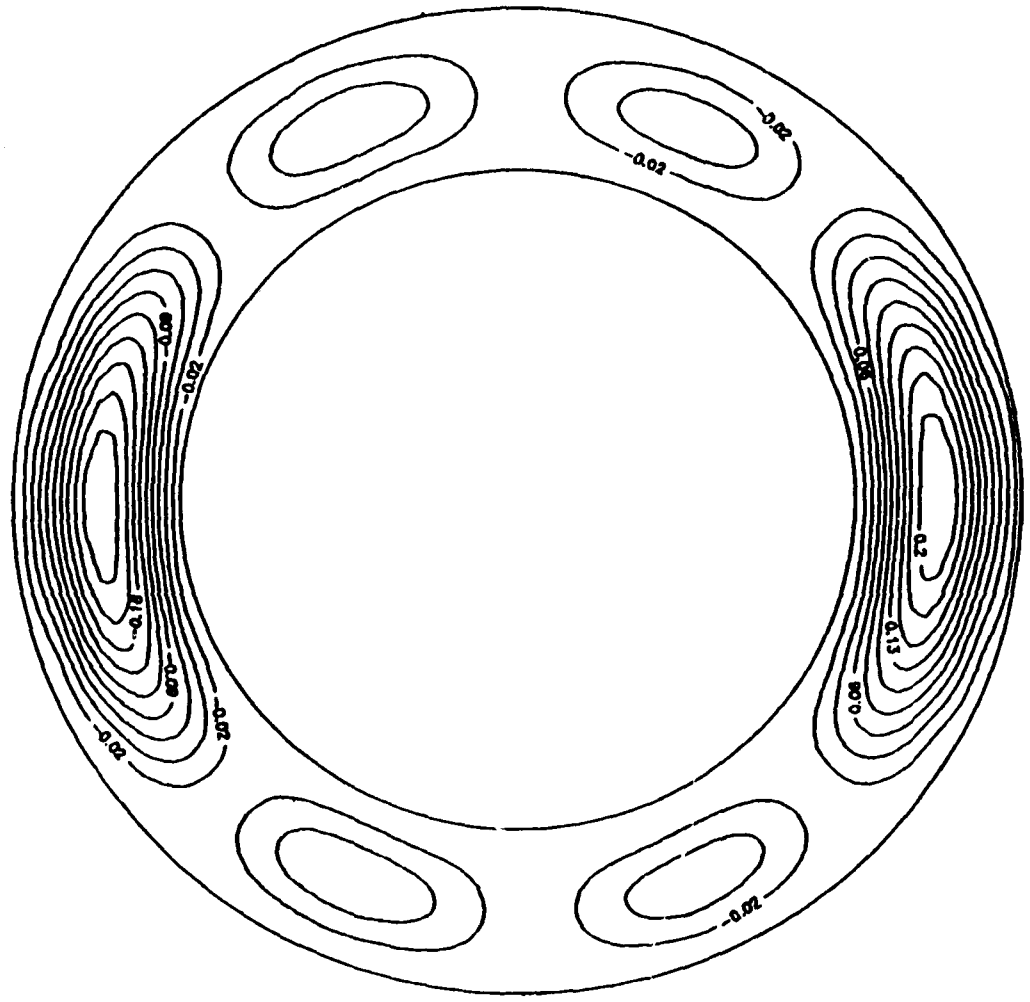


Figure 5.3c. Numerical streamlines for $T_I(\psi) = -\cos(2\psi)$ at $\hat{G} = 4.40$

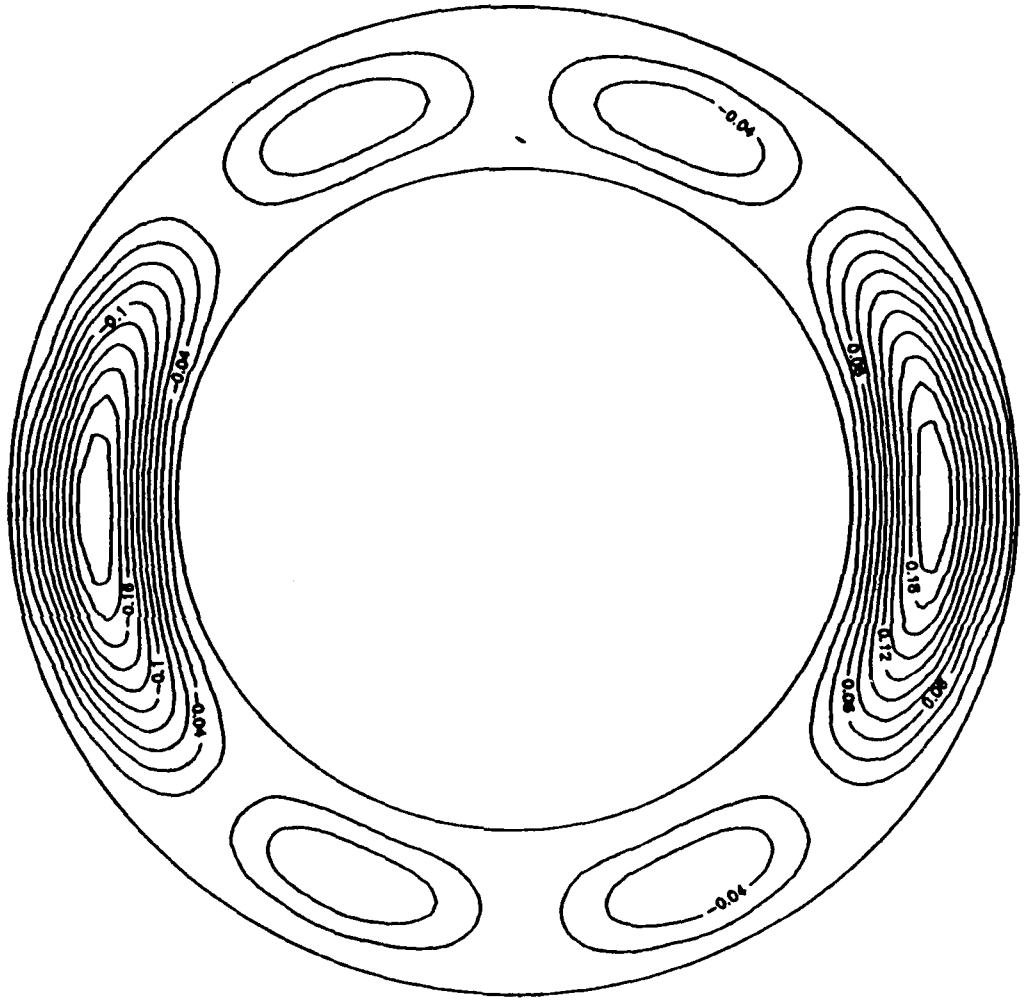


Figure 5.3d. Analytical streamlines for $T_I(\psi) = -\cos(2\psi)$ at $\hat{G} = 4.40$

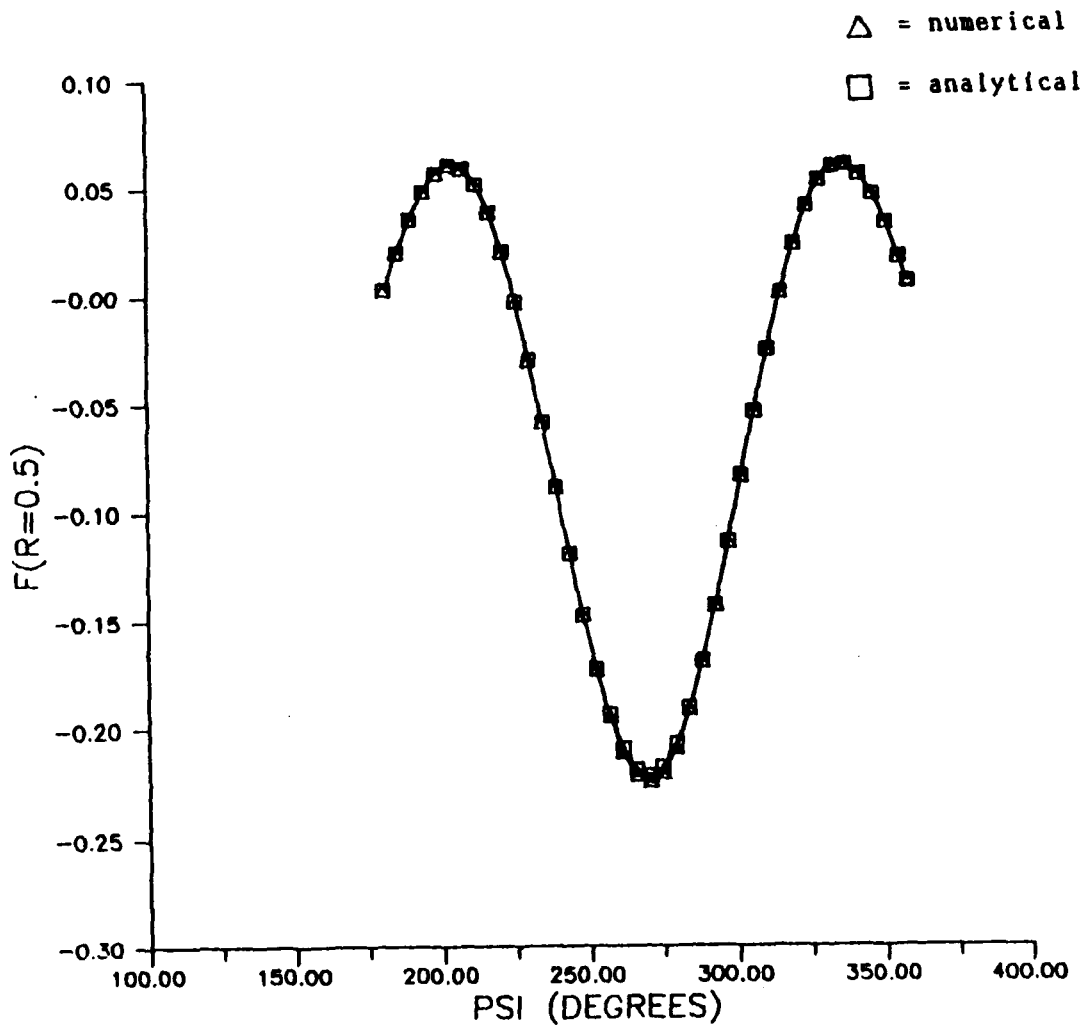


Figure 5.3e. Angular variation of the center-line stream function for $T_I(\psi) = -\cos(2\psi)$ at $G = 4.40$

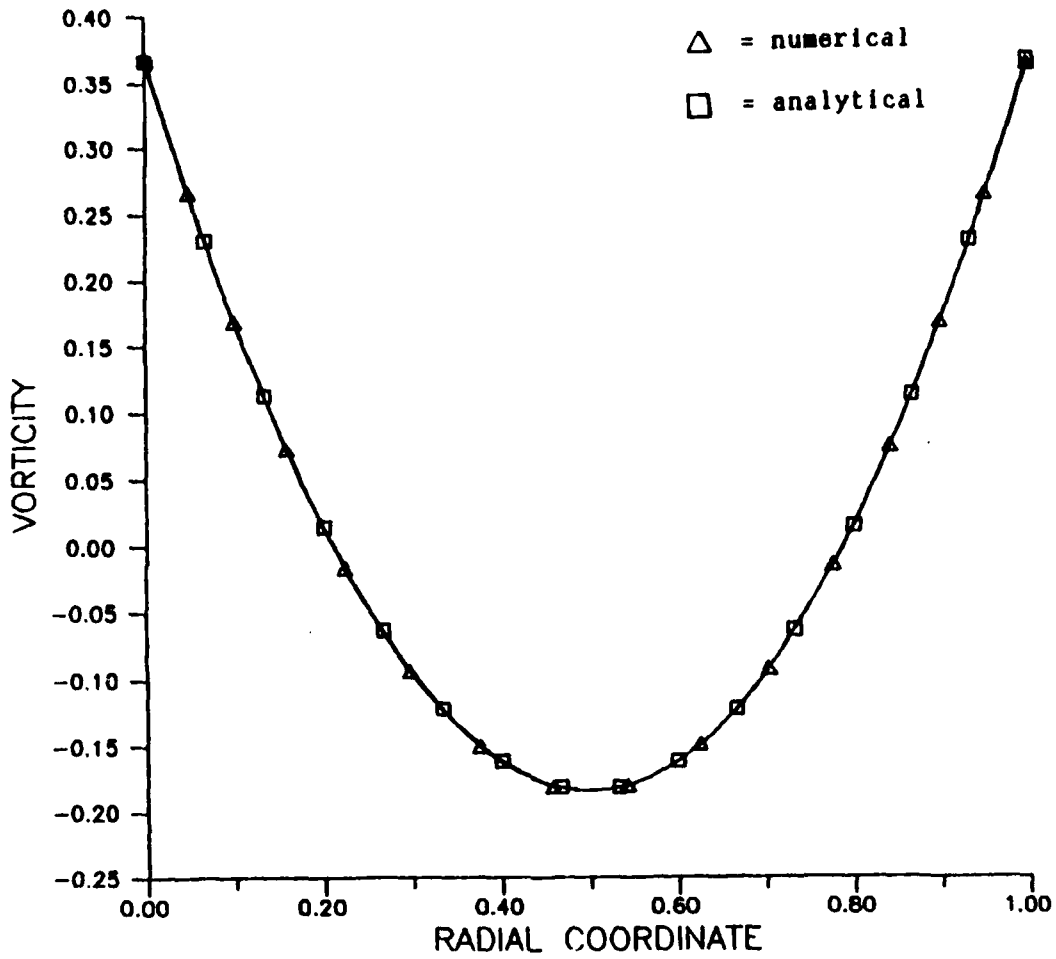


Figure 5.3f. Radial variation of vorticity at 90° for $\hat{G} = 4.40$
$T_I(\psi) = -\cos(2\psi)$

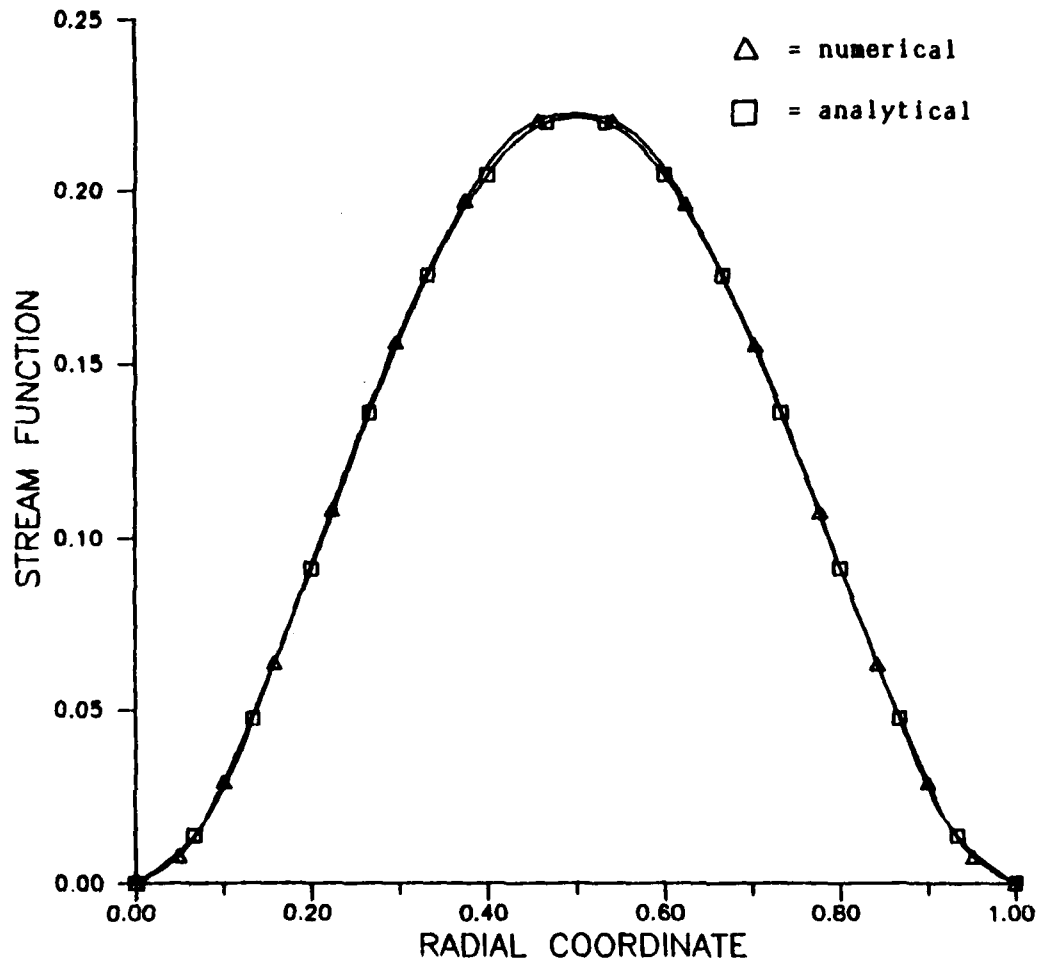


Figure 5.3g. Radial variation of the stream function at 90° for $\hat{G} = 4.40$
$T_I(\psi) = -\cos(2\psi)$

annular locations, as explicitly shown by the analytical result:

$$F_1 \propto \sin \psi \, (T_I(\psi)) \quad .$$

Also, vertical symmetry of the cell formation is recognized.

Other test cases exhibiting this flow behavior were the inner wall temperature distributions $T_I = -\cos \psi$ and $T_I = \cos \psi$, which produced four counter-rotating cells of equal size and strength. No cells were predominantly larger due to the equal buoyancy influence at each cellular location in the annulus. Unlike $\sin \psi$, the $\cos \psi$ temperature distribution did not induce a more complex multicellular flow field when the unsteady flow transition point was reached at $\hat{G} = 5.75$. The isotherm and streamline contour plots for $T_I = \cos \psi$ and $T_I = -\cos \psi$ are found in Appendix A (Figures A3 a - c and A4 a - c).

The test cases involving more localized temperature changes on an otherwise isothermal inner cylinder (cases g - j), model hot and cold spots near the top of the annulus. Case i models a triple hot spot distribution symmetric about $\psi = 180^\circ$, where a temperature peak of 2.5 is reached. Two secondary peaks of 1.8 are located $\pm 22^\circ$ from the vertical symmetry line (see Figure 5.4 a). As shown in Figures 5.4 b and c, these hot spots induce the beginnings of a secondary cell formation near the top of the annulus. This flow field is similar to the isothermal case, except for this localized increased convective activity.

The cold spot of case j (Figure 5.5 a) gives rise to a thermal instability of two discrete counter-rotating cells near the top of the annulus. As gap number is increased from 3.0 to 4.40, these small cells become stronger as does the larger kidney-shaped cells which dominate the

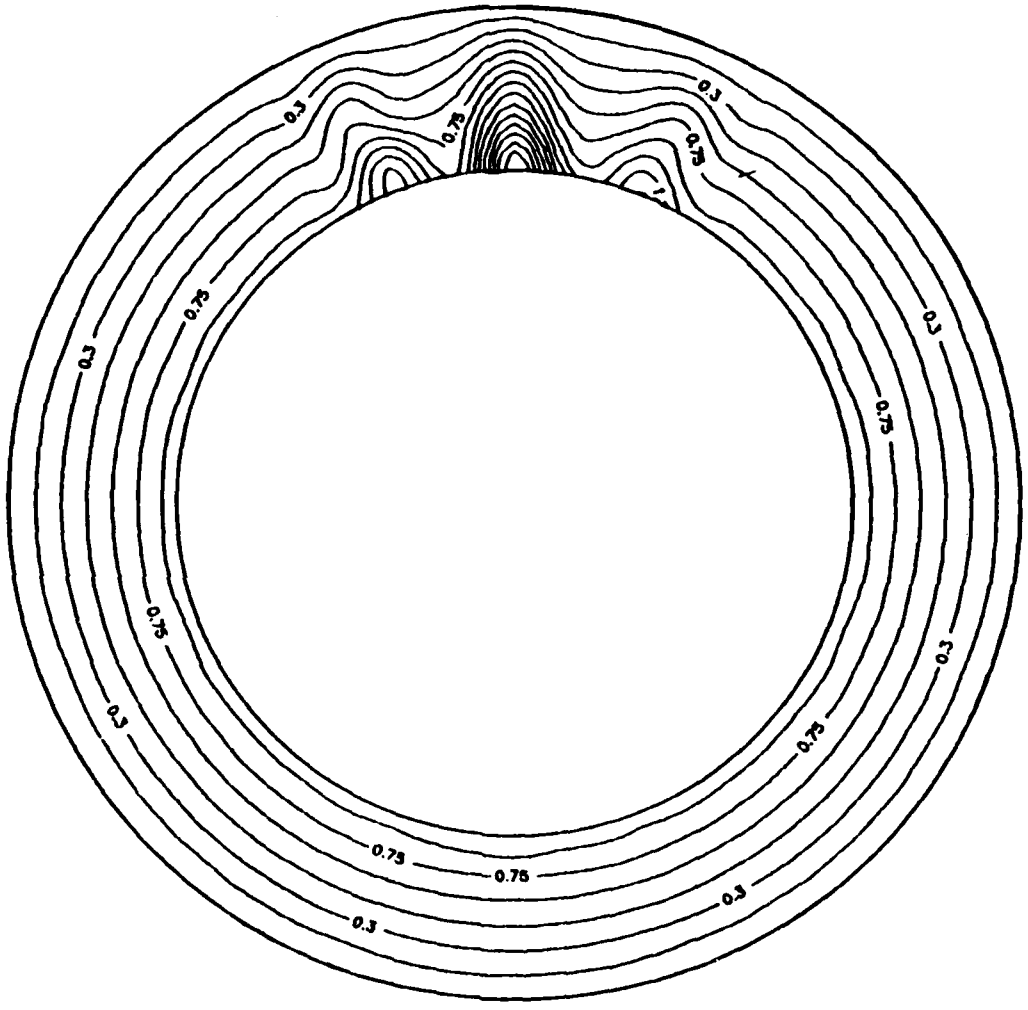


Figure 5.4a. Isotherms for the triple hot spot distribution

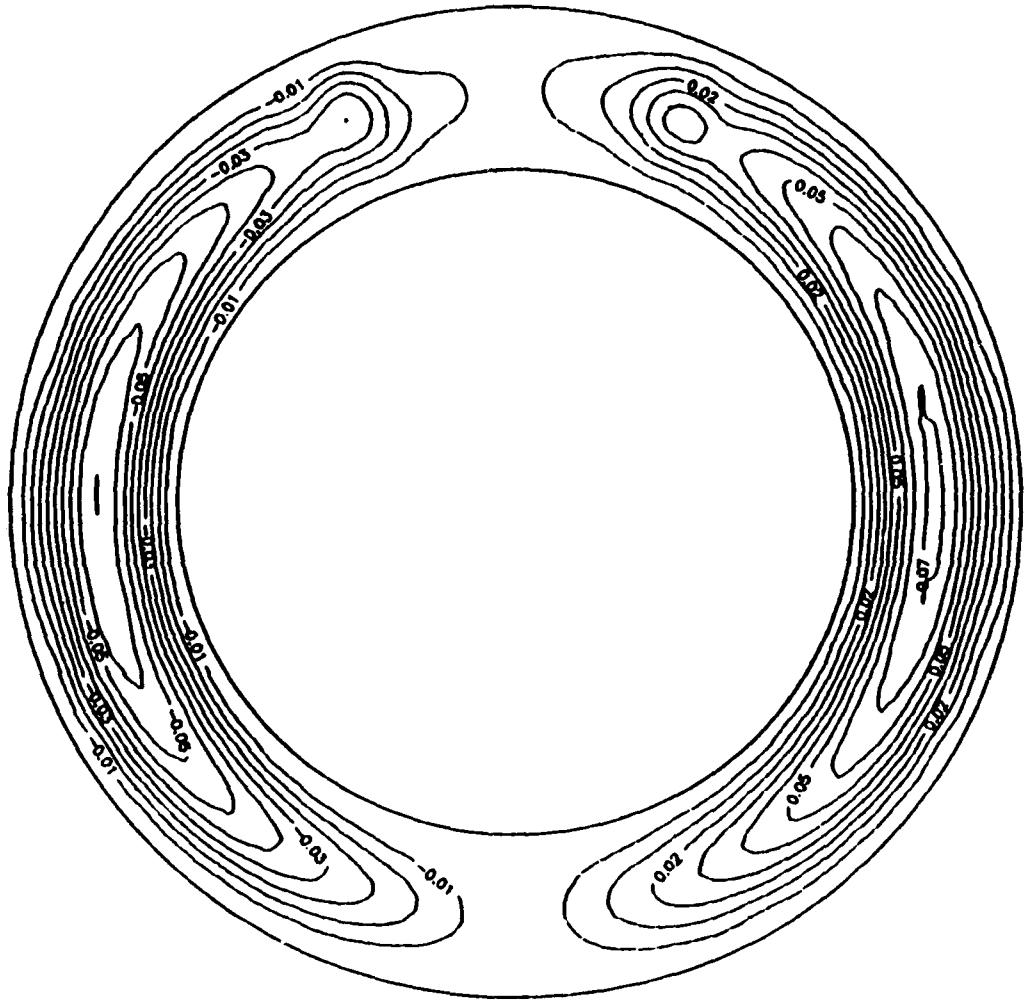


Figure 5.4b. Numerical streamlines at $\hat{G}$ = 3.0 for the triple hot spot distribution

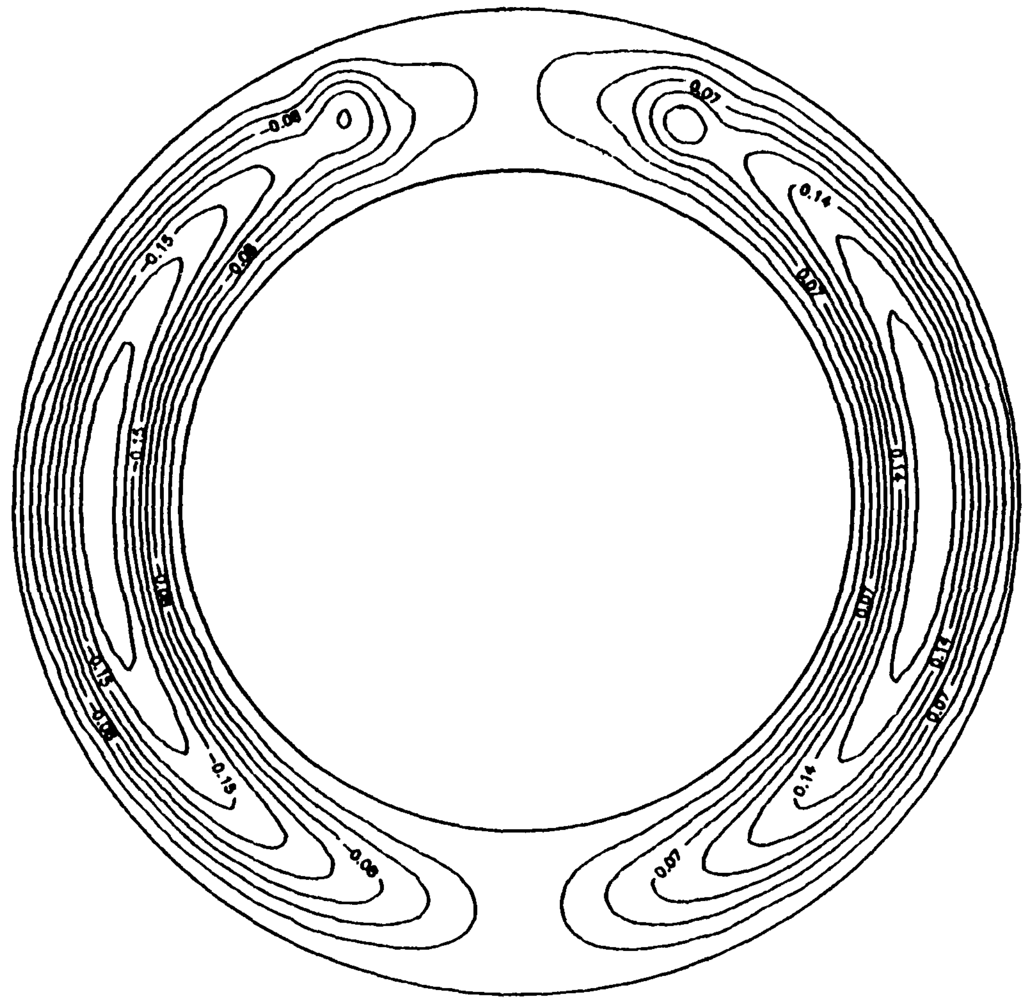


Figure 5.4c. Numerical streamlines at $\hat{G} = 4.40$ for the triple hot spot distribution

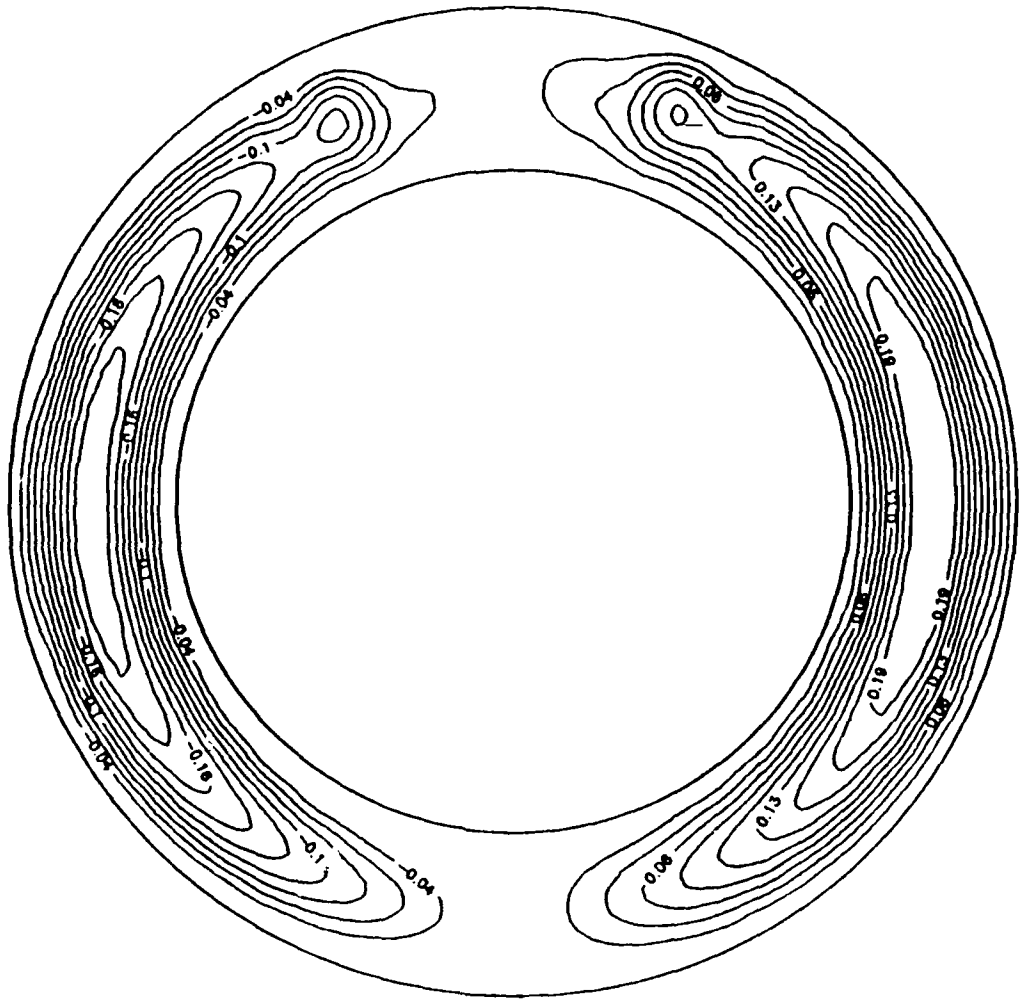


Figure 5.4d. Analytical streamlines at $\hat{G}$ = 4.40 for the triple hot spot distribution

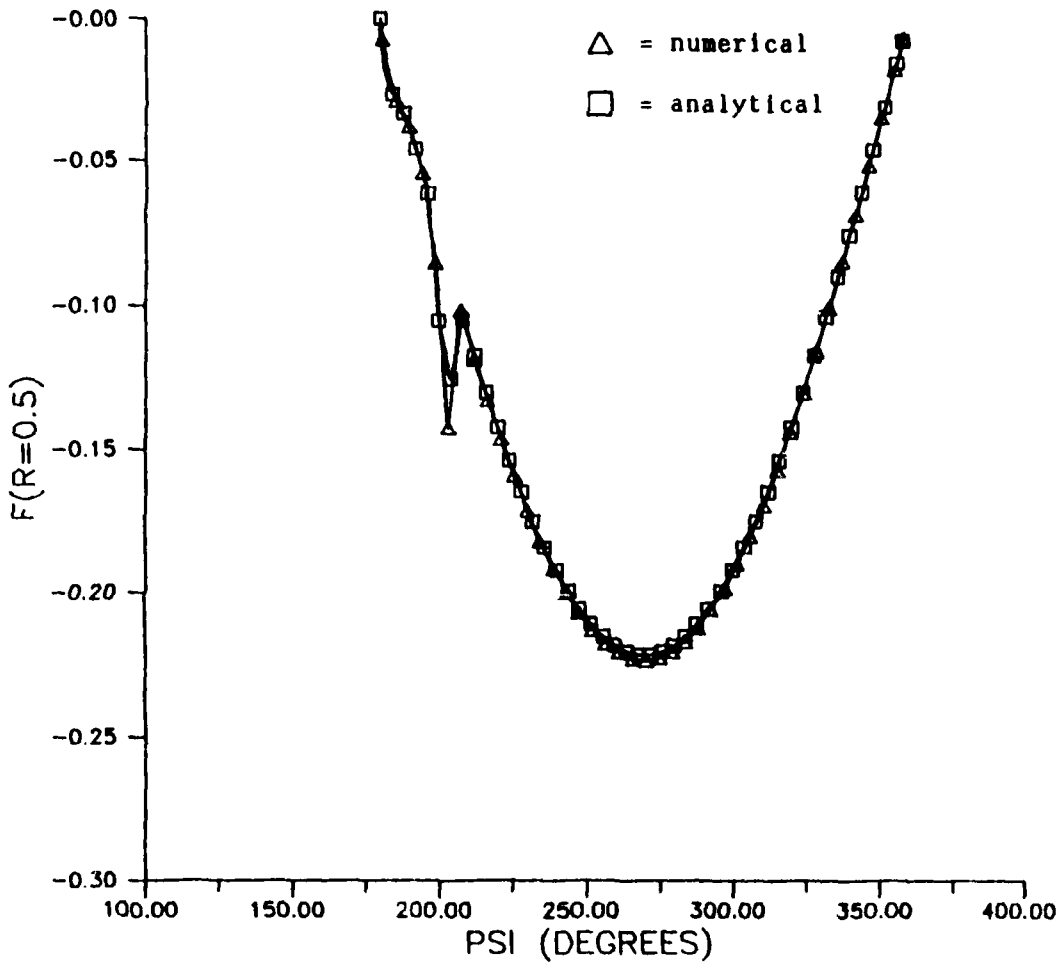


Figure 5.4e. Angular variation of the center-line stream function at $\hat{C}$ = 4.40 for the triple hot spot distribution

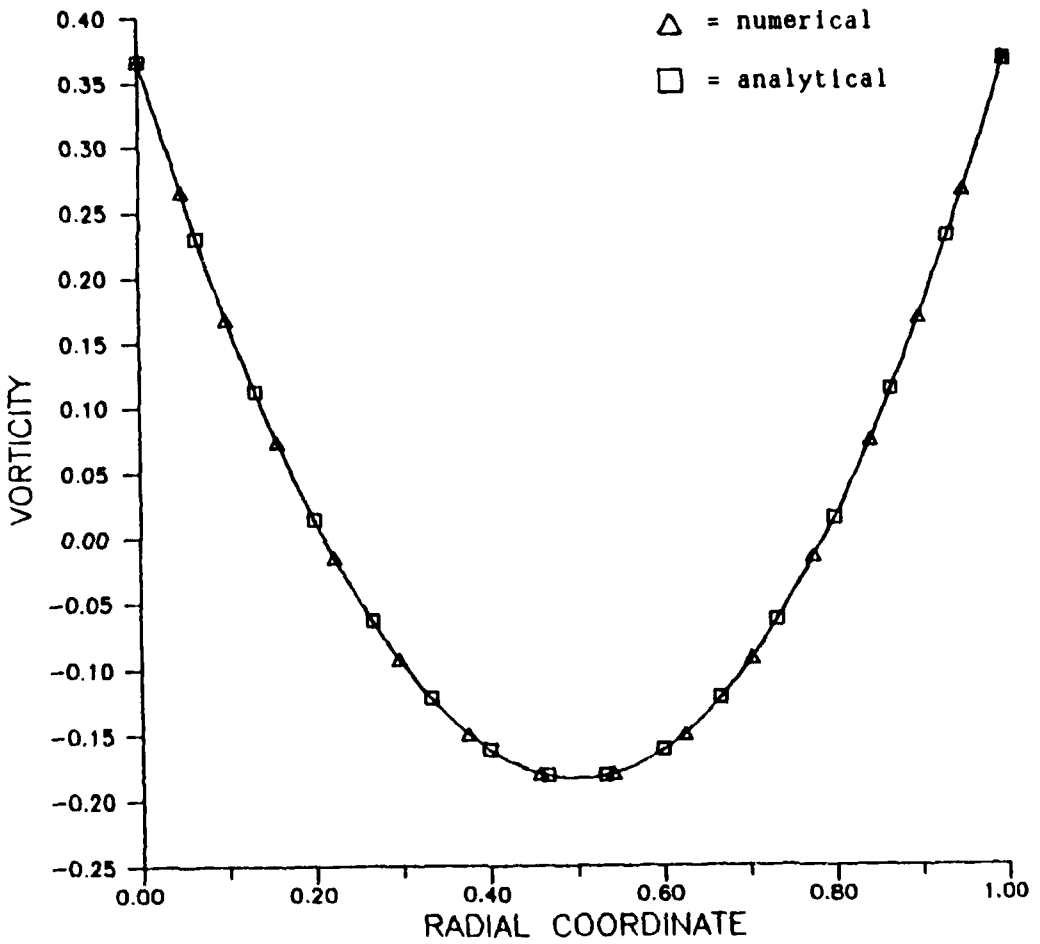


Figure 5.4f. Radial variation of vorticity at 90° for $\hat{G}$ = 4.40 for the triple hot spot distribution

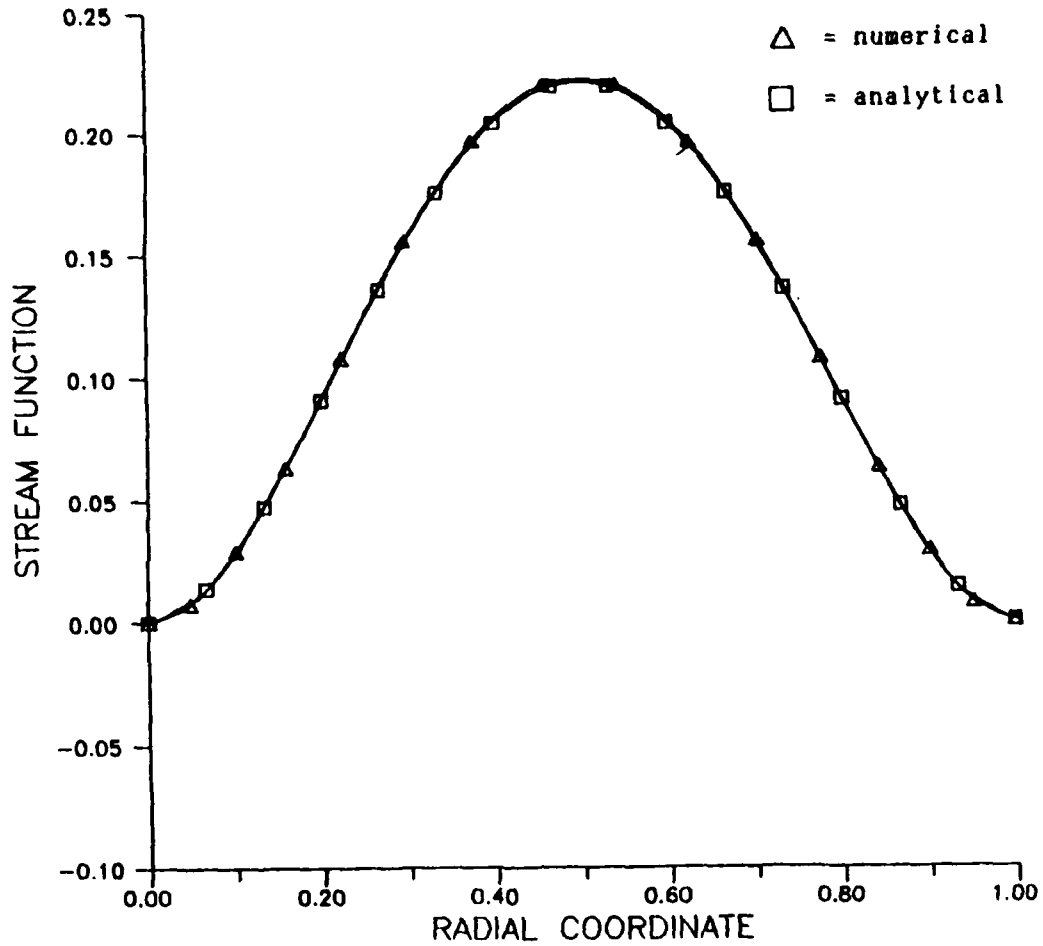


Figure 5.4g. Radial variation of the stream function at 90° for $\hat{G}$ = 4.40 for the triple hot spot distribution

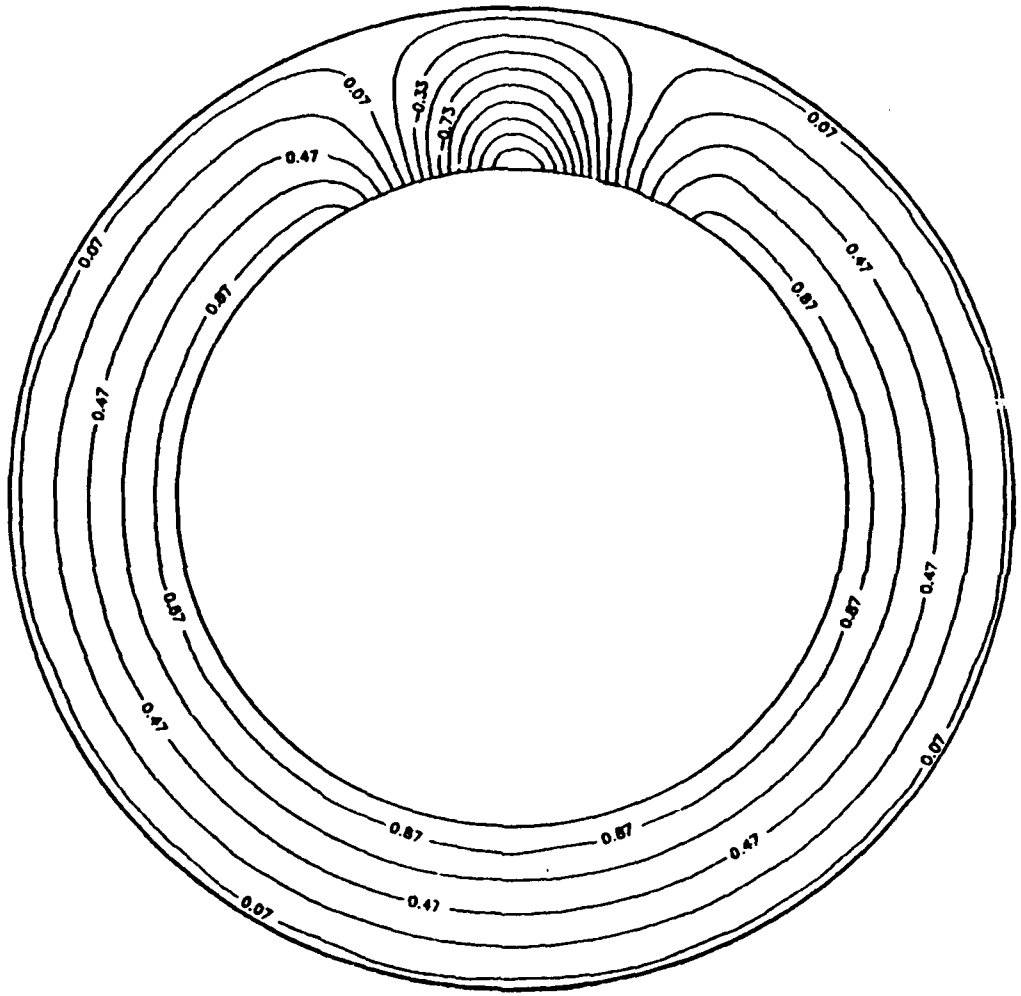


Figure 5.5a. Isotherms for the cold spot condition

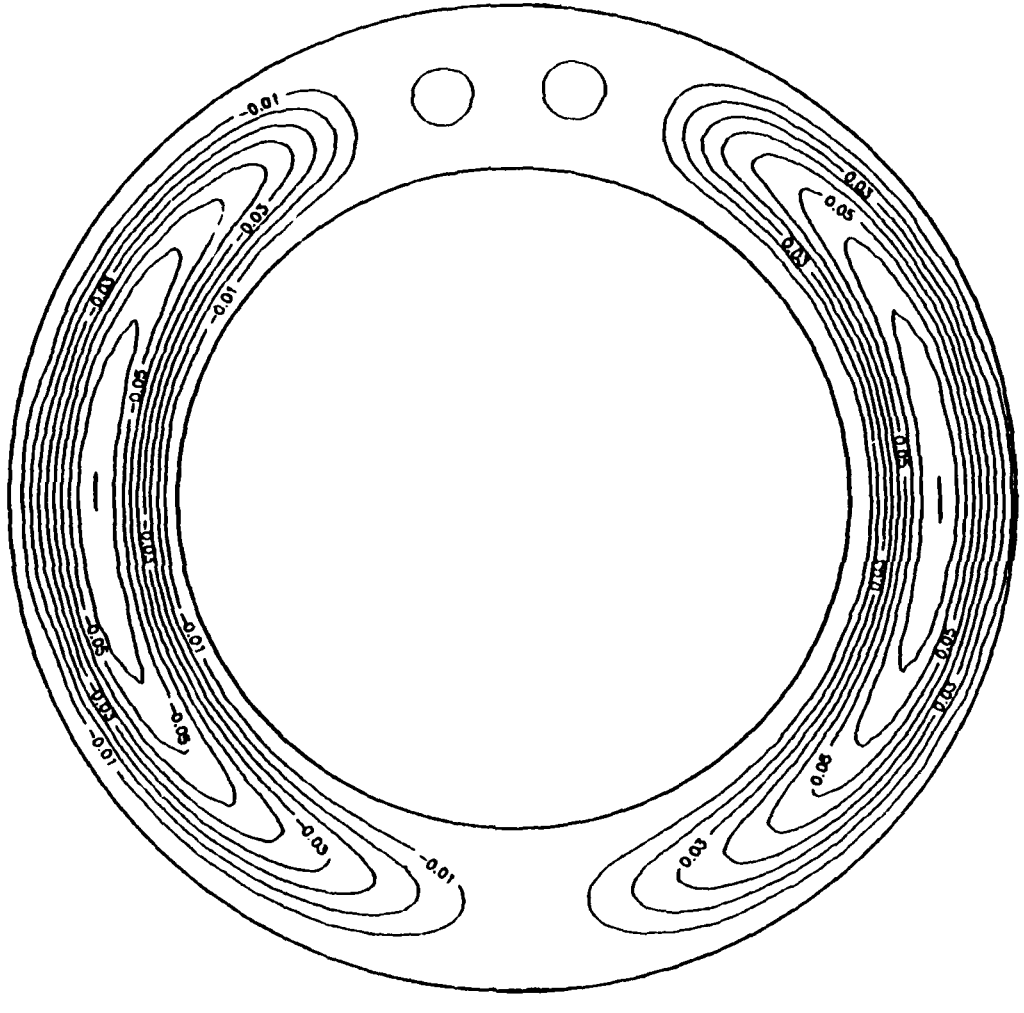


Figure 5.5b. Numerical streamlines for the cold spot condition at $\hat{G}$ = 3.0

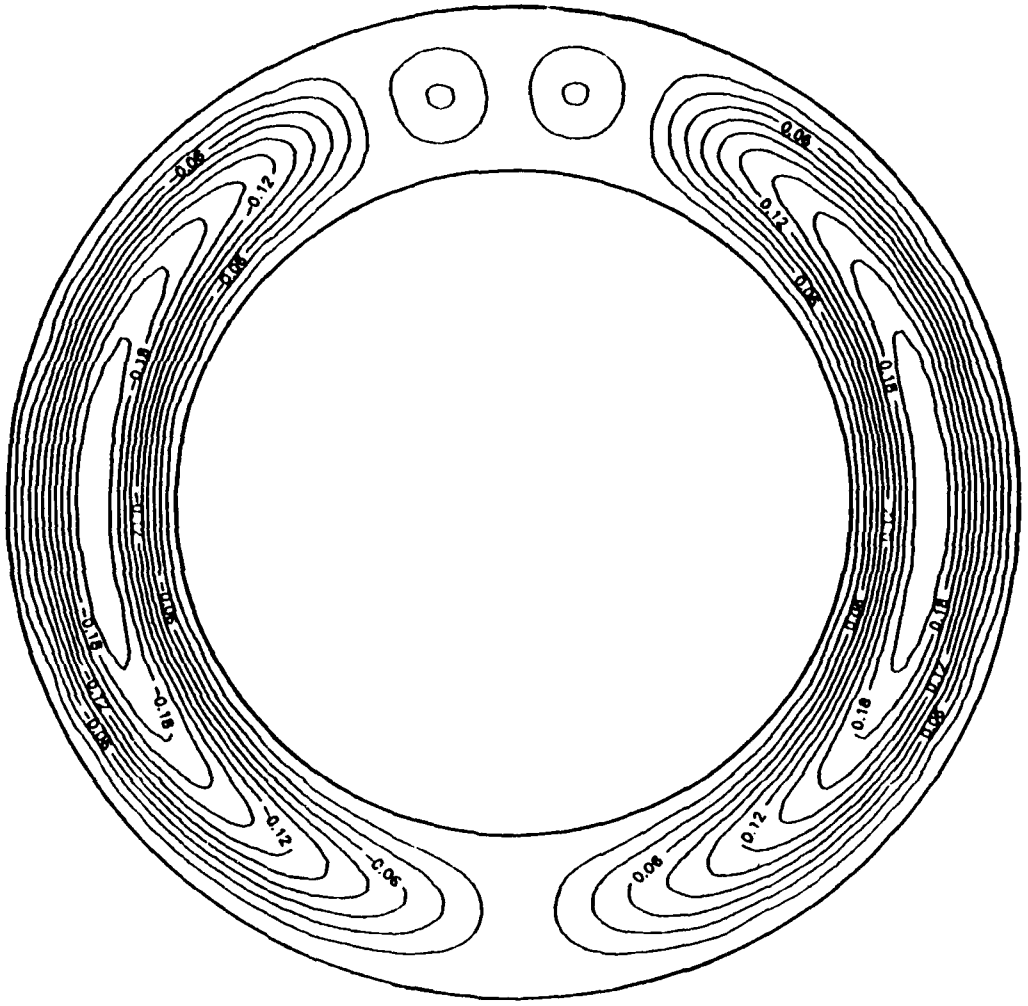


Figure 5.5c. Numerical streamlines for the cold spot condition at $\hat{G}$ = 4.40

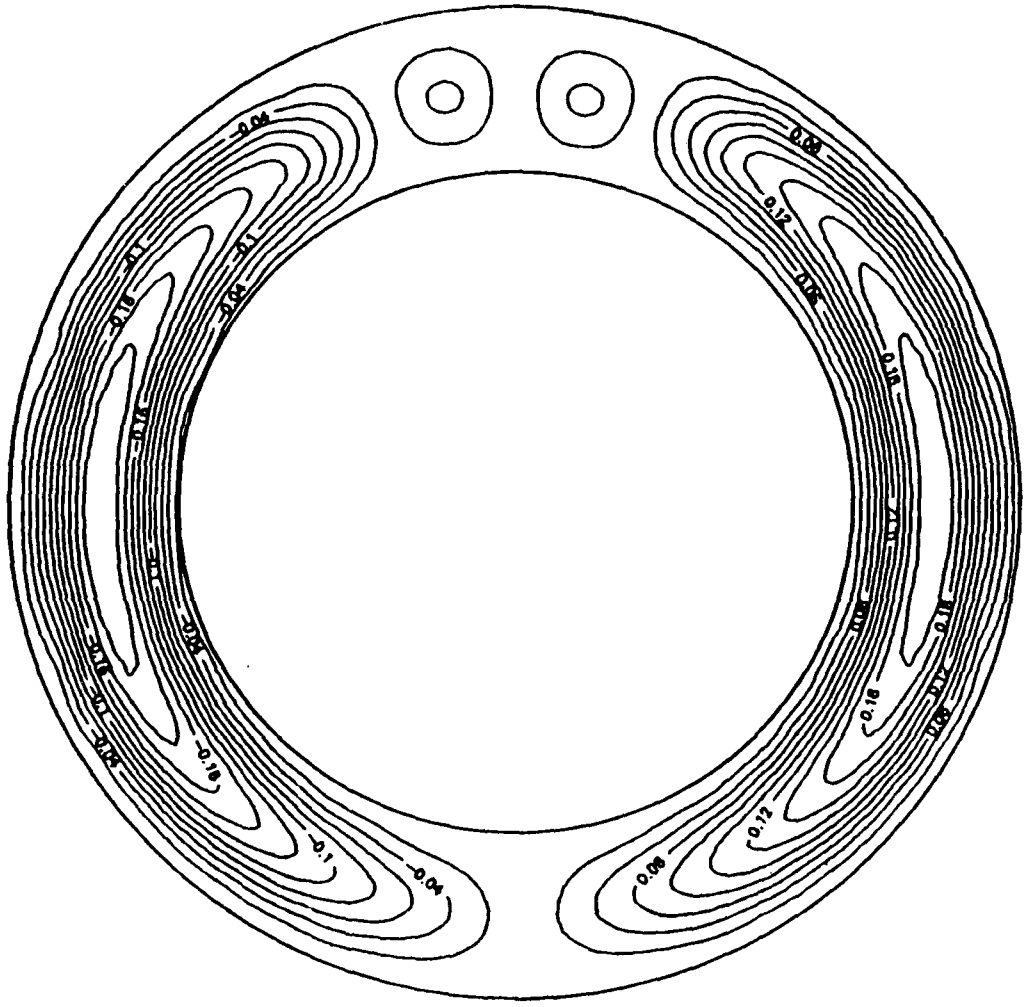


Figure 5.5d. Analytical streamlines for the cold spot conditon at $\hat{G}$ = 4.40

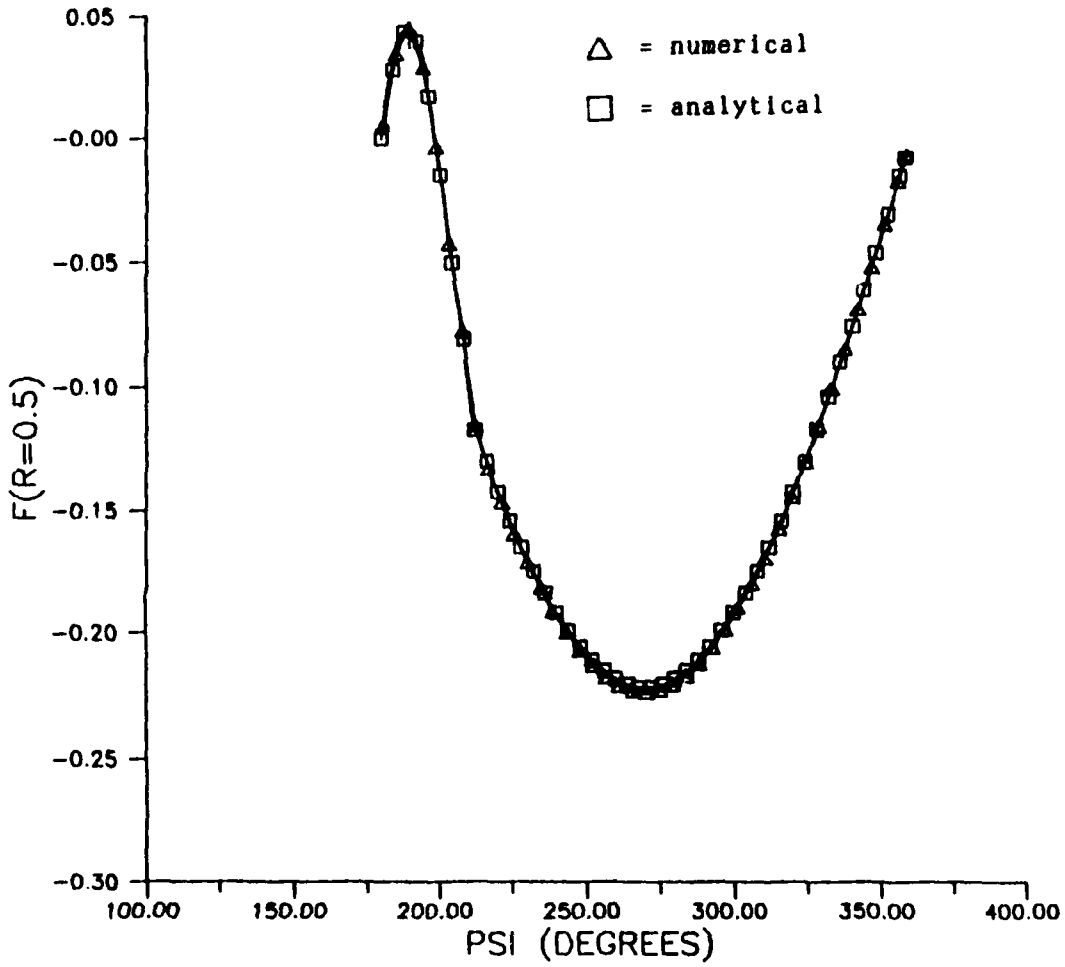


Figure 5.5e. Angular variation of the center-line stream function at $\hat{G}$ = 4.40 for the cold spot condition

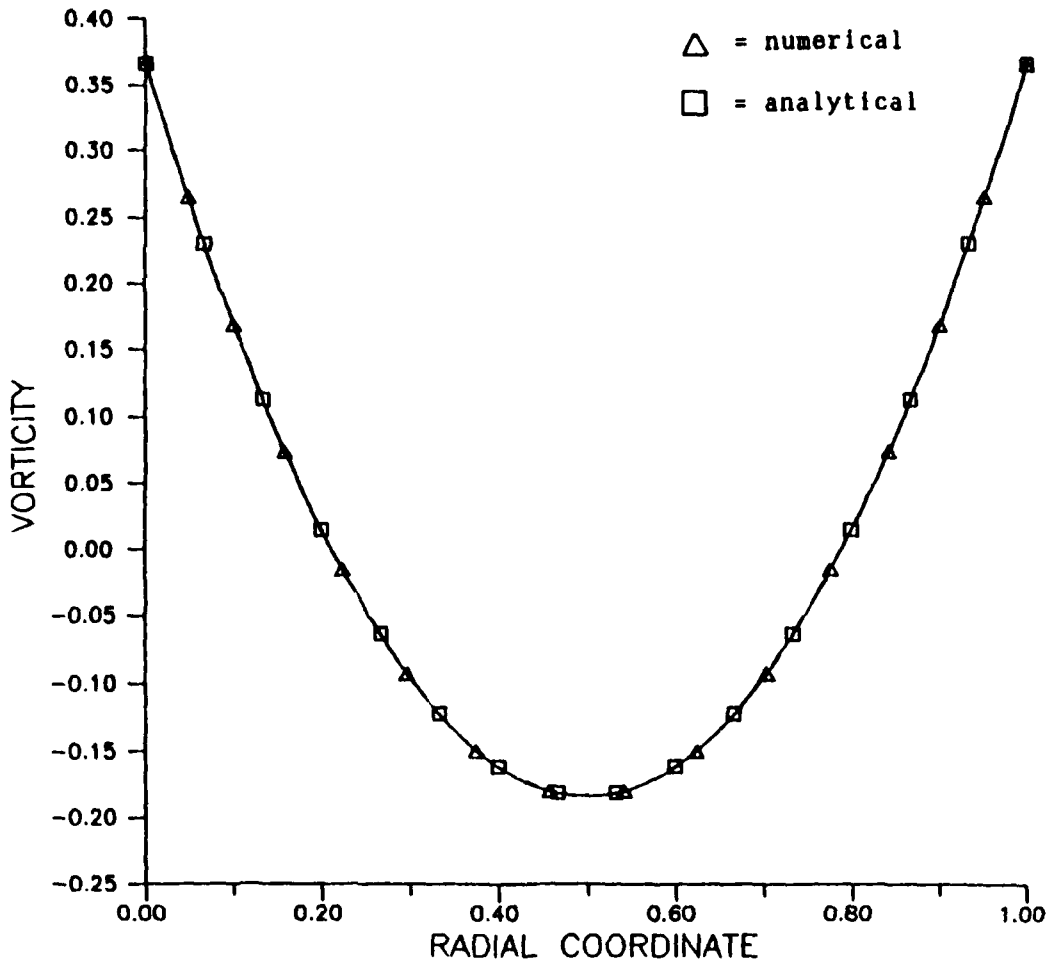


Figure 5.5f. Radial variation of vorticity at 90° for $\hat{G}$ = 4.40 for the cold spot condition

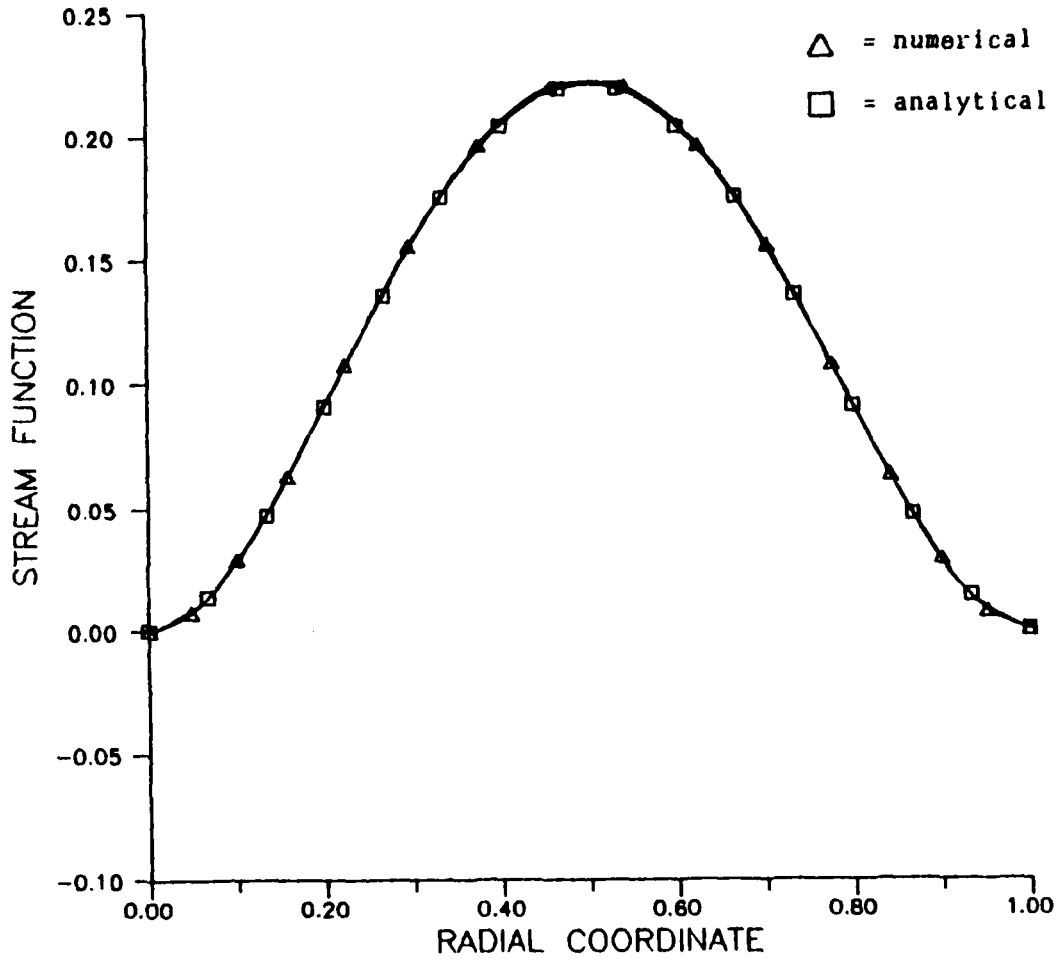


Figure 5.5g. Radial variation of the stream function at 90° for $\hat{G}$ = 4.40 for the cold spot condition

flow field (see Figures 5.5 b and c). Note that this convective behavior resembles the thermal instability of air (Pr = .7) in an isothermally heated narrow annulus.

Cases g and h, presented in Figures A5 a - c and A6 a - c in Appendix A, model single and dual hot spots, respectively. These temperature distributions produce simply an elongation of the upper portion of the kidney-shaped counter-rotating cells. Strong secondary cell formation does not occur as in case i, where the sharp central peak contributes to this condition. As with cases i and j, increasing gap number to 4.40 only increases the stream function strength without altering the basic cell pattern.

Analytical Comparison. The analytical perturbation expressions derived in Chapter III, from the zero-Prandtl number boundary-layer equations were used as checks to the steady-state numerical results. These comparisons support both the flow fields found by the numerical procedure and the analytical analysis itself.

The two-term perturbation expressions for stream function and vorticity were used to generate comparative data for the pretransitional numerical results. Stream function and vorticity were compared at the angular coordinate where maximum stream function occurred for $0 \leq r \leq 1$. Comparison of stream function data was also made at the annulus centerline ($r = .5$) for $180^\circ \leq \psi \leq 360^\circ$. For each test case, the comparative data was generated for the largest gap number used in the numerical analysis of section 5.2.1.

The temperature distribution, $T_I(\psi) = \sin \psi$, demonstrates the limits of the analytical formulation in describing pretransitional flows.

Figure 5.2 d shows how the analytically generated streamlines for $\hat{G} = 4.95$ resemble the numerical result of $\hat{G} = 4.93$ (Figure 5.2 b), while failing to capture the numerically-generated multicellular flow structure of Figure 5.2 c (for $\hat{G} = 4.95$). Figures 5.2 e - g explicitly show the analytical agreement with $\hat{G} = 4.93$ numerical data, while Figures 5.2 h -j highlight the descrepancies in the $\hat{G} = 4.95$ results. analytical vs. numerical comparison plots for stream function and vorticity (Figures h and i) indicate significant differences in the solution where stream function strength is maximum. This difference is also seen along the centerline (Figure 5.2 j) where descrepancies exist for $225^\circ \leq \psi \leq 300^\circ$. This is the multicellular region which could not be resolved by the two-term perturbation result.

All other cases exhibited very close agreement when comparing analytical and numerical solutions, except for case c; the cooled upper half-cylinder. As Figures A1 d - g show, the descrepancies were not as dramatic as the sin $\psi$ case, particularly for the centerline comparison. These descrepancies were due to the use of the transitional gap number for this case ($\hat{G} = 4.71$) to generate comparison data. Although the cos $\psi$ test case was evaluated at its transitional gap number (as sin $\psi$ was for $\hat{G} = 4.95$), no discernable differences in the data was noted. From this, one might conclude that discrete, counter-rotating cells tend to stabilize the flow field compared to the kidney-shaped cell pattern. since the comparison data for the other seven cases were within the steady-state or pretransitional zone, no descrepancies were found (as expected). The comparison plots are included with each test case following the flow field contour plots.

Unsteady Results. Only the sin $\psi$ inner cylinder temperature distribution was numerically studied in the unsteady flow regime. As mentioned in section 5.2.1, a gap number of 4.99 induced unsteady flow behavior in the annulus. The solution was carried out to $\hat{t}$ = 1000 to further study this unsteady development. Flow field plots, corresponding to $\hat{t}$ = 200, 400, 600 and 800 are presented in Figures 5.6 a - d. As time progressed, the weaker cells diminished and softened in structure. Then, as seen in Figure 5.6d, some re-strengthening of the cell pattern occurred near $\hat{t}$ = 800. Due to time considerations (on the average, 200 time steps required 4 hours of CPU time), the solution was not carried out further to determine if this cyclic-like flow behavior persisted. Although, it appears that some type of cellular structure interaction is occurring in the vertical portion of the annulus.

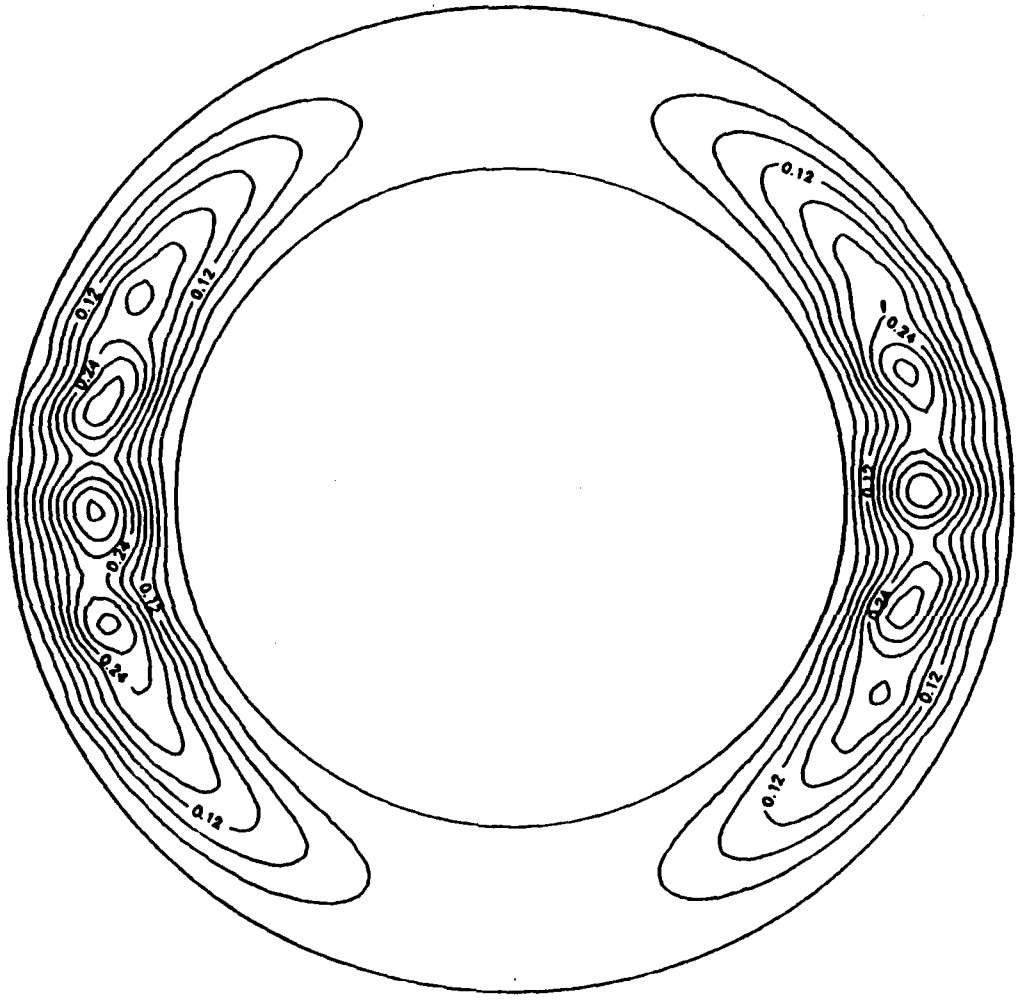


Figure 5.6a. Unsteady flow field at $\hat{t} = 200$, $\hat{G} = 4.99$, $T_I(\psi) = \sin \psi$

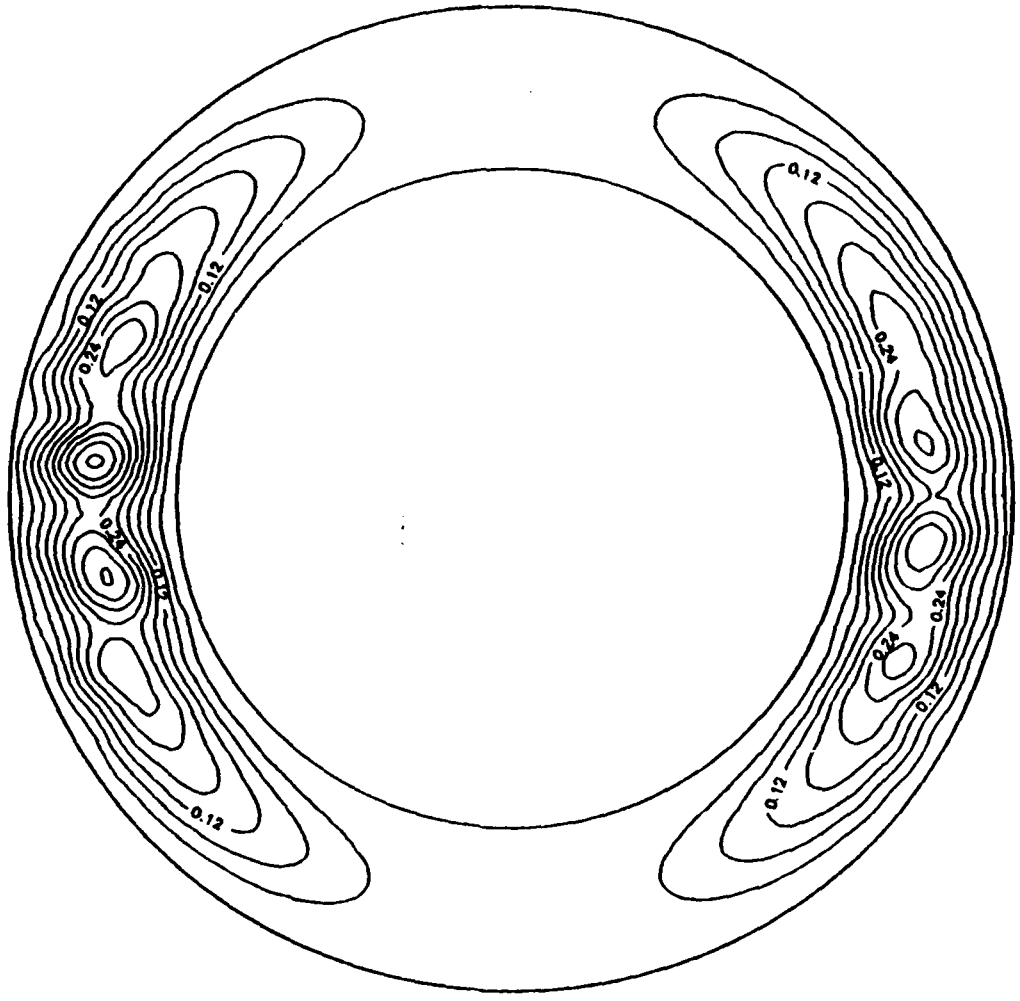


Figure 5.6b. Unsteady flow field at $\hat{t} = 400$, $\hat{G} = 4.99$, $T_I(\psi) = \sin \psi$

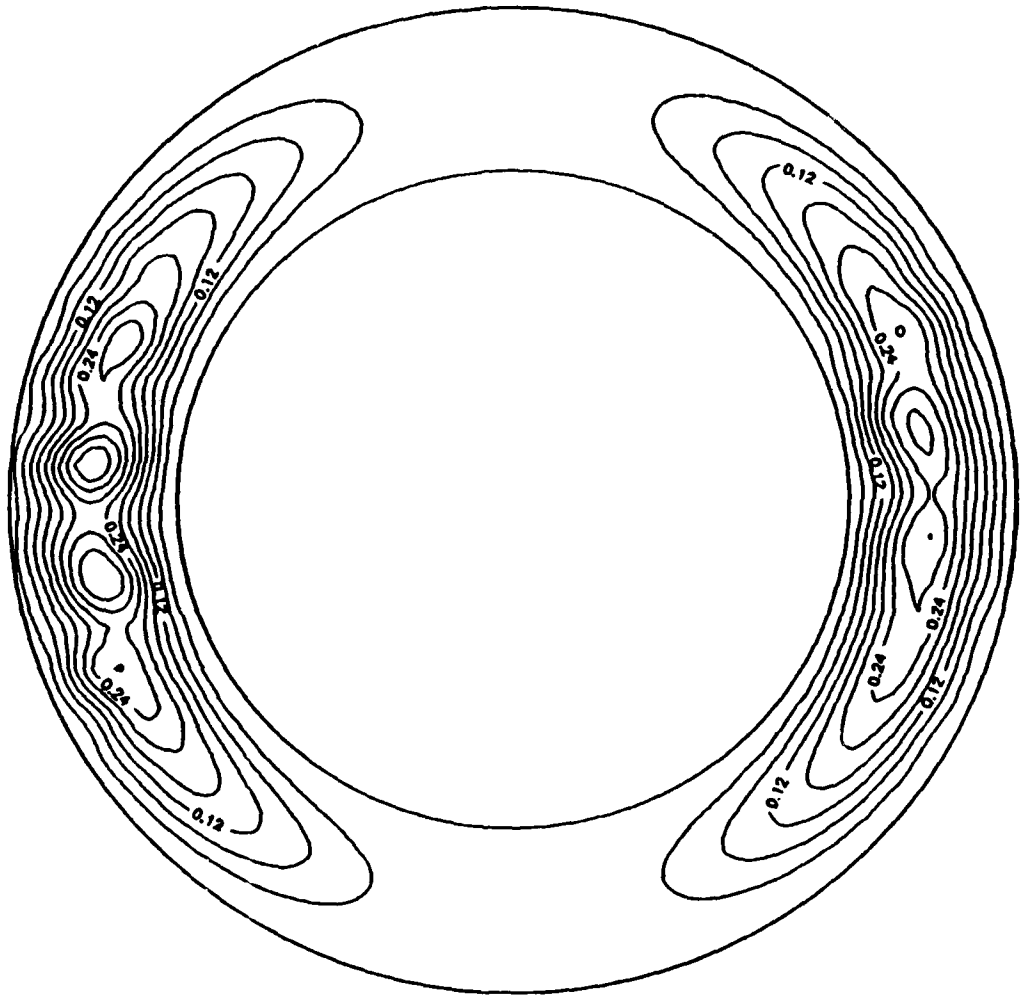


Figure 5.6c. Unsteady flow field at $\hat{t} = 600$, $\hat{G} = 4.99$, $T_I(\psi) = \sin \psi$

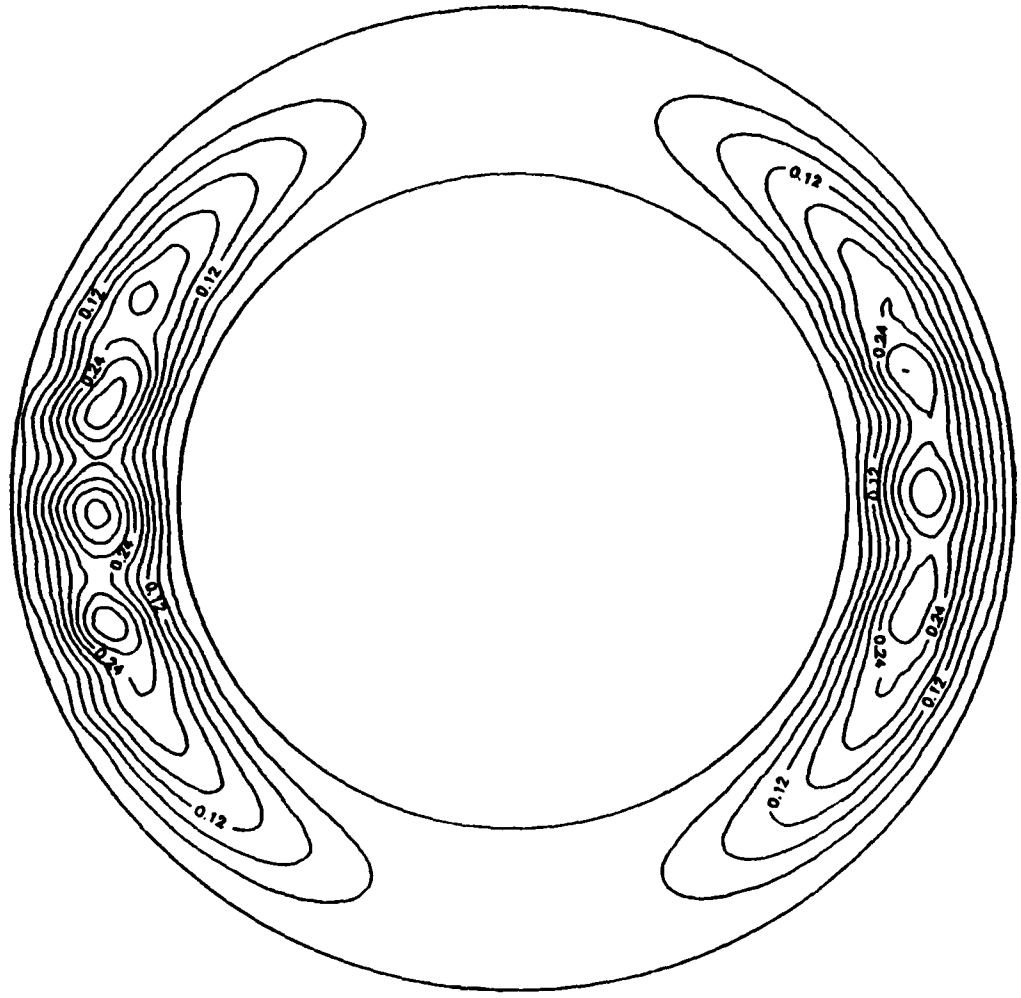


Figure 5.6d. Unsteady flow field at $\hat{t} = 800$, $\hat{C} = 4.99$, $T_I(\psi) = \sin \psi$

## VI. Conclusions and Recommendations

The influence of variable inner wall temperature distributions have direct effects on the formation of multicellular convection flows in narrow horizontal concentric annuli for both steady-state and unsteady flow regimes. For most test cases examined in this study, the two-term analytical perturbation expressions of Chapter III provided excellent agreement with pretransitional numerical results for steady-state flows. These solutions begin to diverge, however, when the point of transition to the unsteady flow regime is reached, as shown explicitly by the sin $\psi$ test case of chapter V. This is to be expected, since the analytical formulation is derived on the assumption of steady-state conditions and cannot capture any time-dependent multicellular flow field behavior. These solutions are therefore best suited for quick flow field visualization of steady-state convection in the annulus subject to variable inner wall temperature conditions.

Abrupt temperature changes on the upper cylinder surface (hot or cold spots) give rise to small, discrete convective cells, especially in the horizontal section of the annulus, which resemble thermal instabilities characteristic of air in a narrow horizontal enclosure. This is in contrast to the instability formed in the vertical portions of the annulus by isothermal or gradually-varying inner wall temperature conditions. This instability is hydrodynamic in origin, induced by buoyancy forces.

In the context of a simplified set of governing equations, one can obtain a multitude of cellular structures in the annular flow field.

Such complex convective flow behavior may enhance heat transfer of systems employing the concentric cylinder geometry for cooling or insulation purposes. Understanding the inner wall conditions that cause such phenomenon is central to this analysis.

In order to gain further insight into the formation of discrete multicellular steady-state flow fields, more studies are recommended in the pretransitional regime using a variety of hot and cold spots on the lower and side portions of the inner cylinder. In addition, more numerical work should be performed in the unsteady and transitional flow regimes for a variety of inner cylinder temperature distributions to study the nature of unsteady multicellular instabilities. Experimental studies of low Prandtl-number fluid convection are strongly recommended for the narrow-gap concentric cylinder geometry with variable inner wall temperature conditions to verify the limited numerical work performed in this area.

Additional numerical and analytical work is also recommended to study how finite Prandtl-number fluids effect the solutions obtained for the test cases examined in this thesis. Such research would offer insight into the behavior of viscous fluids under variable inner wall temperature boundary conditions within a narrow annular enclosure.

Finally, a parametric study of the numerical grid could be performed to see how grid density affects the flow field solutions, perhaps indicating an optimal configuration for resolving multicellular flow behavior.

# Appendix A

## Supplementary Flow Field Data

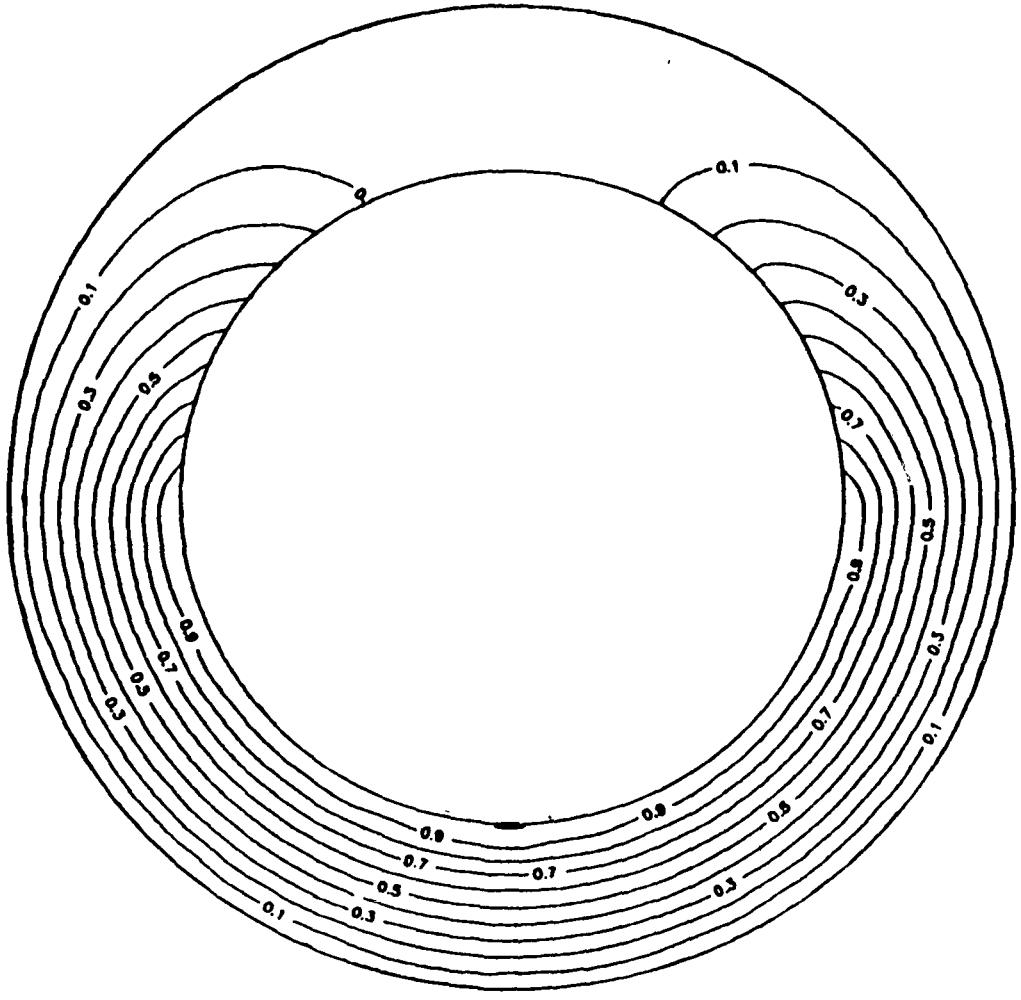


Figure A1a. Isotherms for $T_I(\psi) = 1 + \cos\psi$ imposed on the upper half cyliner

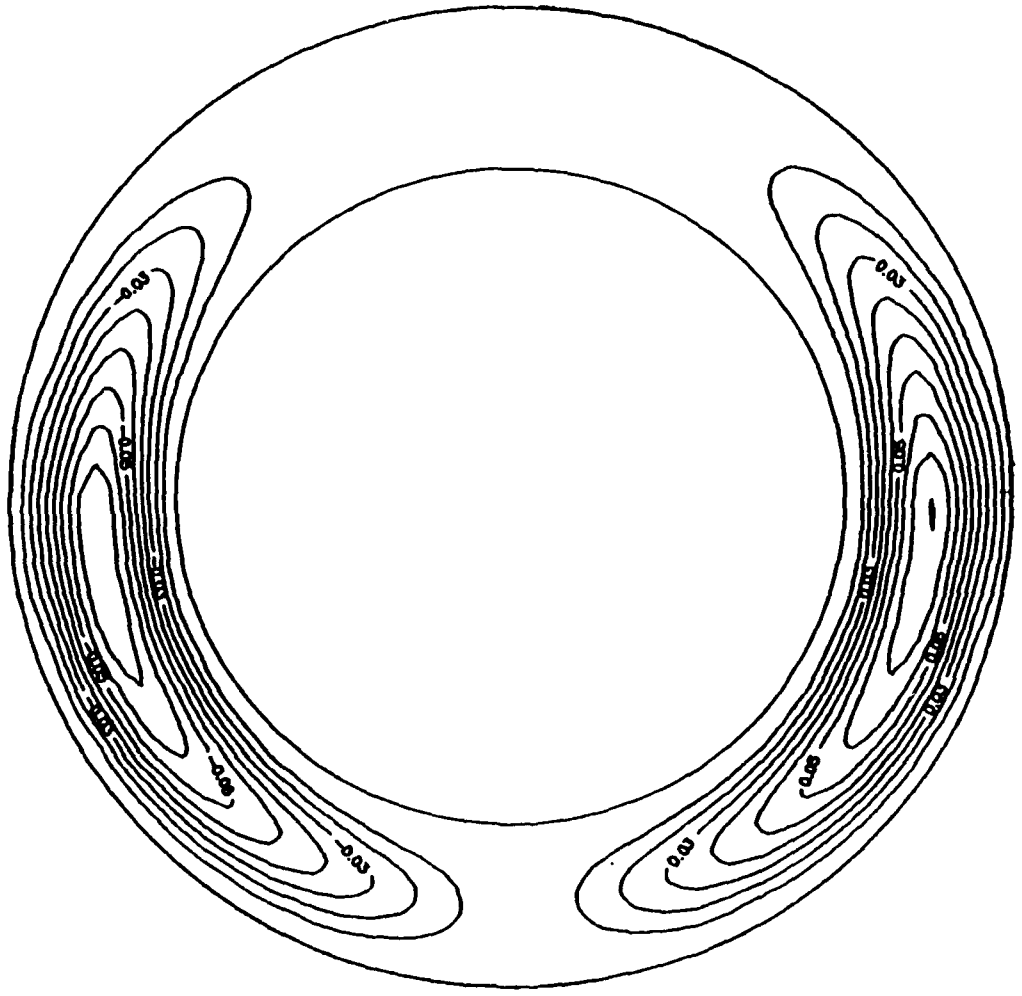
-0.03
-0.06
-0.09
-0.12
-0.15
-0.18
-0.21
-0.24
-0.27
-0.30
-0.33
-0.36
-0.39
-0.42
-0.45
-0.48
-0.51
-0.54
-0.57
-0.60
-0.63
-0.66
-0.69
-0.72
-0.75
-0.78
-0.81
-0.84
-0.87
-0.90
-0.93
-0.96
-0.99
-1.02
-1.05
-1.08
-1.11
-1.14
-1.17
-1.20
-1.23

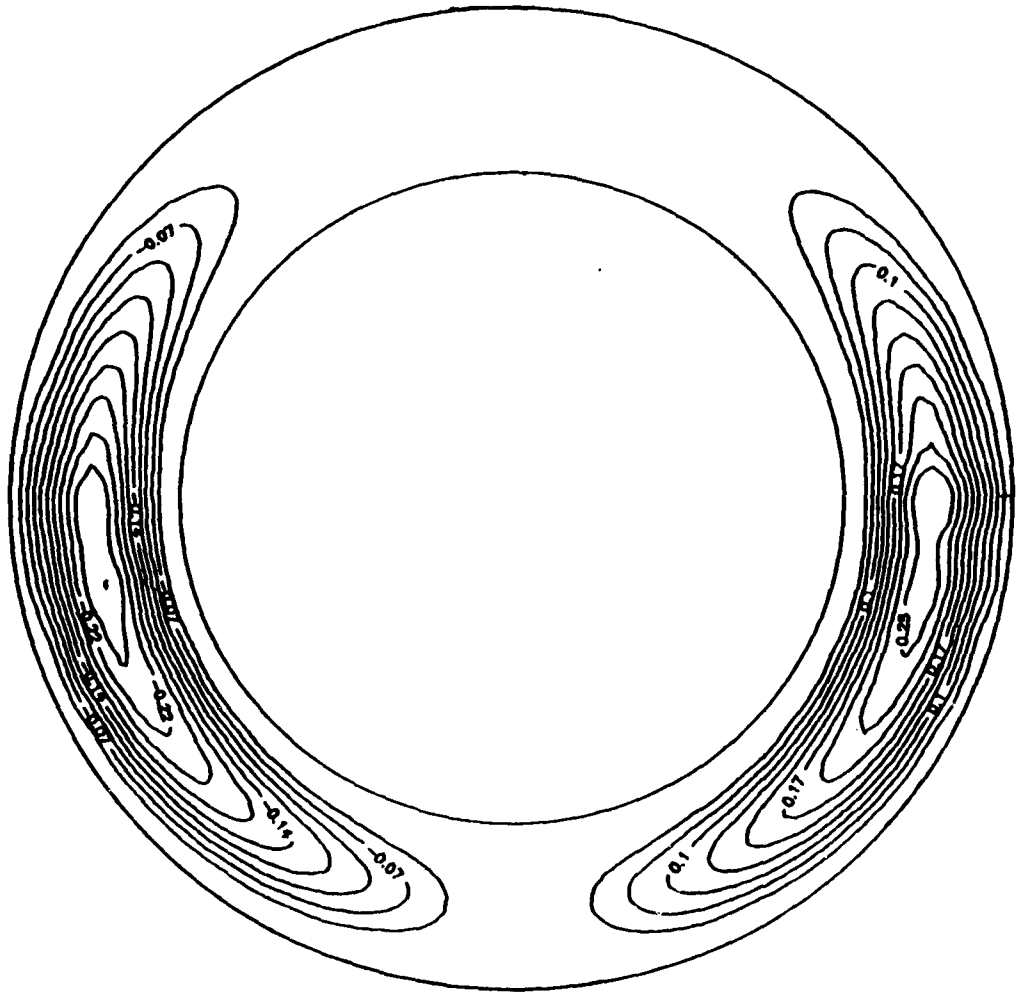


Figure A1c. Numerical streamlines for $\hat{G} = 4.71$, $T_I(\psi) = 1 + \cos\psi$ imposed on the upper half cylinder

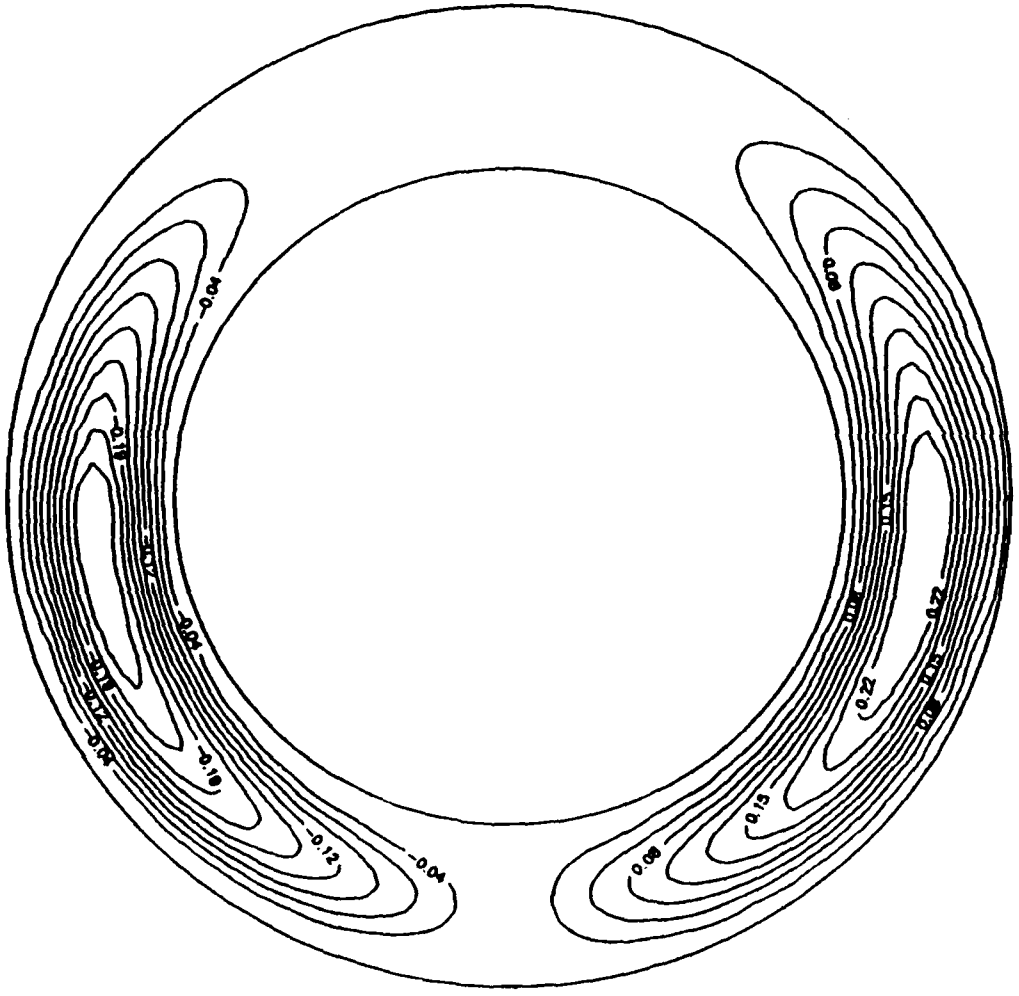


Figure A1d. Analytical streamlines for $\hat{G} = 4.71$, $T_I(\psi) = 1 + \cos\psi$ imposed on the upper half-cylinder

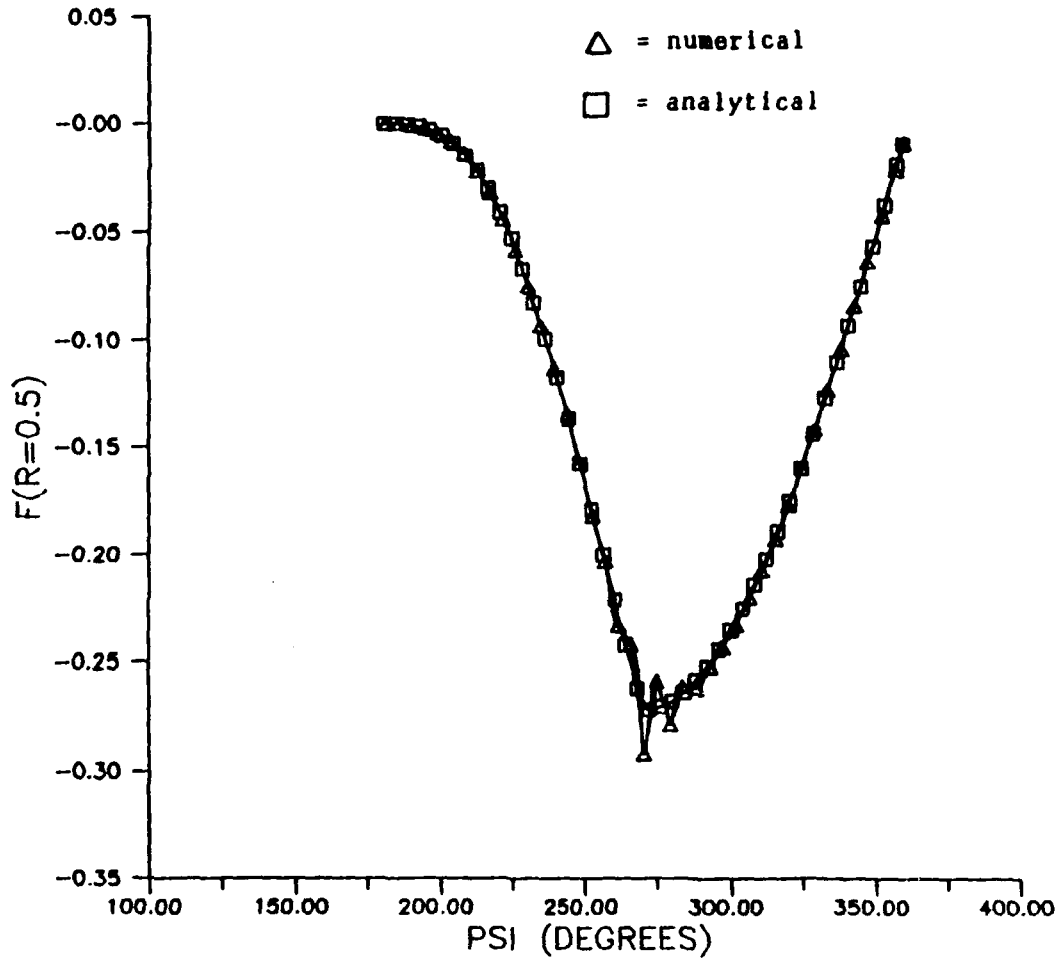


Figure A1e. Angular variation of the center-line stream function at $\hat{G} = 4.71$ for $T_I(\psi) = 1 + \cos\psi$ imposed on the upper half-cylinder

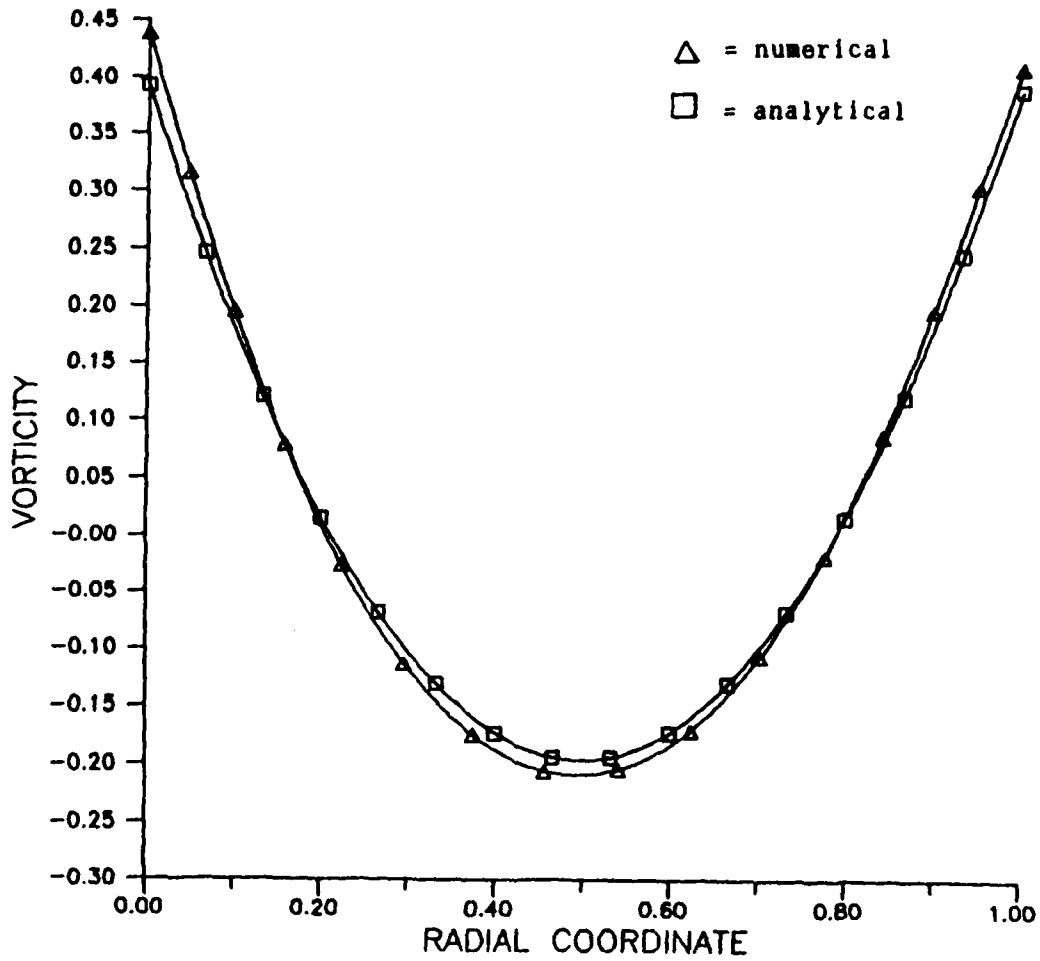


Figure A1f. Radial variation of vorticity at 88° for $\hat{G}$ =4.71 for $T_I(\psi) = 1 + \cos\psi$ imposed on the upper half-cylinder

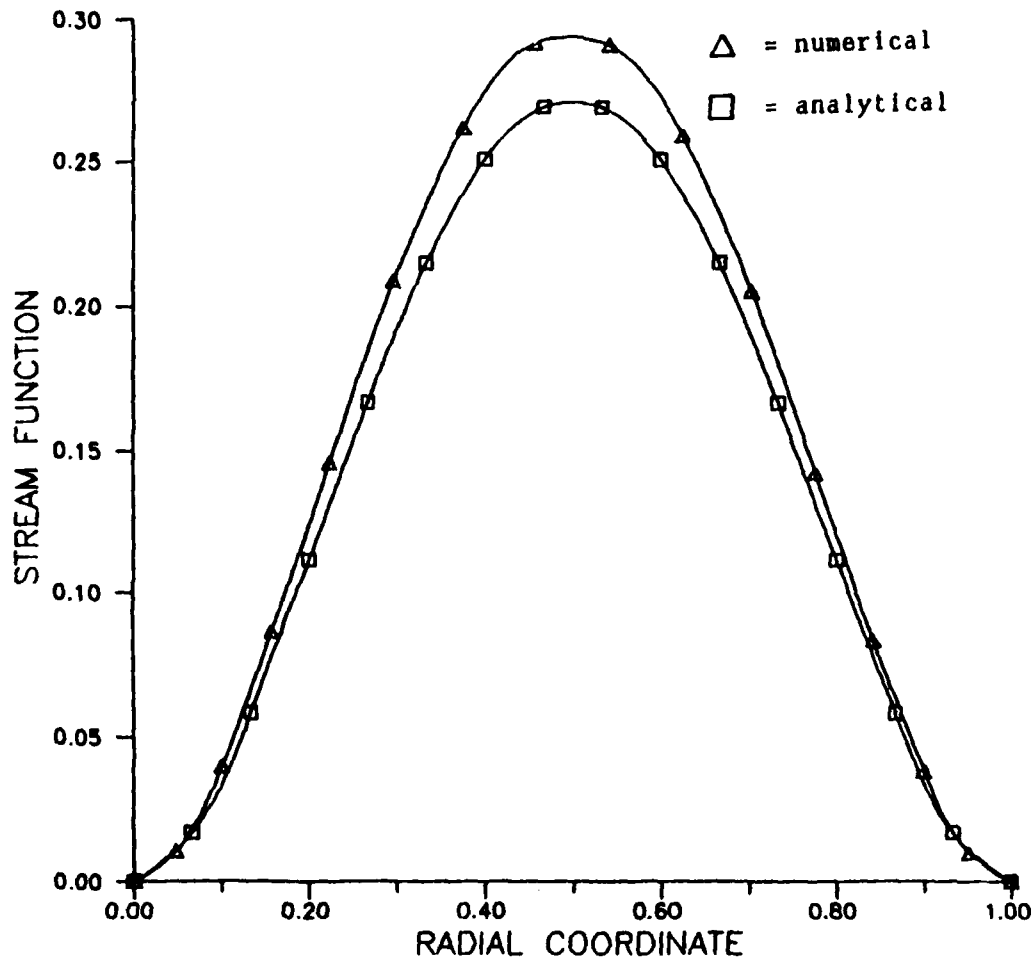


Figure A1g. Radial variation of the stream function at 88° for $\hat{G} = 4.71$ for $T_I(\psi) = 1 + \cos\psi$ imposed on the upper half-cylinder

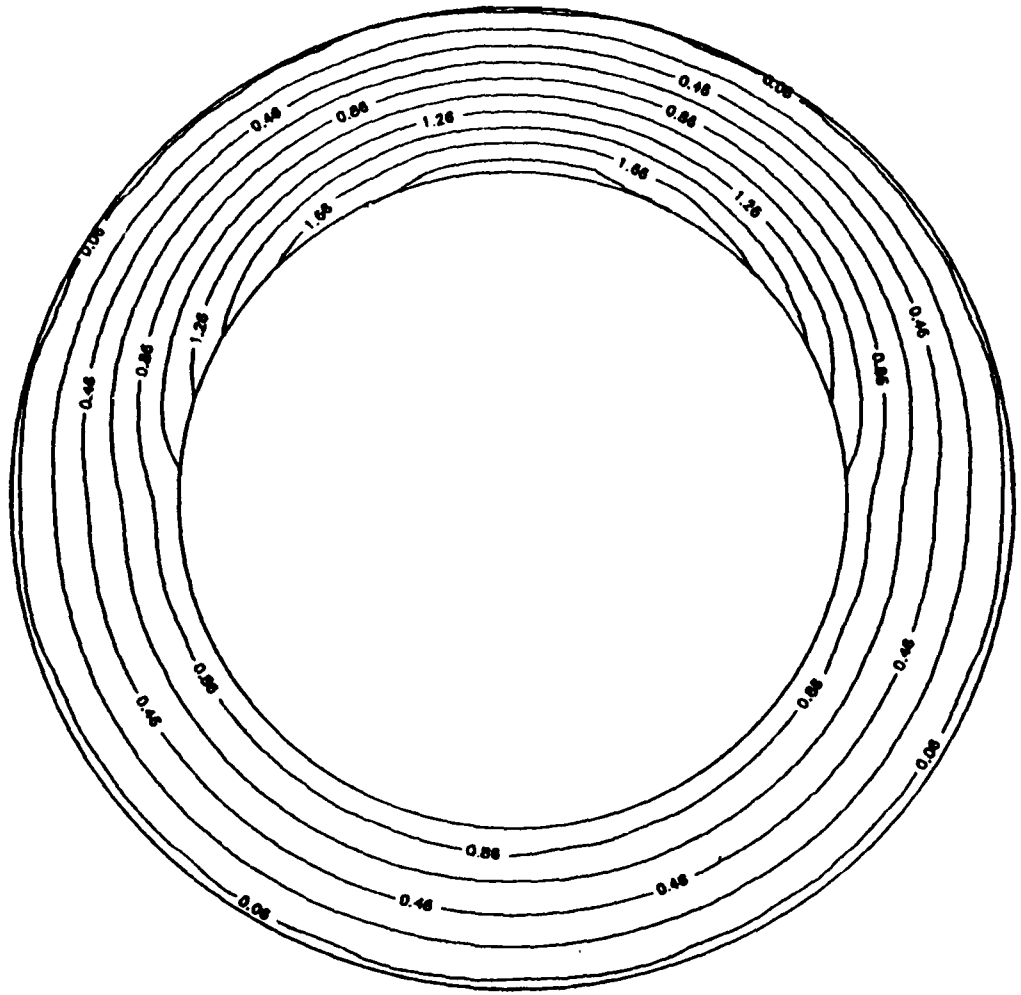


Figure A2a. Isotherms for $T_I(\psi) = 1 - \cos\psi$ imposed on the upper half-cylinder

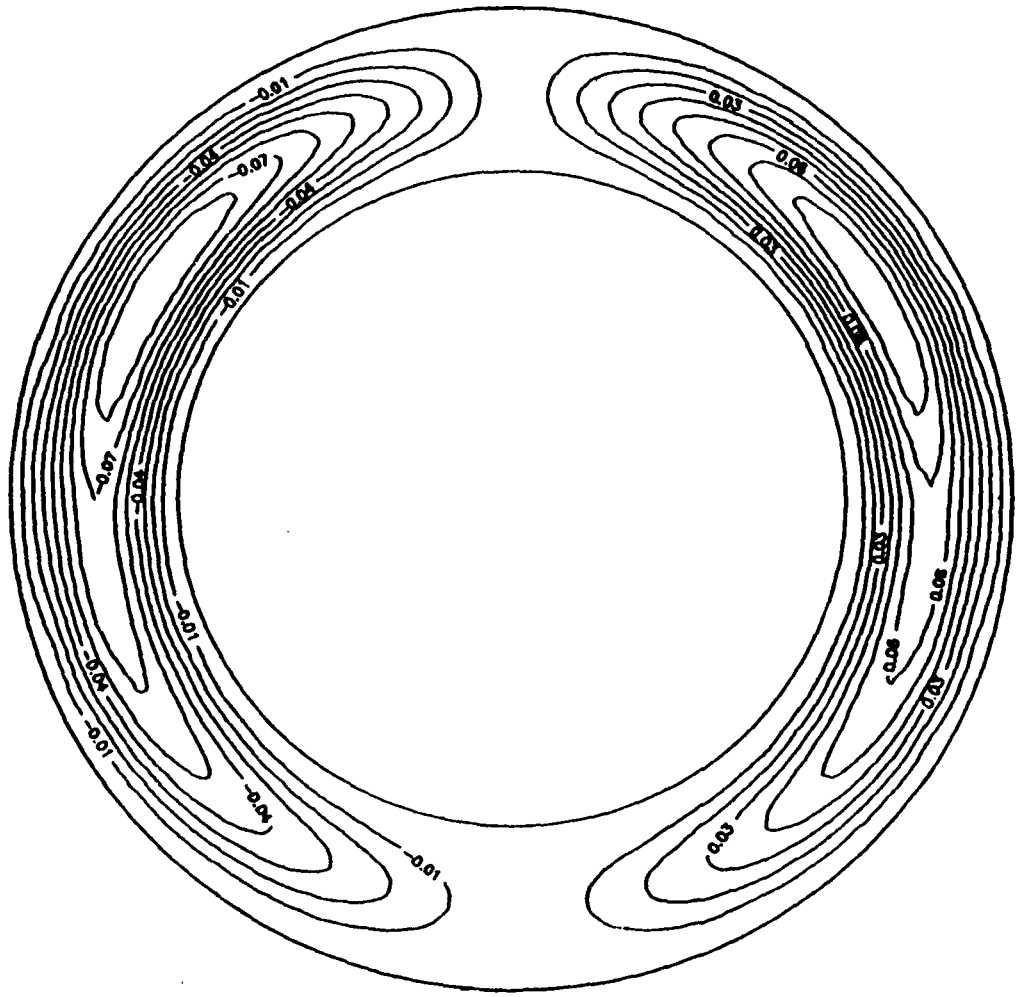


Figure A2b. Numerical streamlines at $\hat{G} = 3.0$ for $T_I(\psi) = 1 - \cos\psi$ imposed on the upper half-cylinder

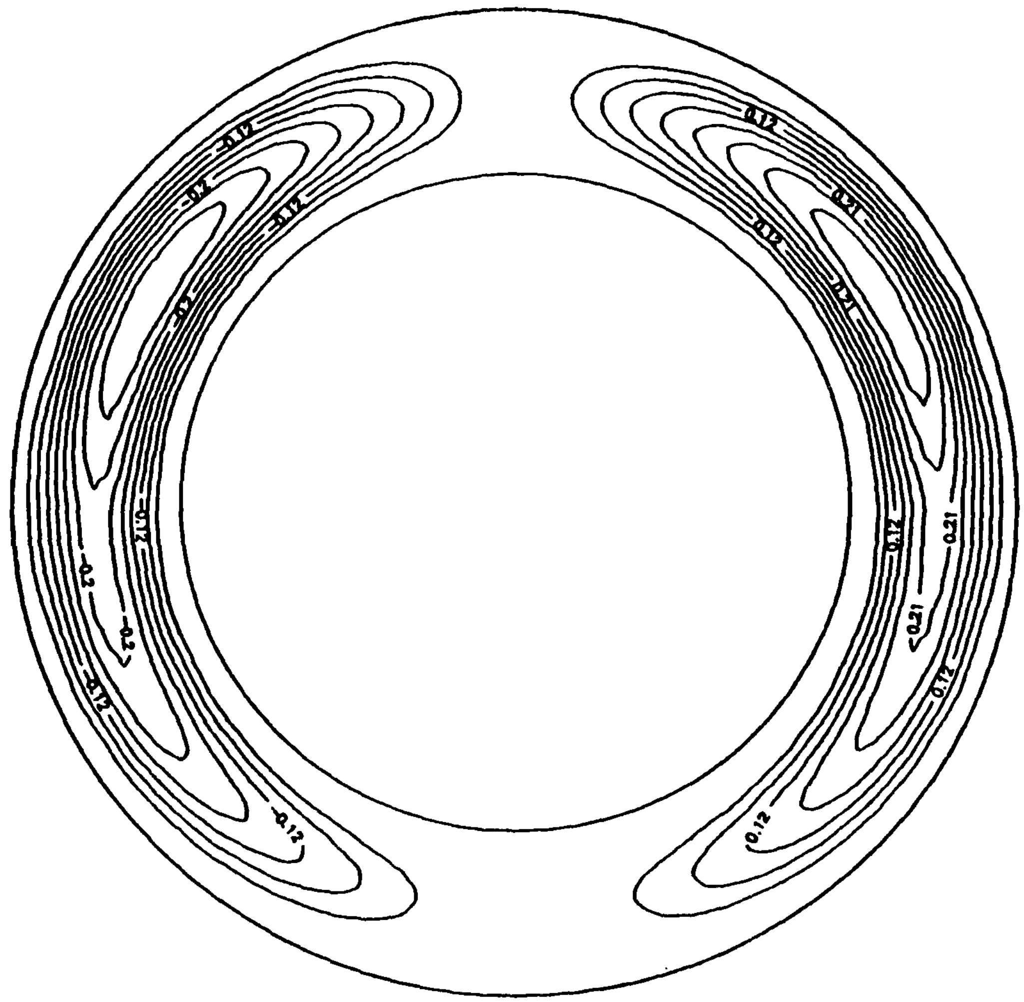


Figure A2c. Numerical streamlines at $\hat{C} = 4.40$ for $T(\psi) = 1 - \cos\psi$ imposed on the upper half-cylinder

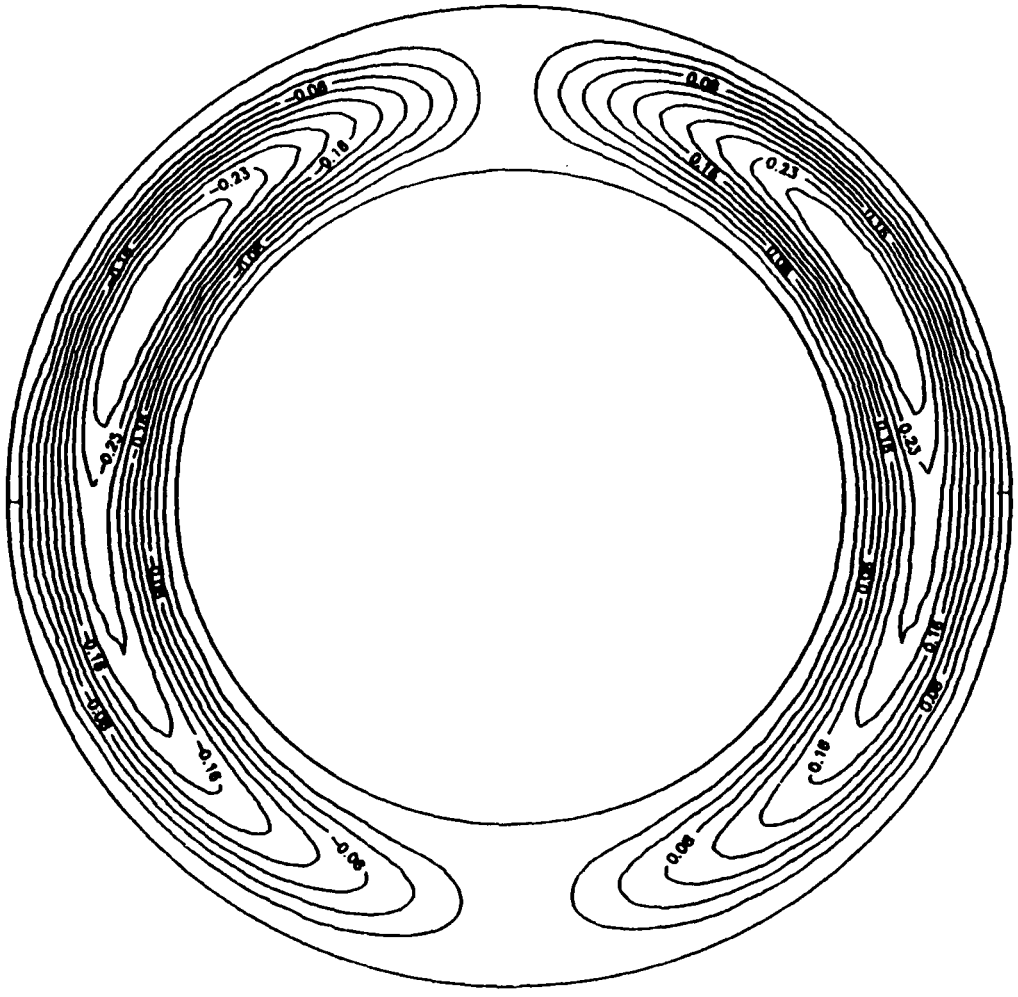


Figure A2d. Analytical streamlines at $\hat{G}$ = 4.40 for $T_I(\psi) = 1 - \cos\psi$ imposed on the upper half-cylinder

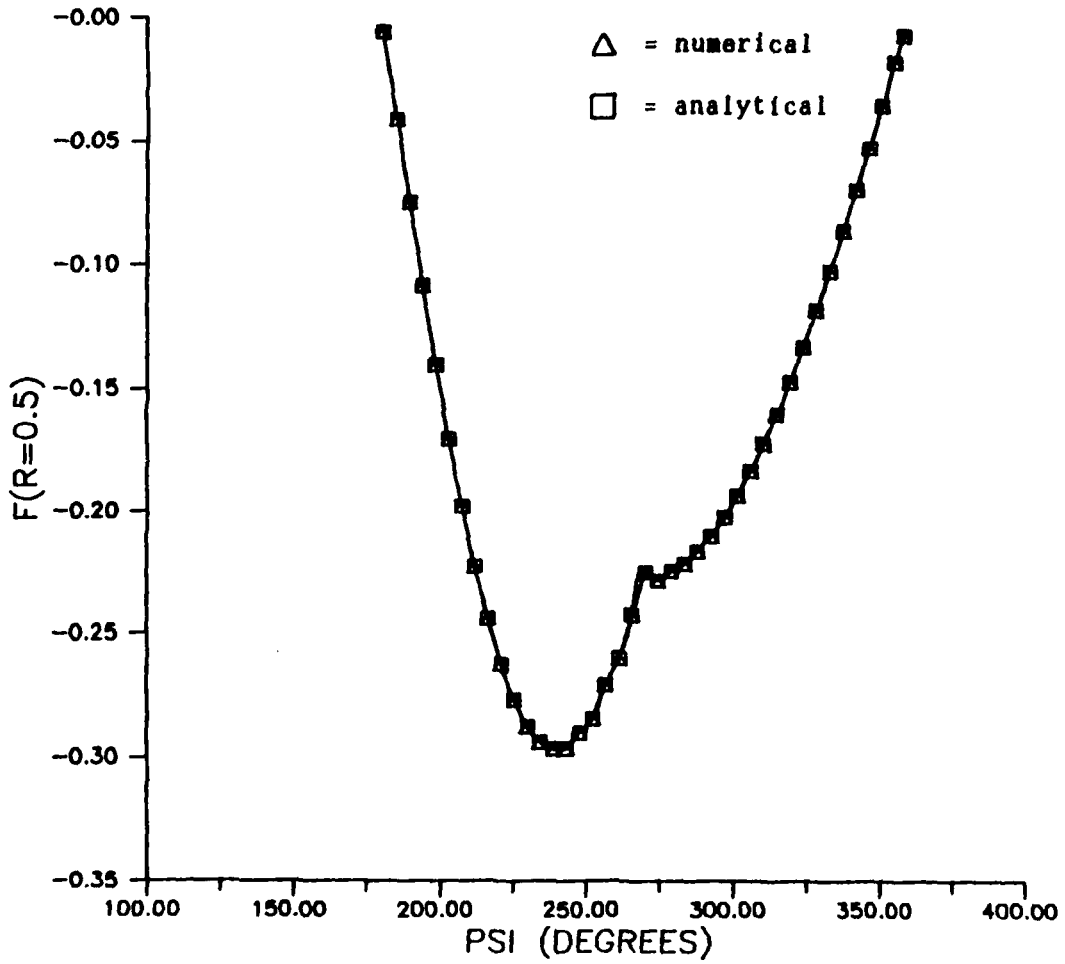


Figure A2e. Angular variation of the center-line stream function at $\hat{G} = 4.40$ for $T_I(\psi) = 1 - \cos\psi$ imposed on the upper half-cylinder

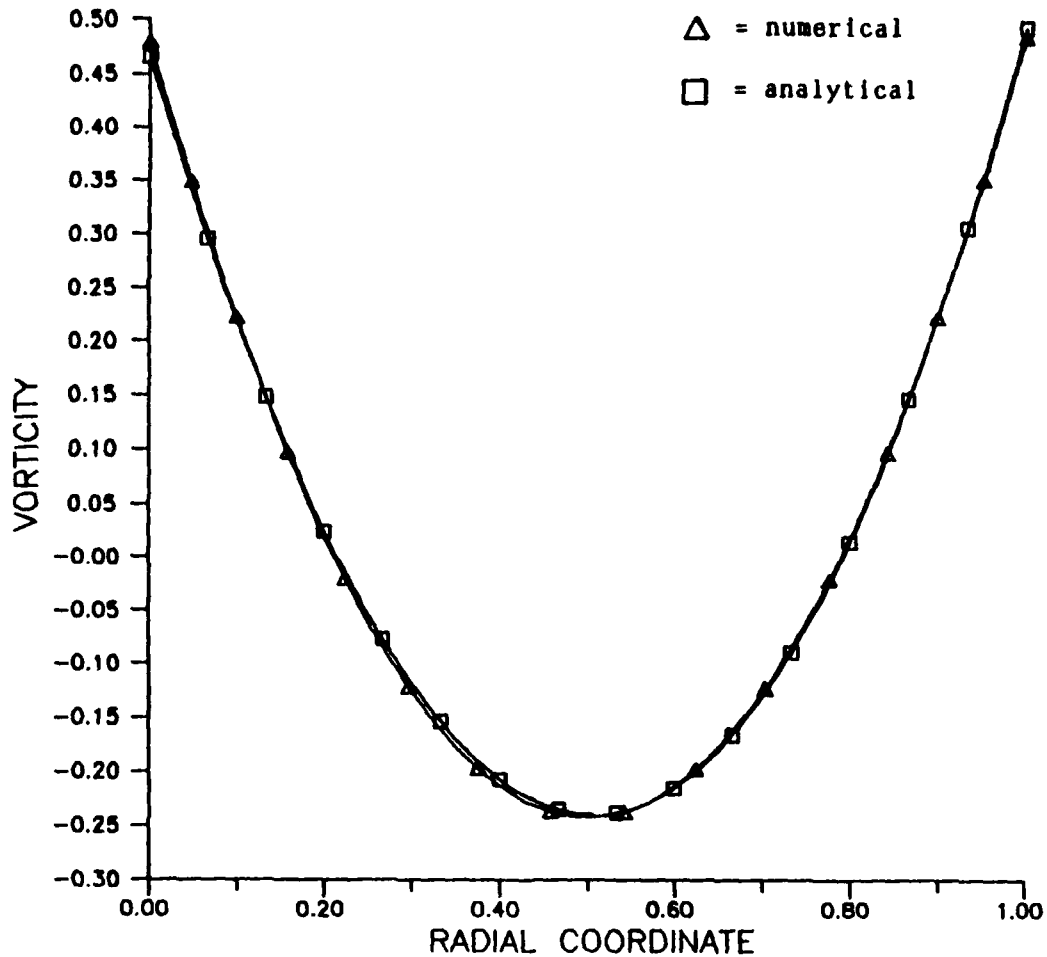


Figure A2f. Radial variation of vorticity at 120° for $\hat{G}$ = 4.40 for $T_I(\psi) = 1 - \cos\psi$ imposed on the upper half-cylinder

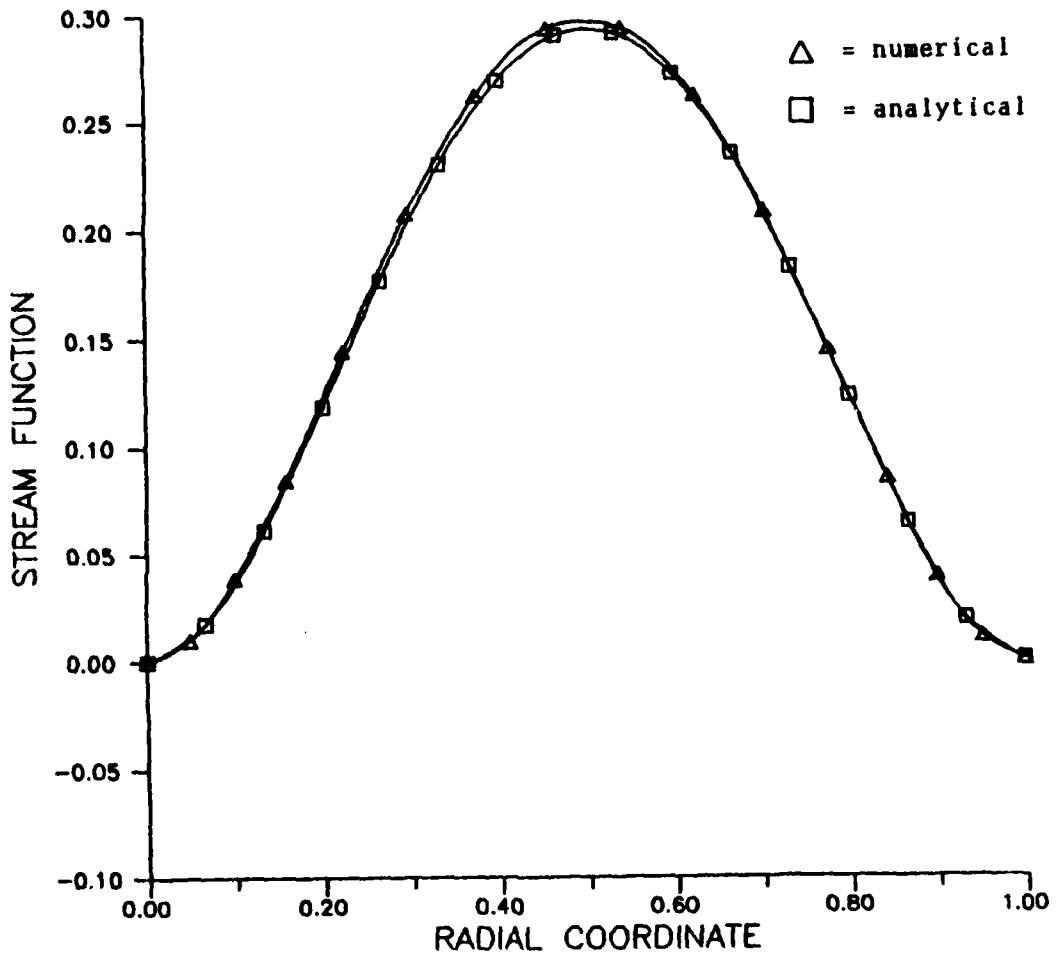


Figure A2g. Radial variation of the stream function at 120 °for $\hat{G}$ = 4.40 for $T_I(\psi)$ = 1-cos $\psi$ imposed on the upper half-cylinder

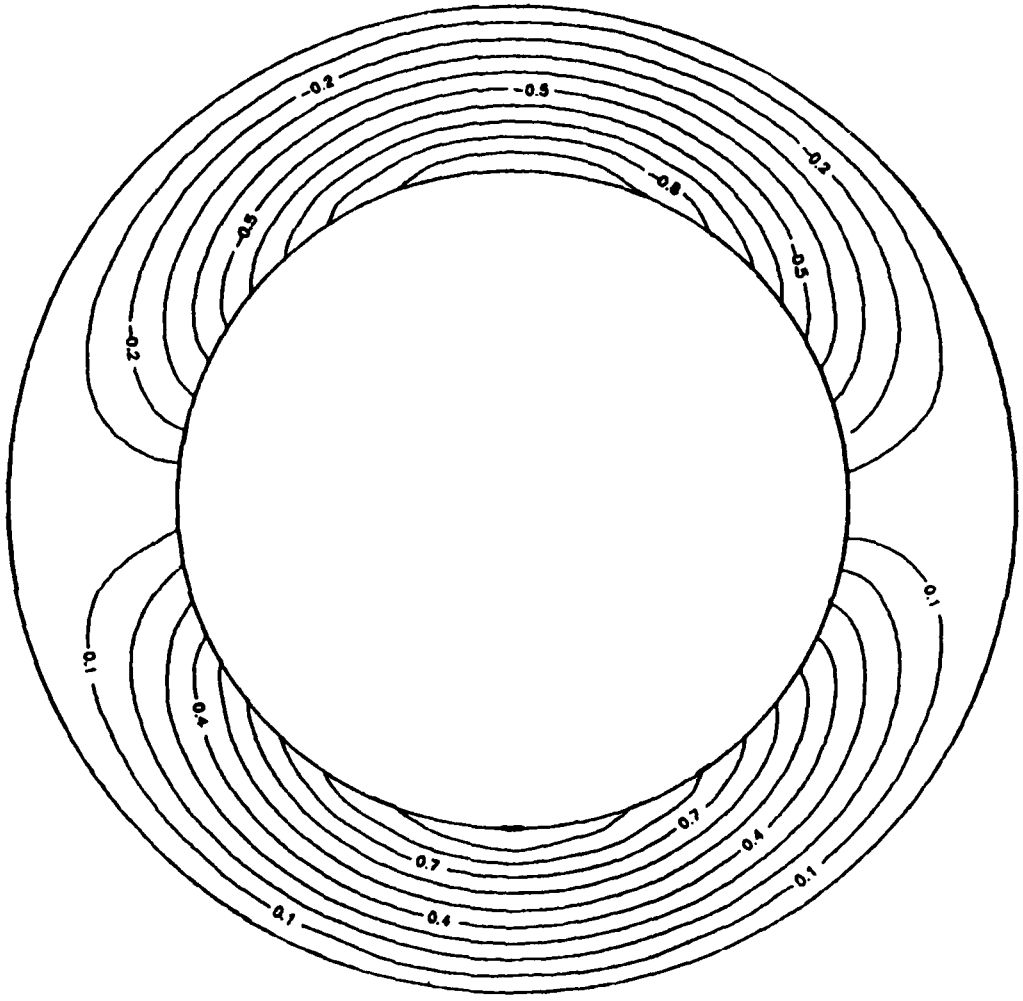


Figure A3a. Isotherms for $T_I(\psi) = \cos \psi$

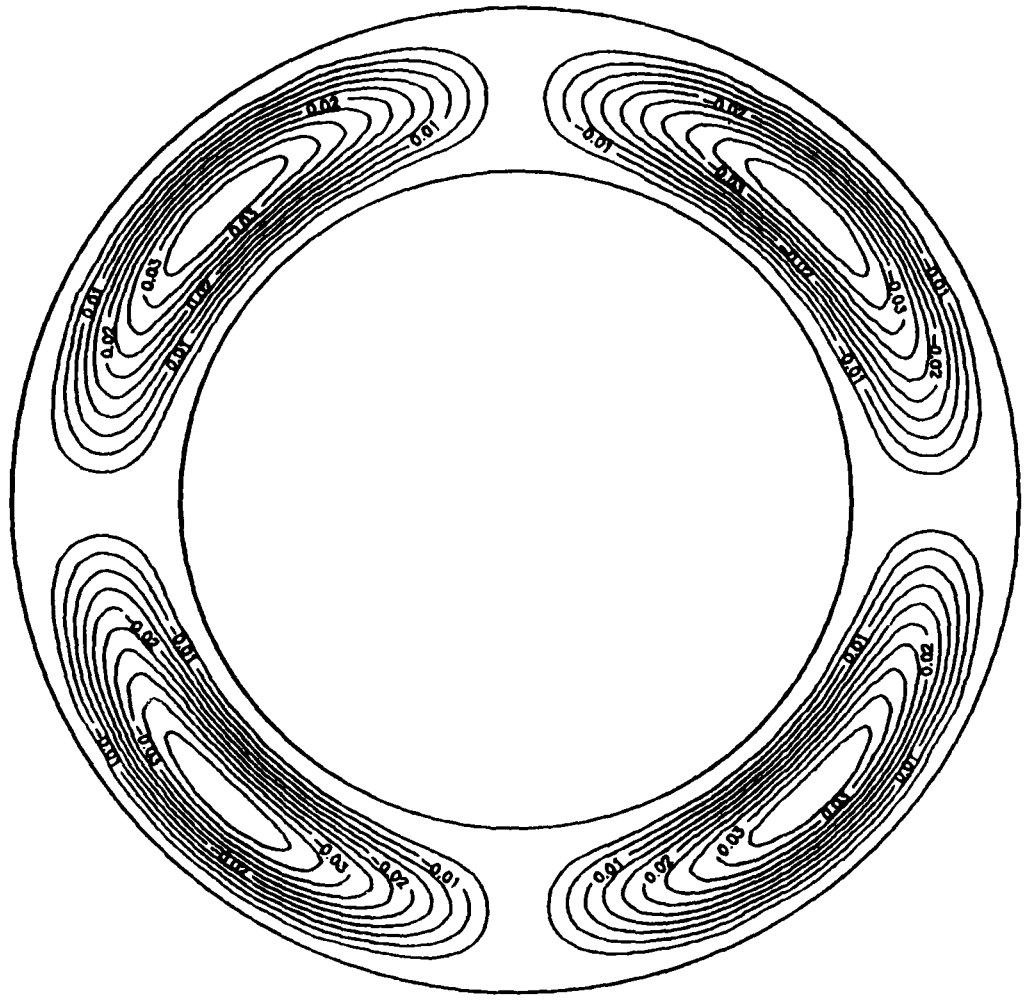


Figure A3b. Numerical streamlines for $T_I(\psi) = \cos\psi$ at $\hat{G} = 3.0$

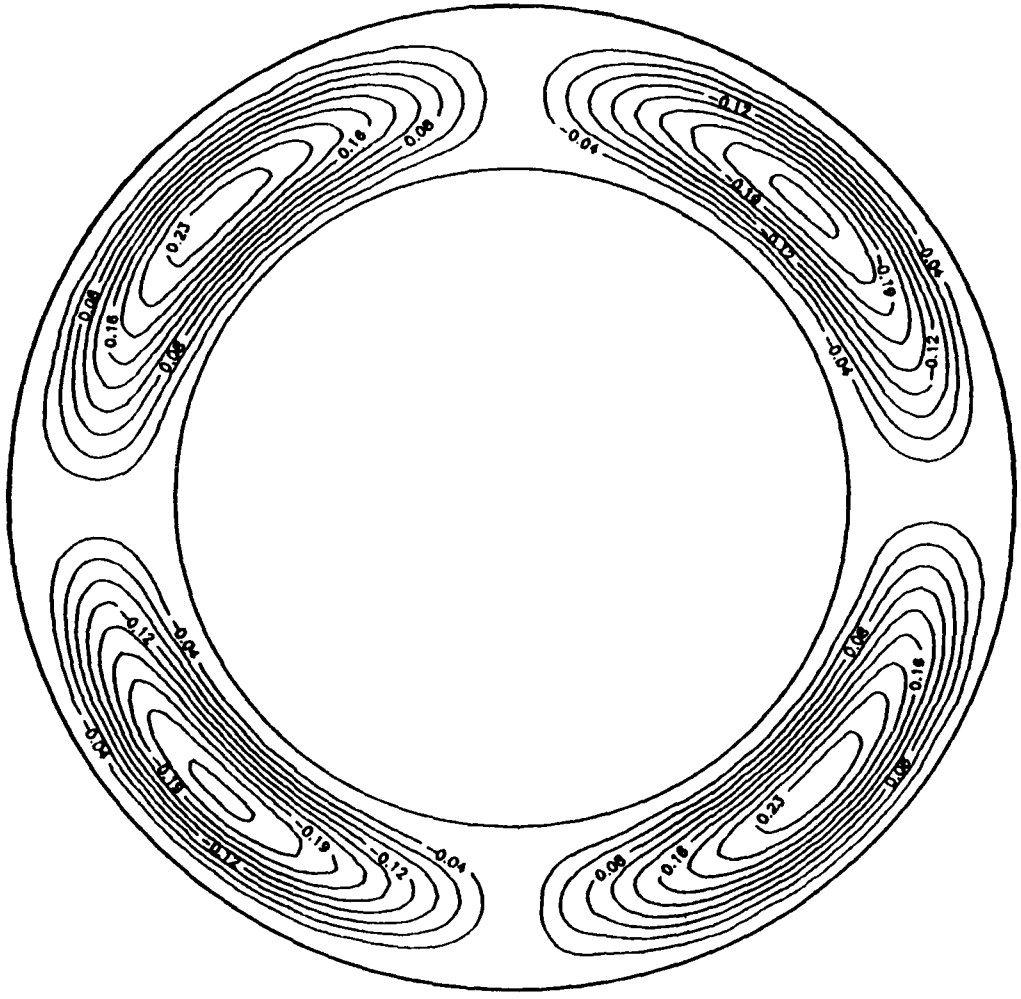


Figure A3c. Numerical streamlines for $T_I(\psi) = \cos\psi$ at $\hat{G} = 5.75$

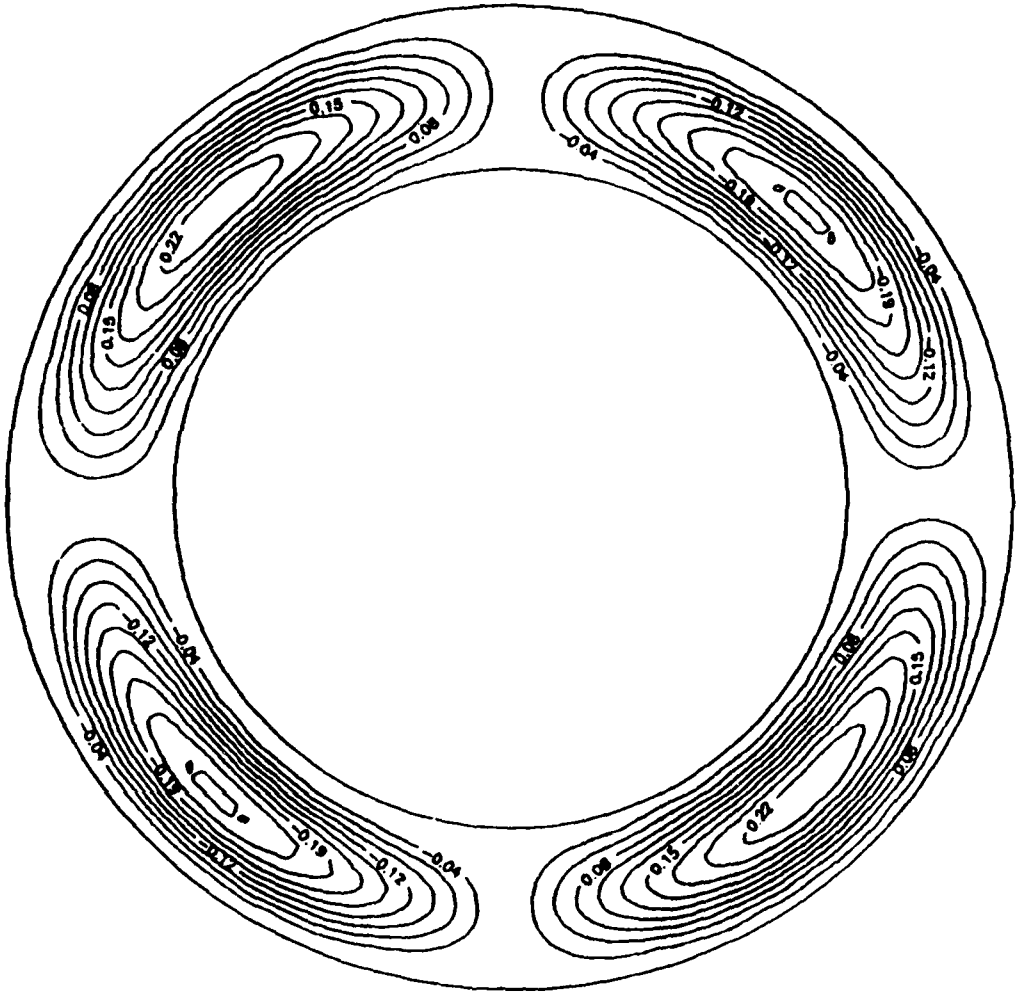


Figure A3d. Analytical streamlines for $T_I(\psi) = \cos\psi$ at $\hat{G} = 5.75$

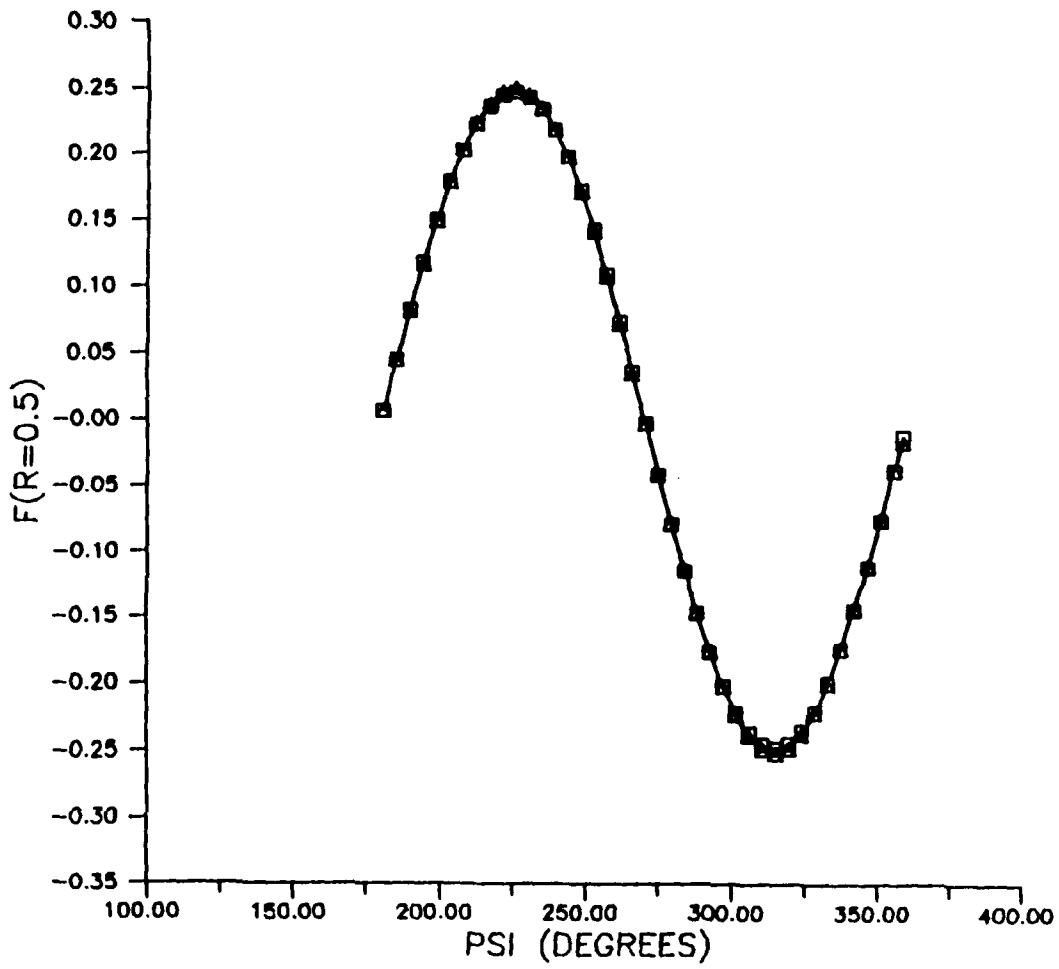


Figure A3e. Angular variation of the center-line stream function for $\hat{G}$ = 5.75

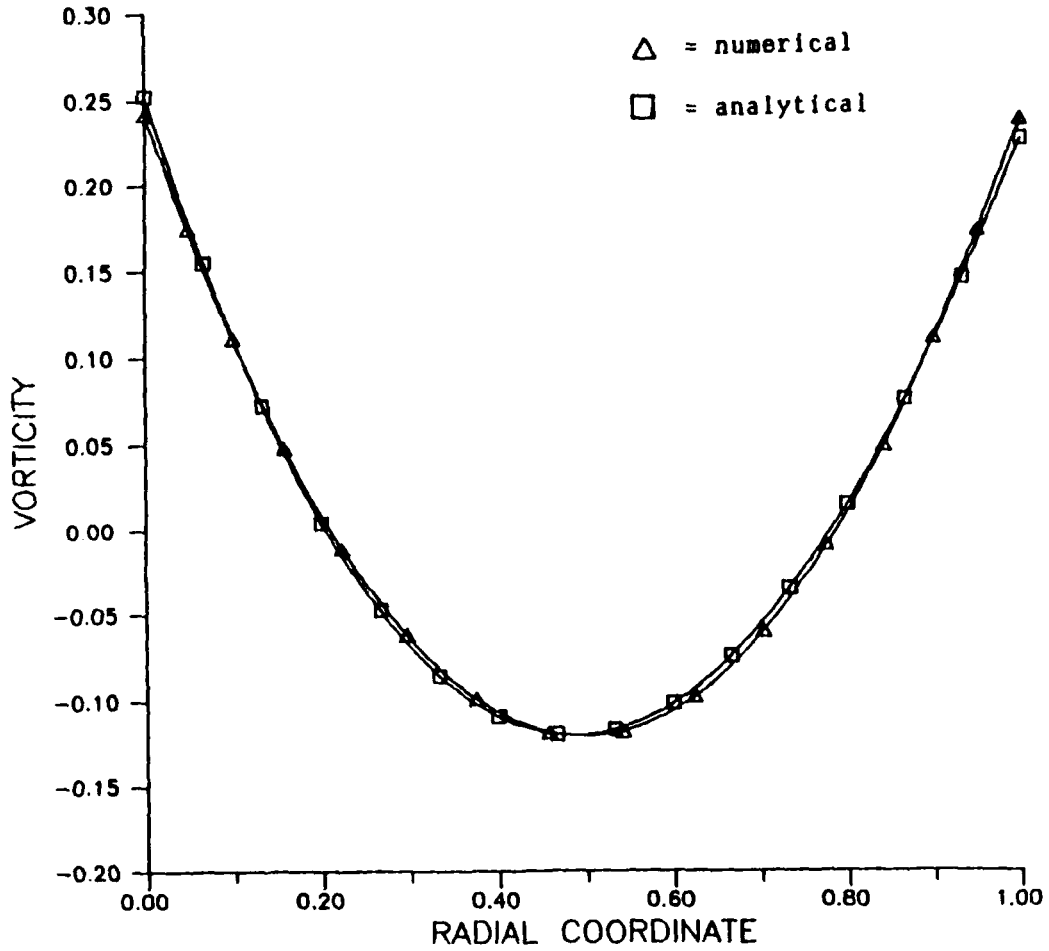


Figure A3f. Radial variation of vorticity at 45° for $\hat{G} = 5.75$
$T_I(\psi) = \cos(\psi)$

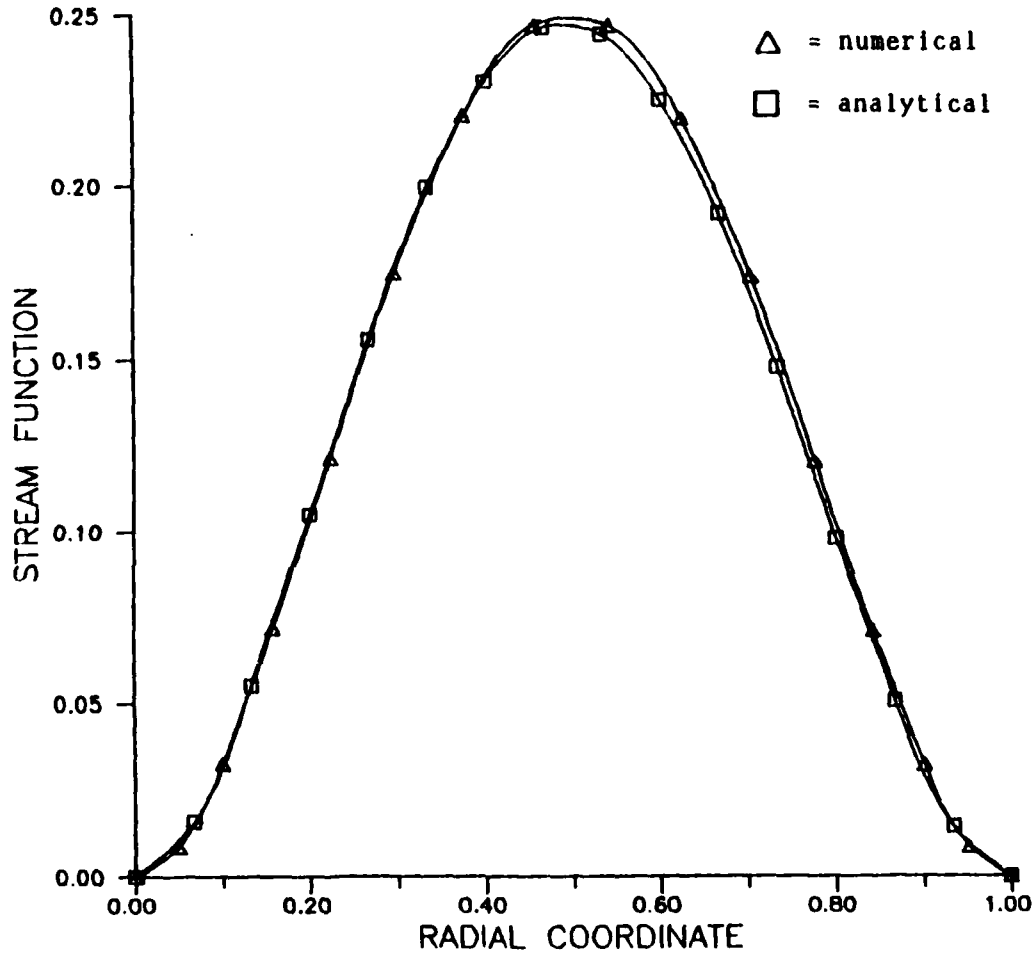


Figure A3g. Radial variation of the stream function at 45° for $\hat{G} = 5.75$
$T_I(\psi) = \cos \psi$

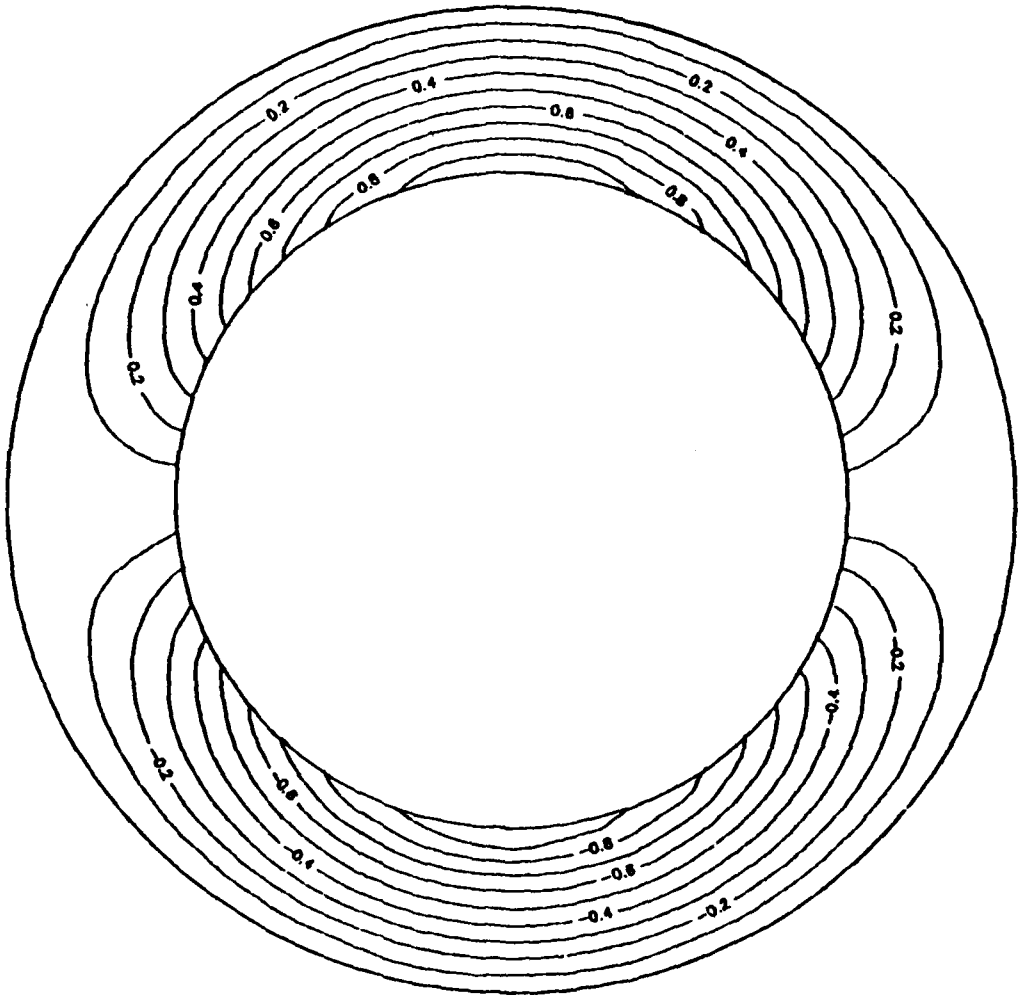


Figure A4a. Isotherms for $T_I(\psi) = -\cos(\psi)$

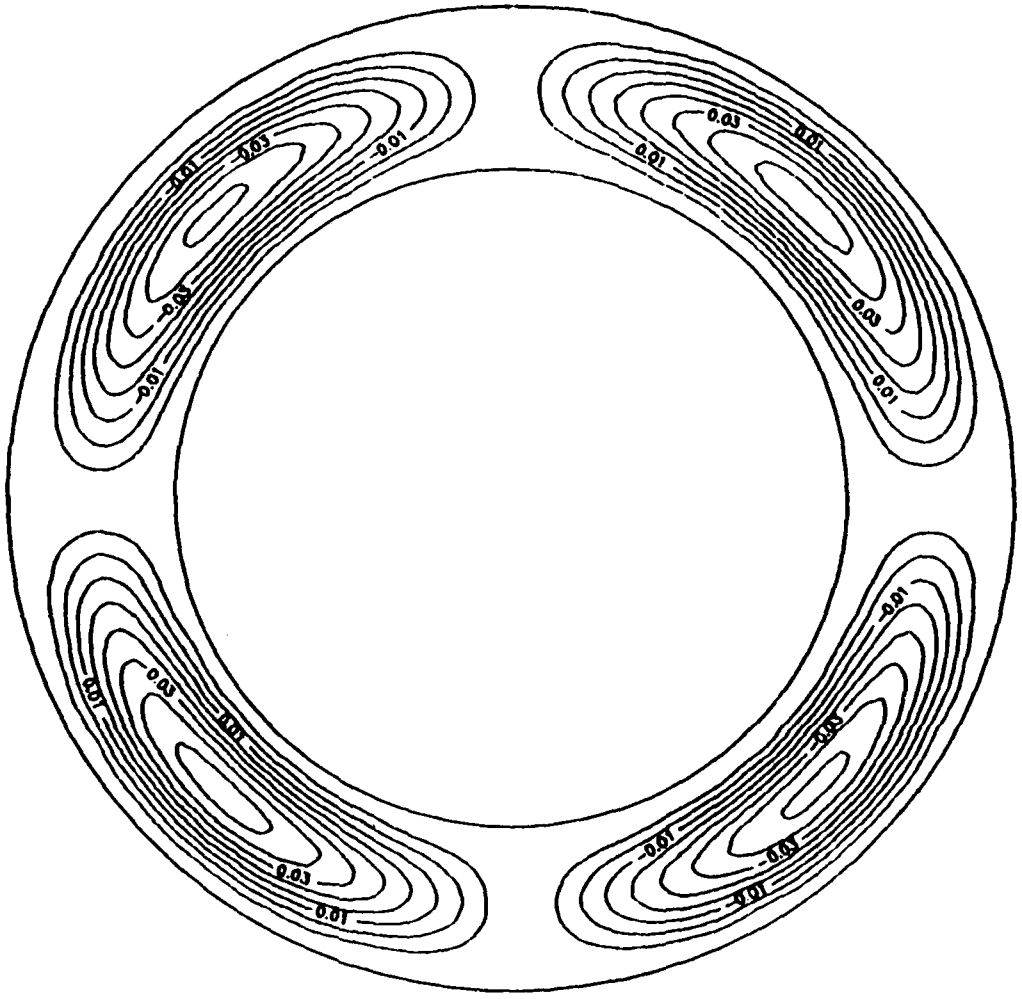


Figure A4b. Numerical streamlines for $T_I(\psi) = -\cos(\psi)$ at $\hat{G} = 3.0$

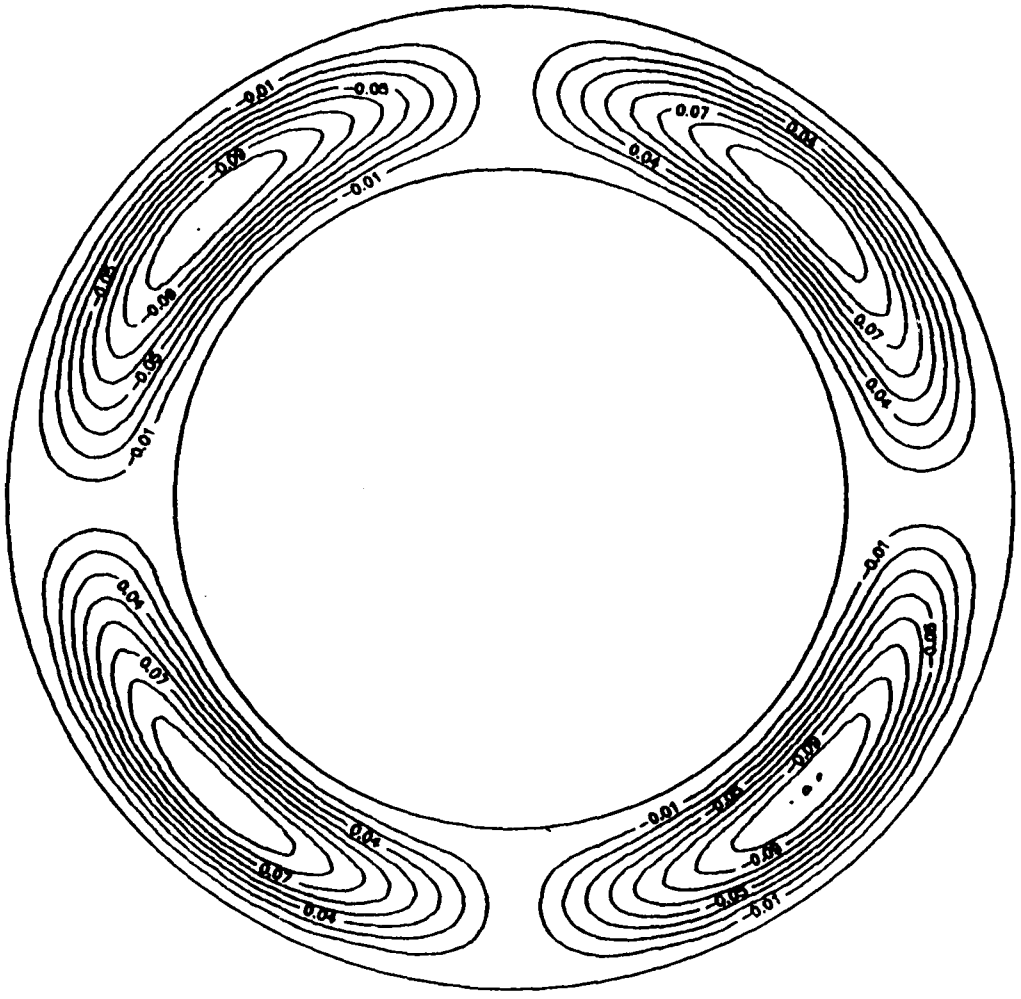


Figure A4c. Numerical streamlines for $T_I(\psi) = -\cos(\psi)$ at $\hat{G} = 4.40$

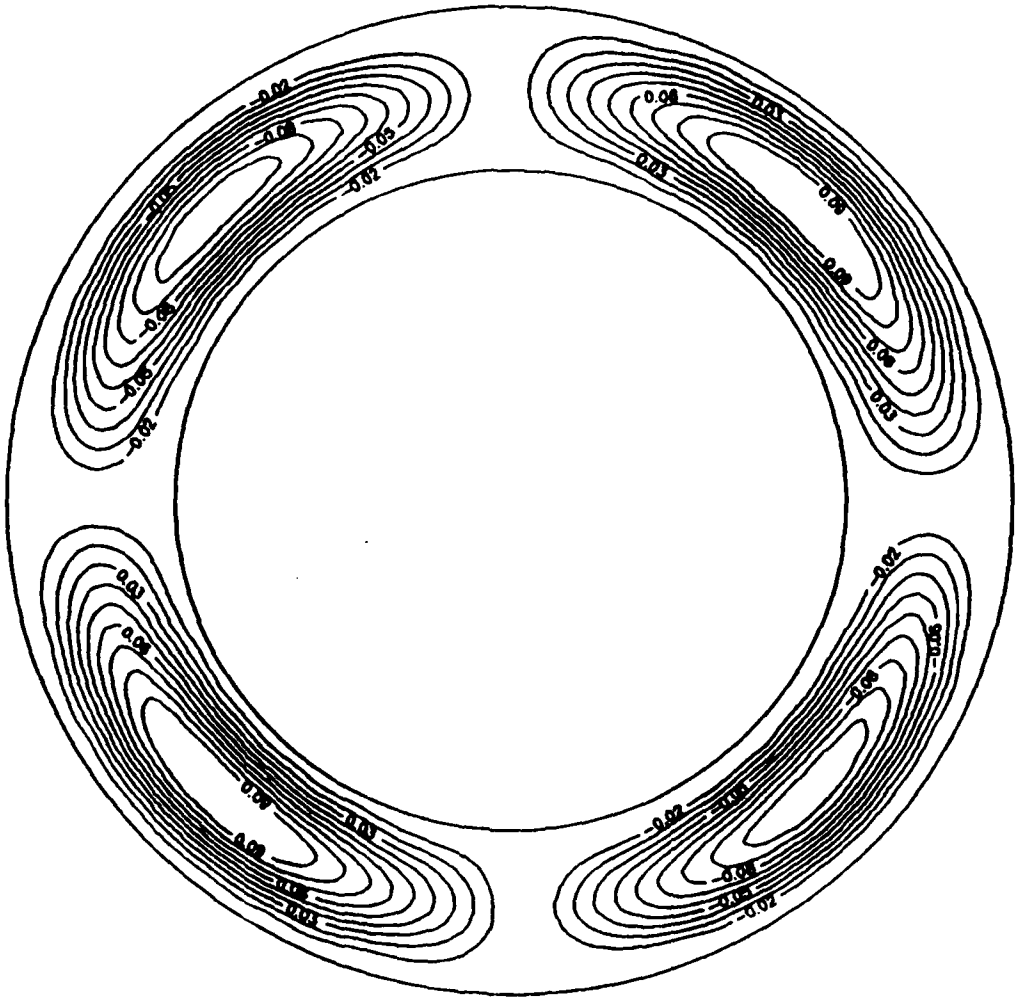

Figure A4d. Analytical streamlines for $T_I(\psi) = -\cos(\psi)$ at $\hat{G} = 4.40$

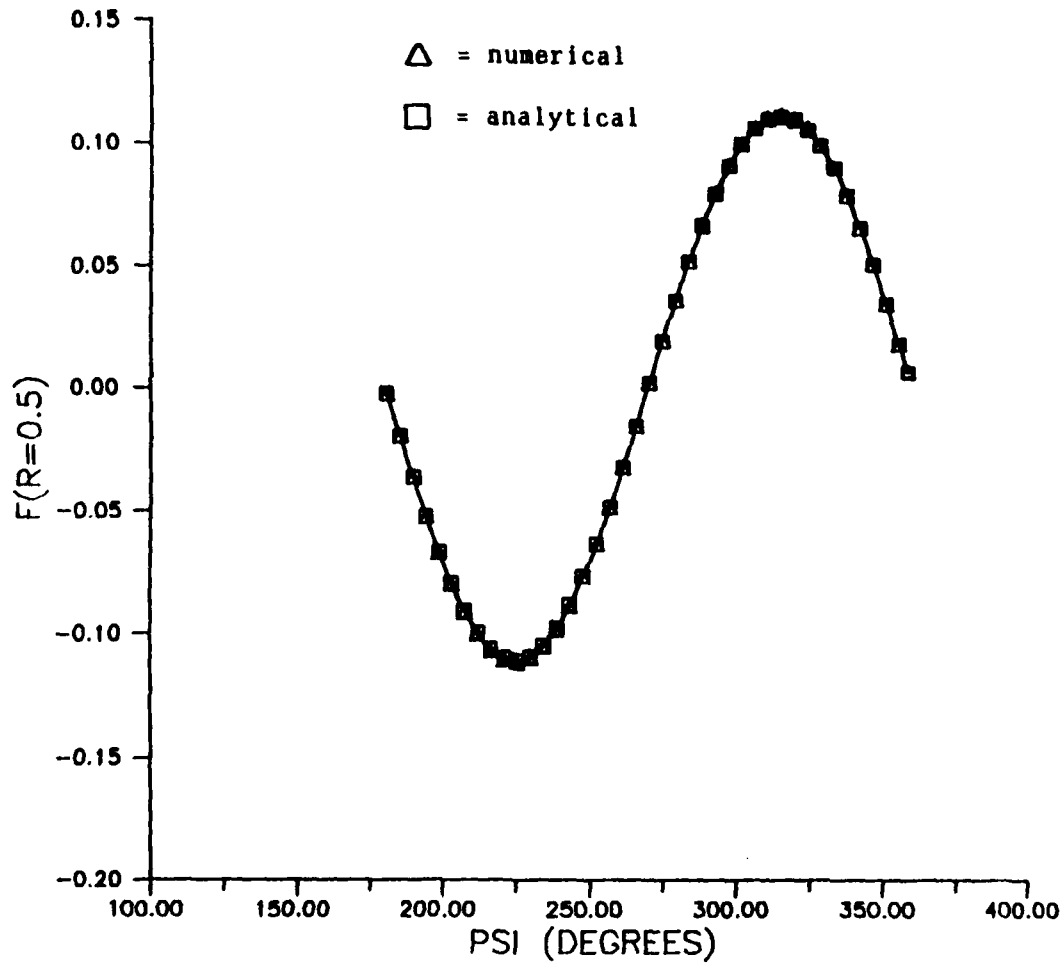


Figure A4e. Angular variation of the center-line stream function at $\hat{C} = 4.40$
$T_I(\psi) = -\cos(\psi)$

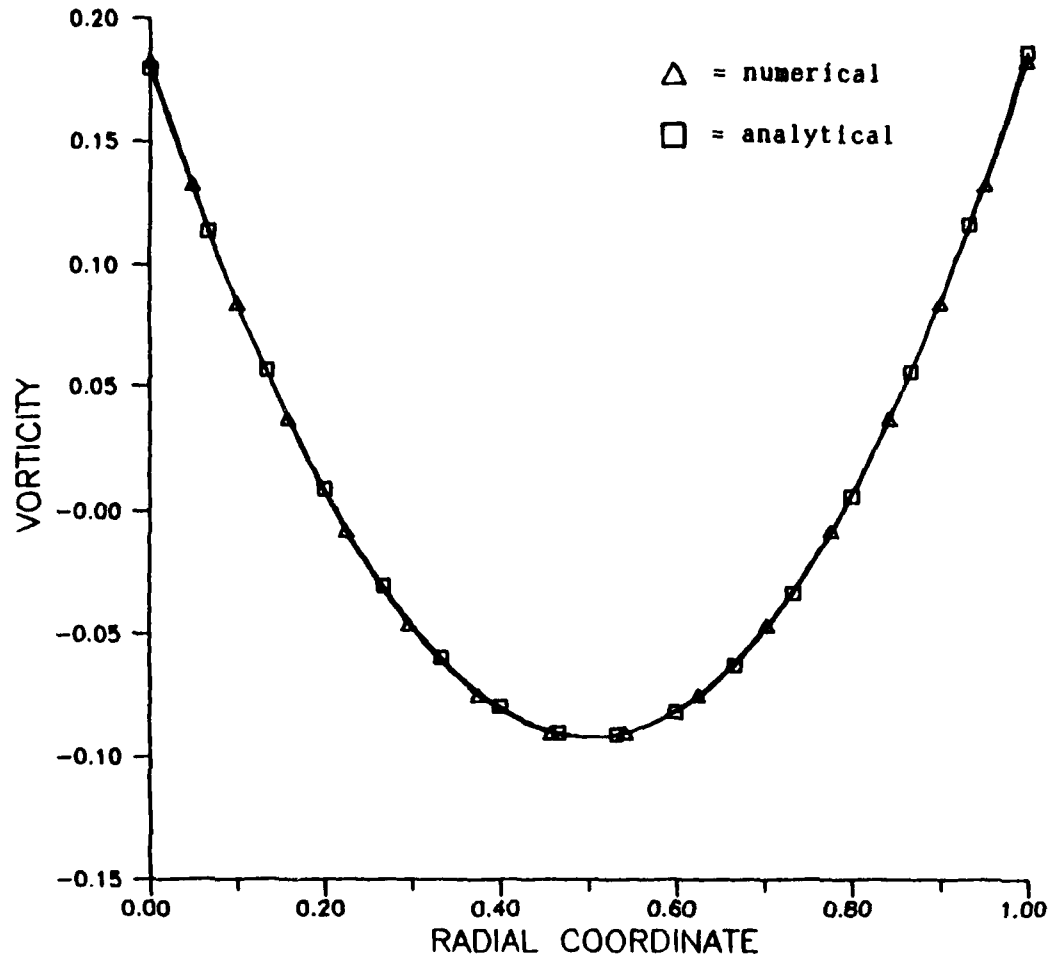


Figure A4f. Radial variation of vorticity at 315° for $\hat{G} = 4.40$
$T_I(\psi) = -\cos(\psi)$

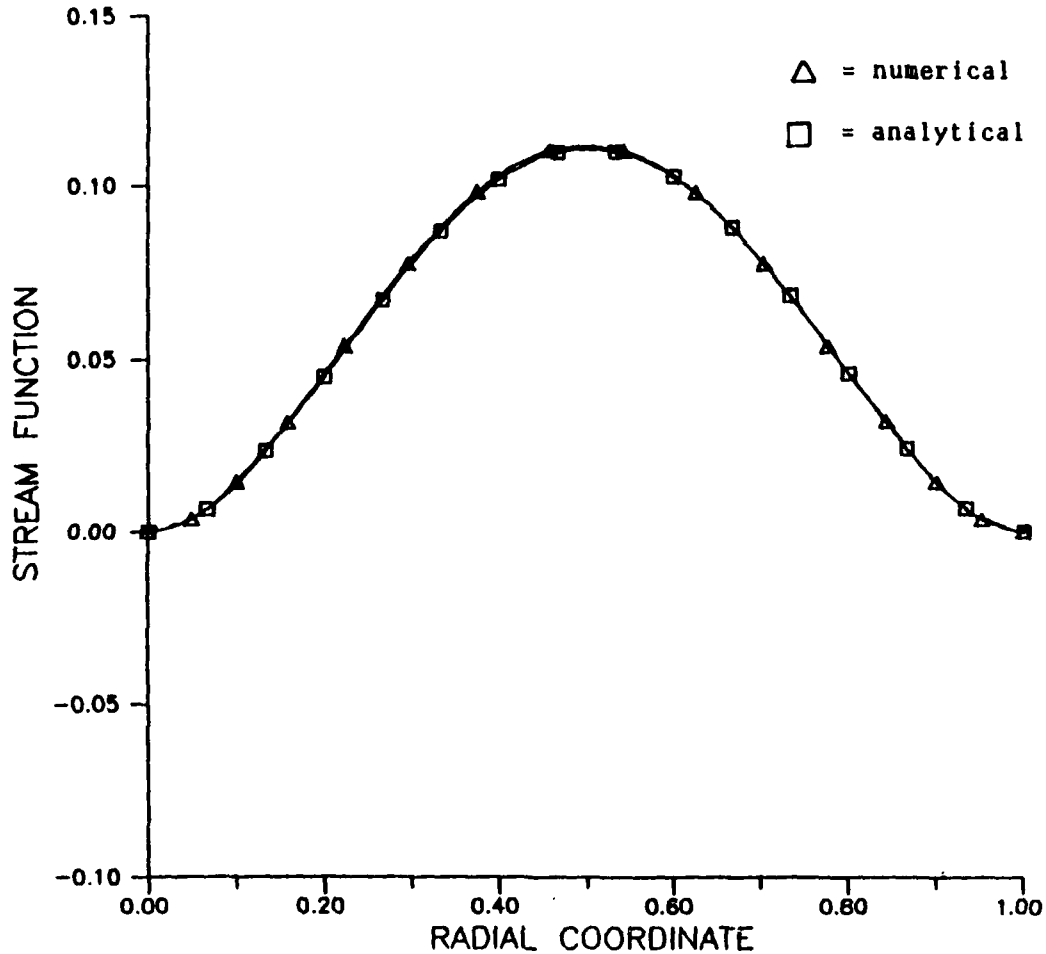


Figure A4g. Radial variation of the stream function at 315° for $\hat{G} = 4.40$
$T_I(\psi) = -\cos(\psi)$

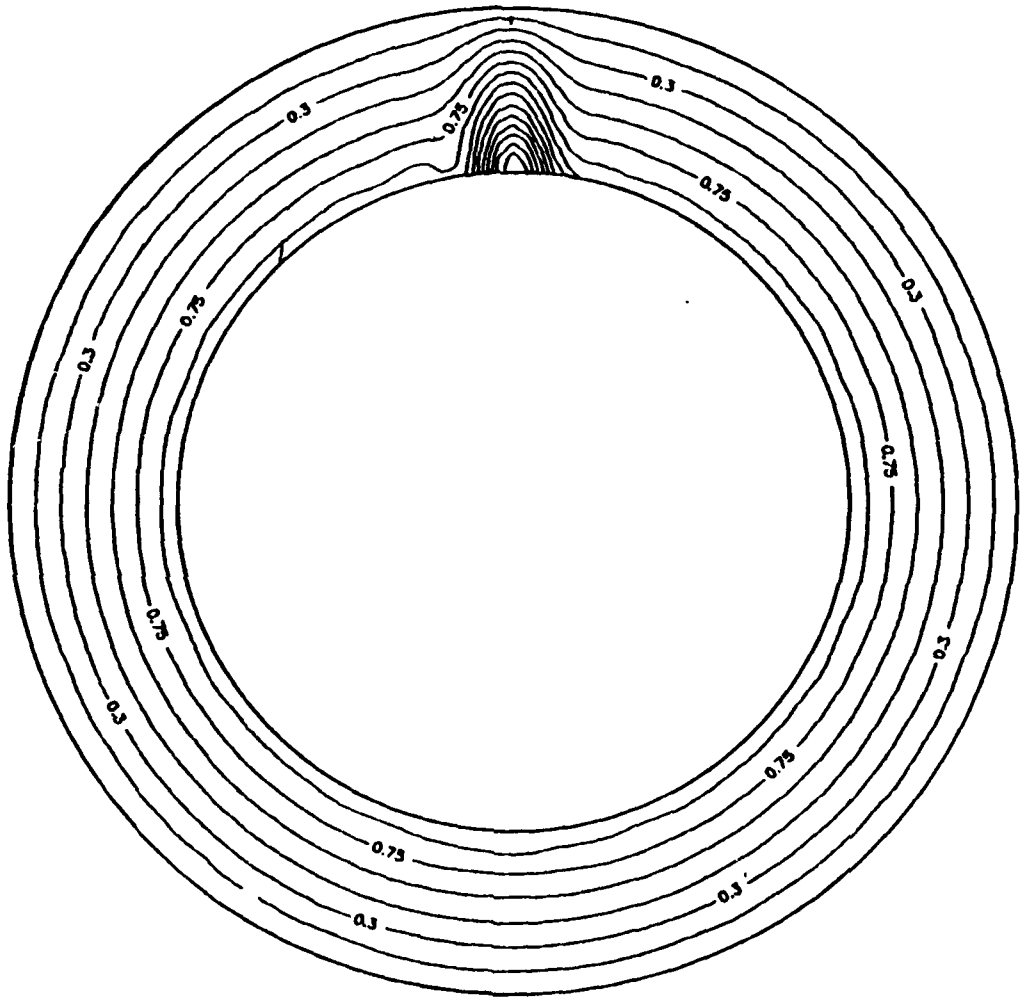


Figure A5a. Isotherms for the single hot spot condition

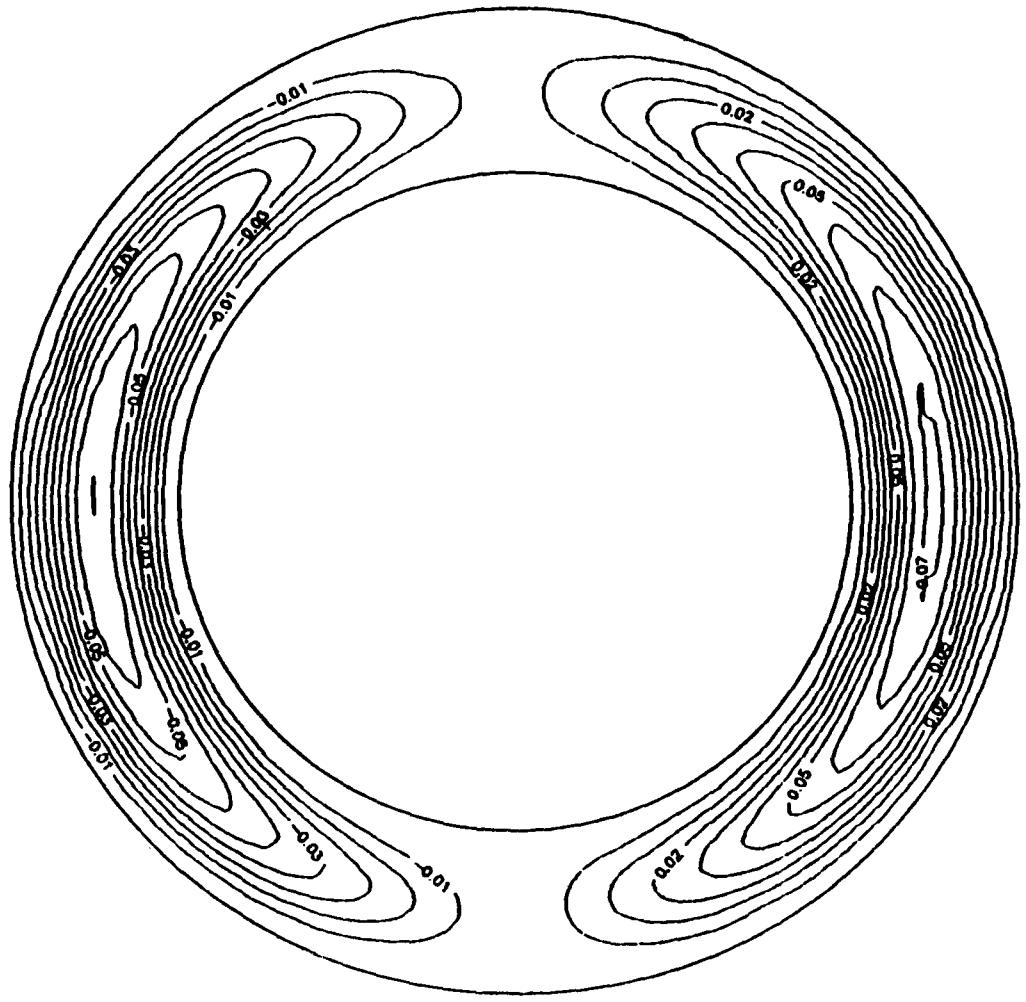


Figure A5b. Numerical streamlines for $\hat{G}$ = 3.0 for the single hot spot condition

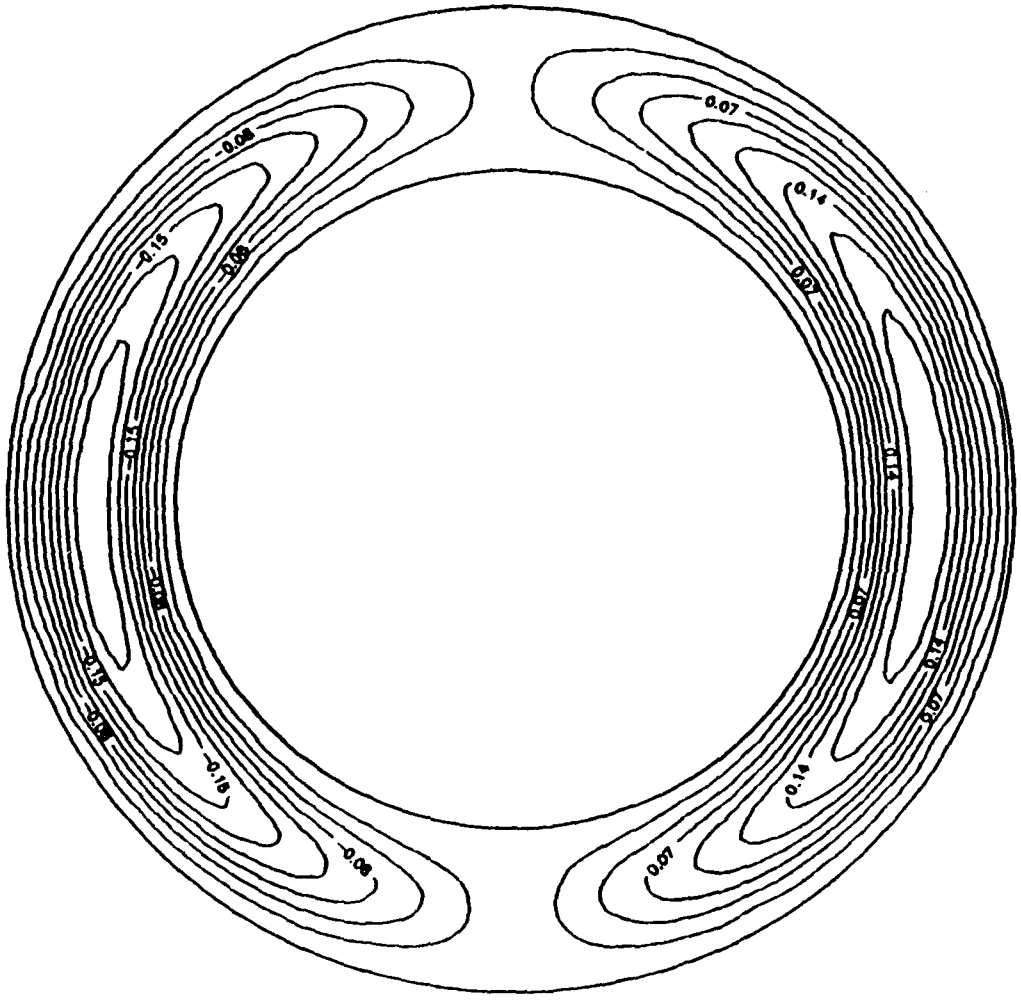


Figure A5c. Numerical streamlines for $\hat{G}$ = 4.40 for the single hot spot condition

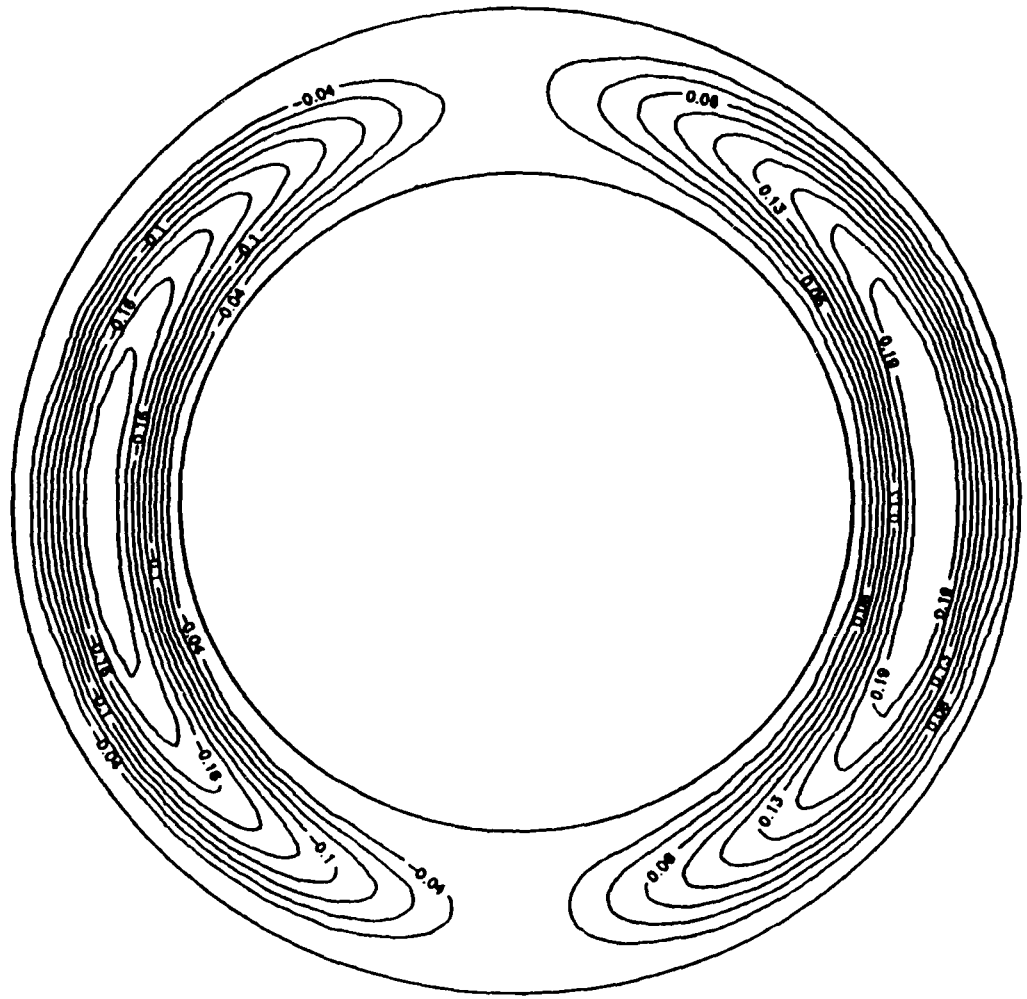


Figure A5d. Analytical streamlines for $\hat{G}$ = 4.40 for the single hot spot condition

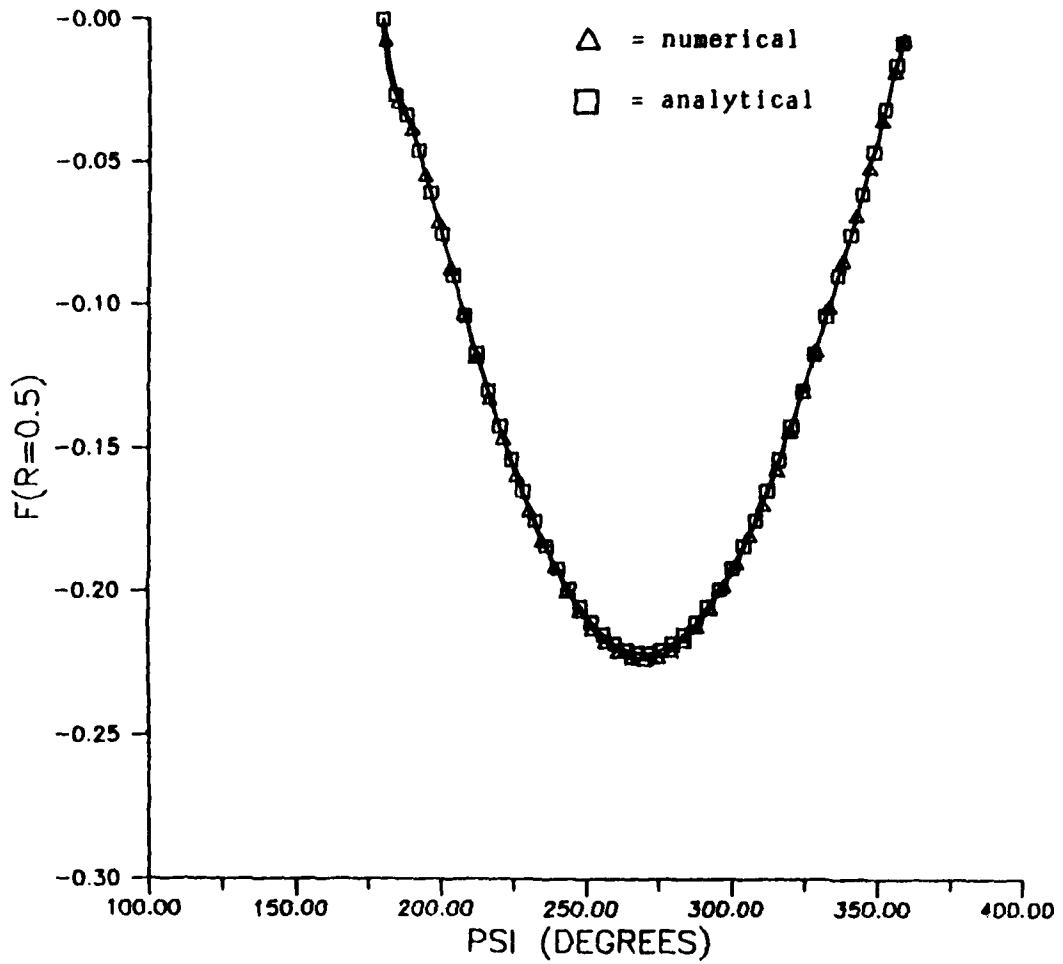


Figure A5e. Angular variation of the center-line stream function for $\hat{G}$ = 4.40 for the single hot spot condition

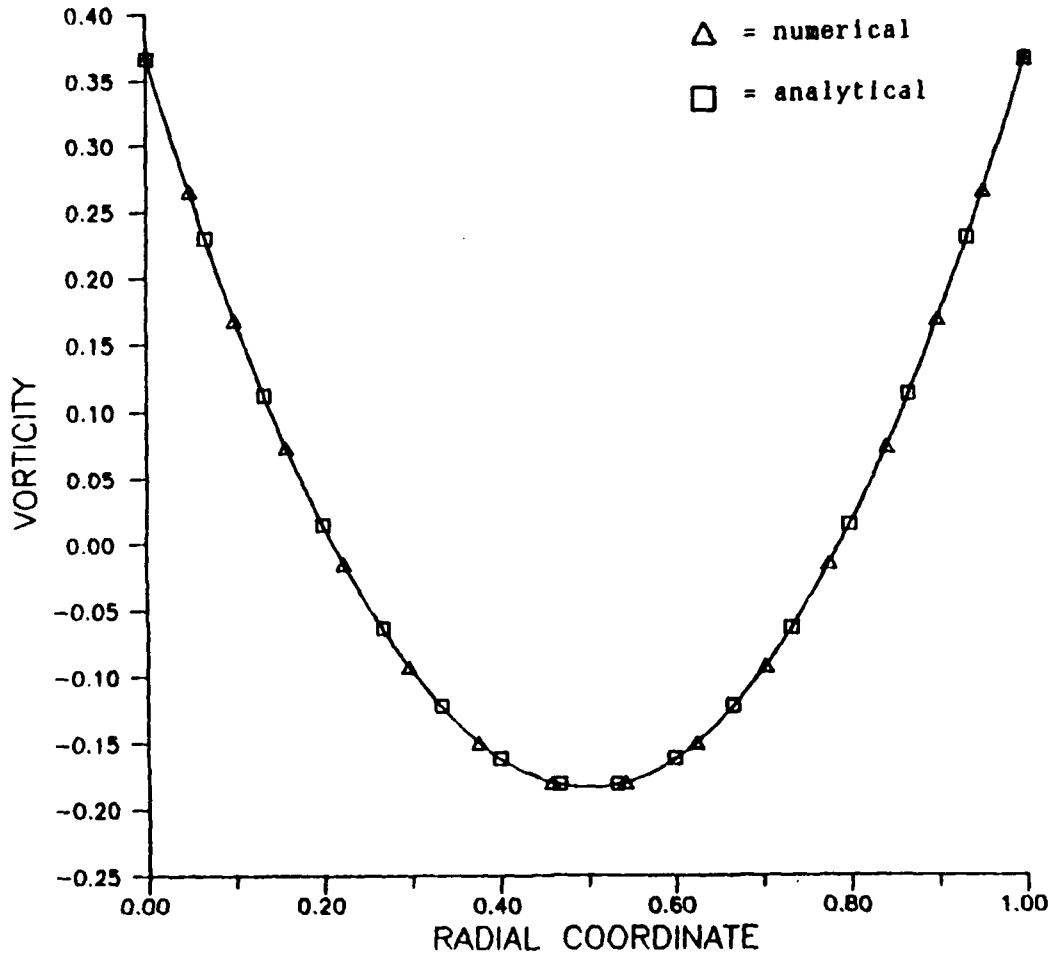


Figure A5f. Radial variation of vorticity at 90° for $\hat{G}$ = 4.40 for the single hot spot condition

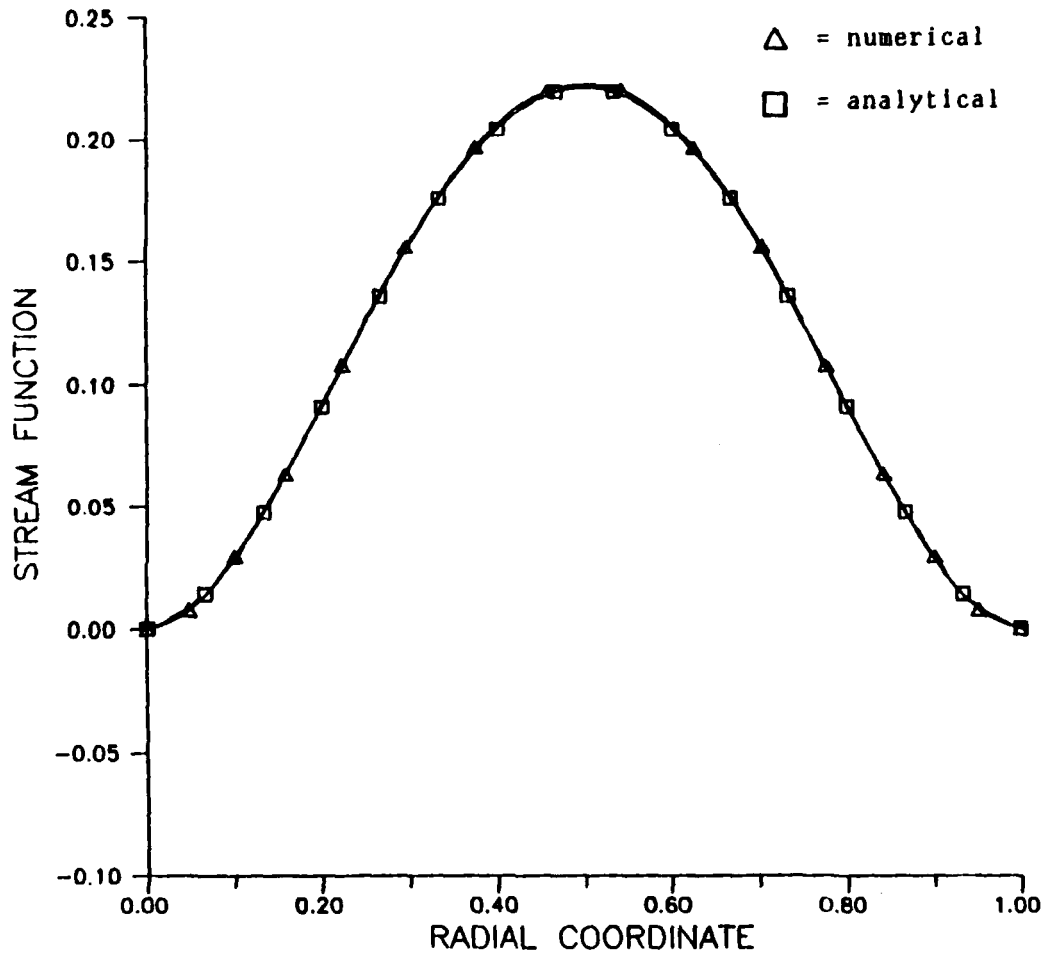


Figure A5g. Radial variation of the stream function at 90° for $\hat{G}$ = 4.40 for the single hot spot condition

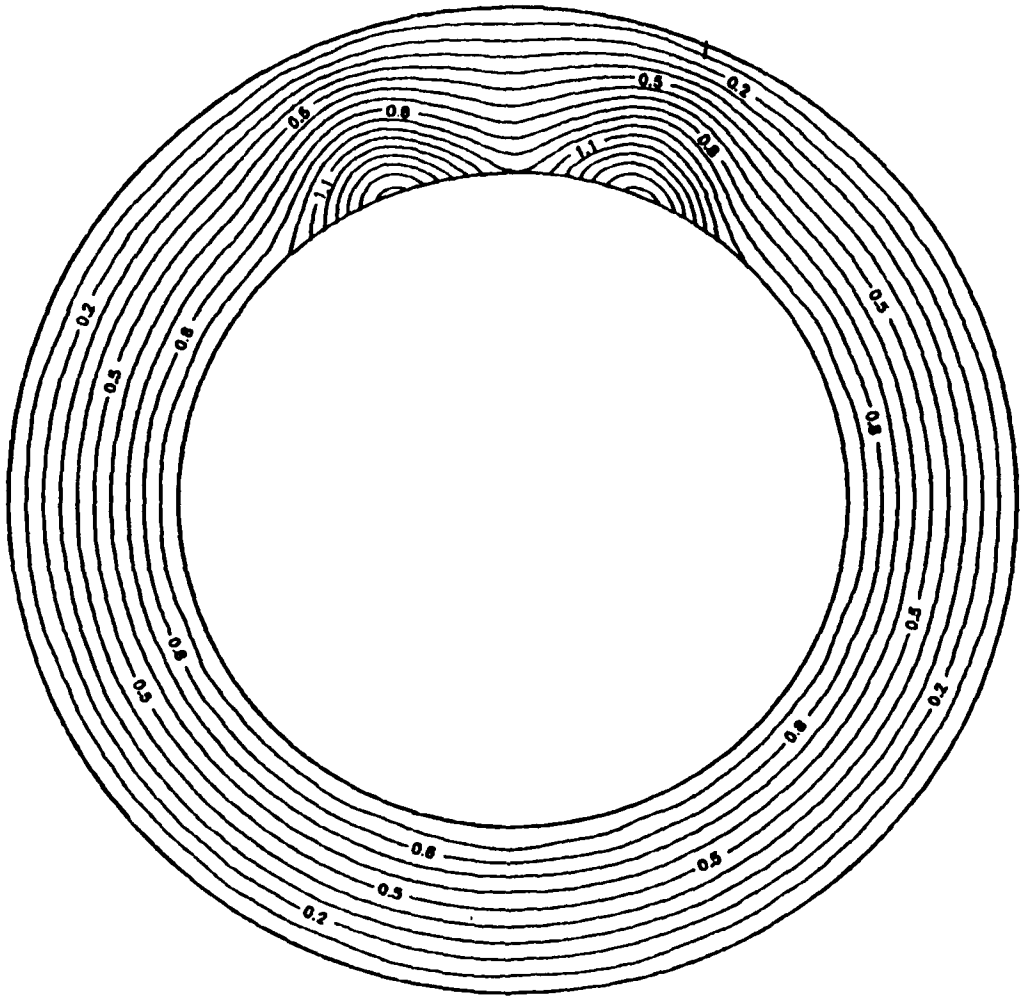


Figure A6a. Isotherms for the dual hot spot condition

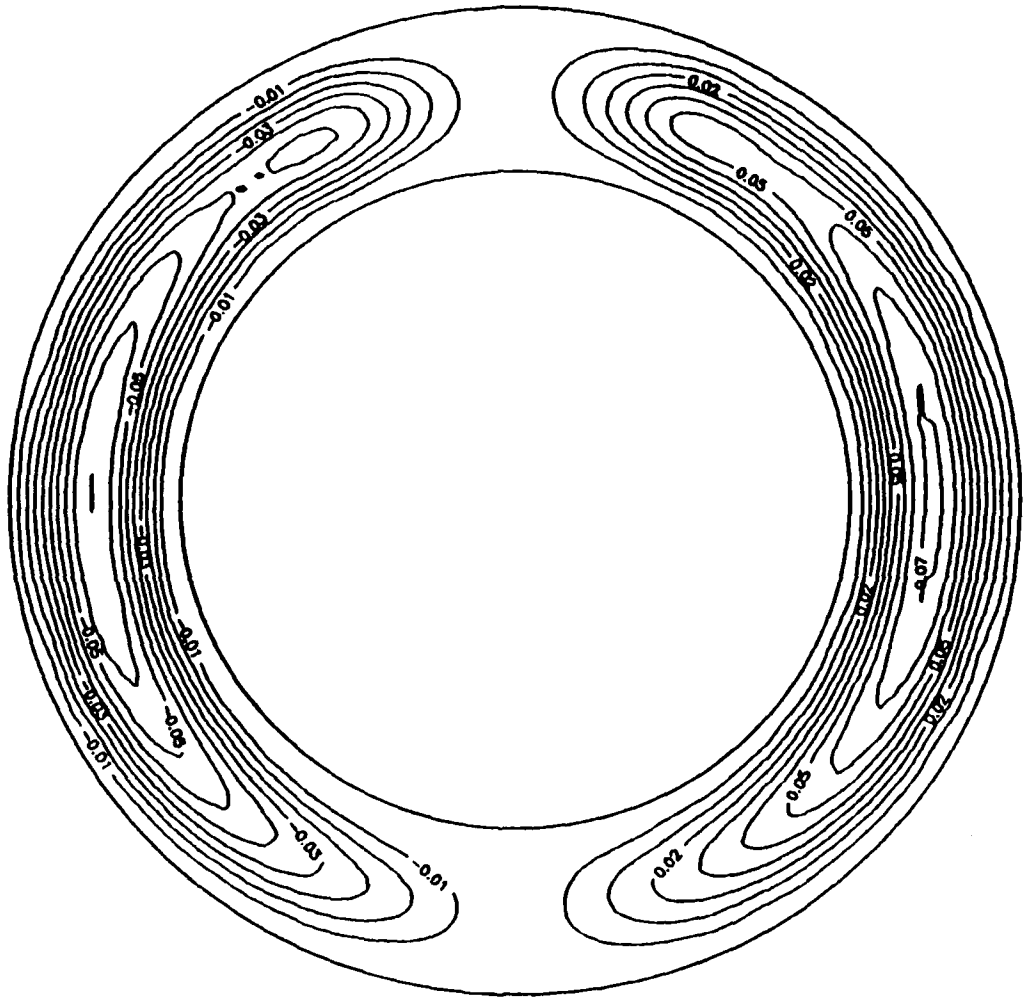


Figure A6b. Numerical streamlines for $\hat{G}$ = 3.0 for the dual hot spot condition

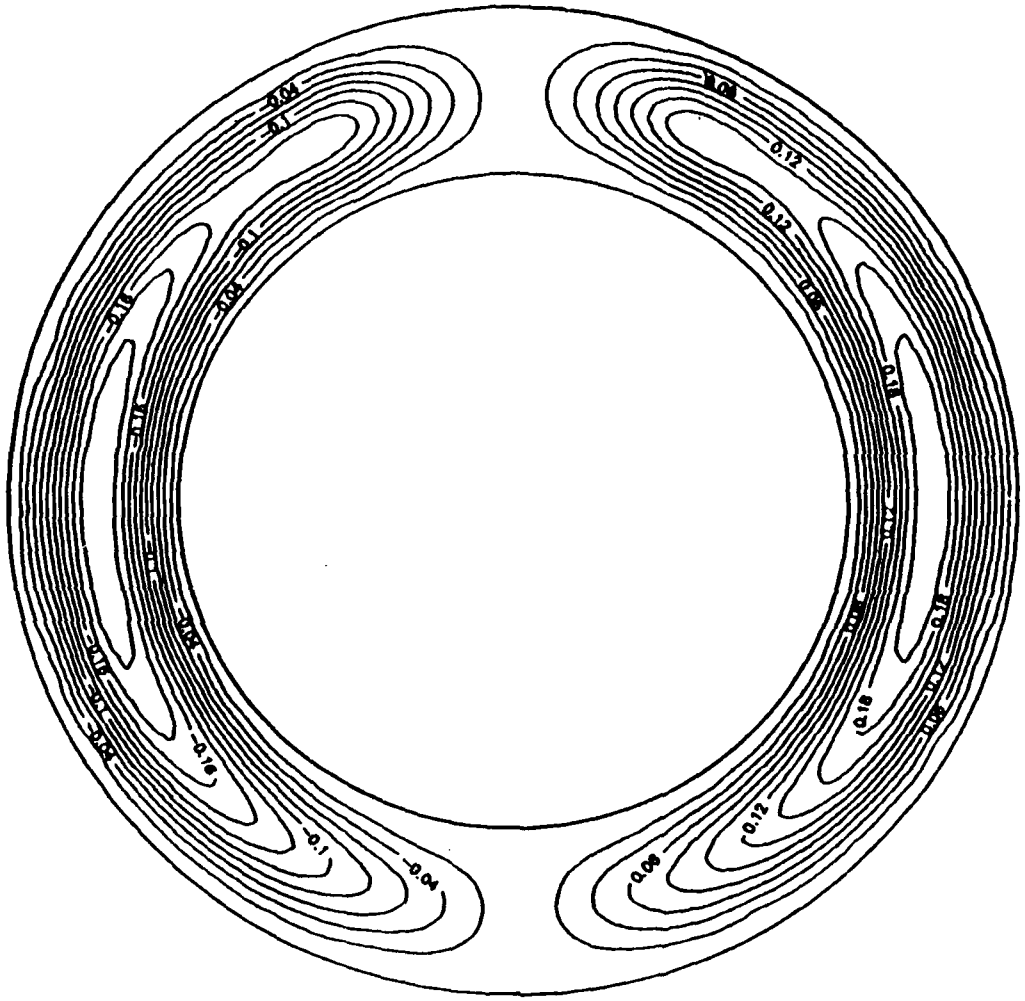


Figure A6c. Numerical streamlines for $\hat{G}$ = 4.40 for the dual hot spot condition

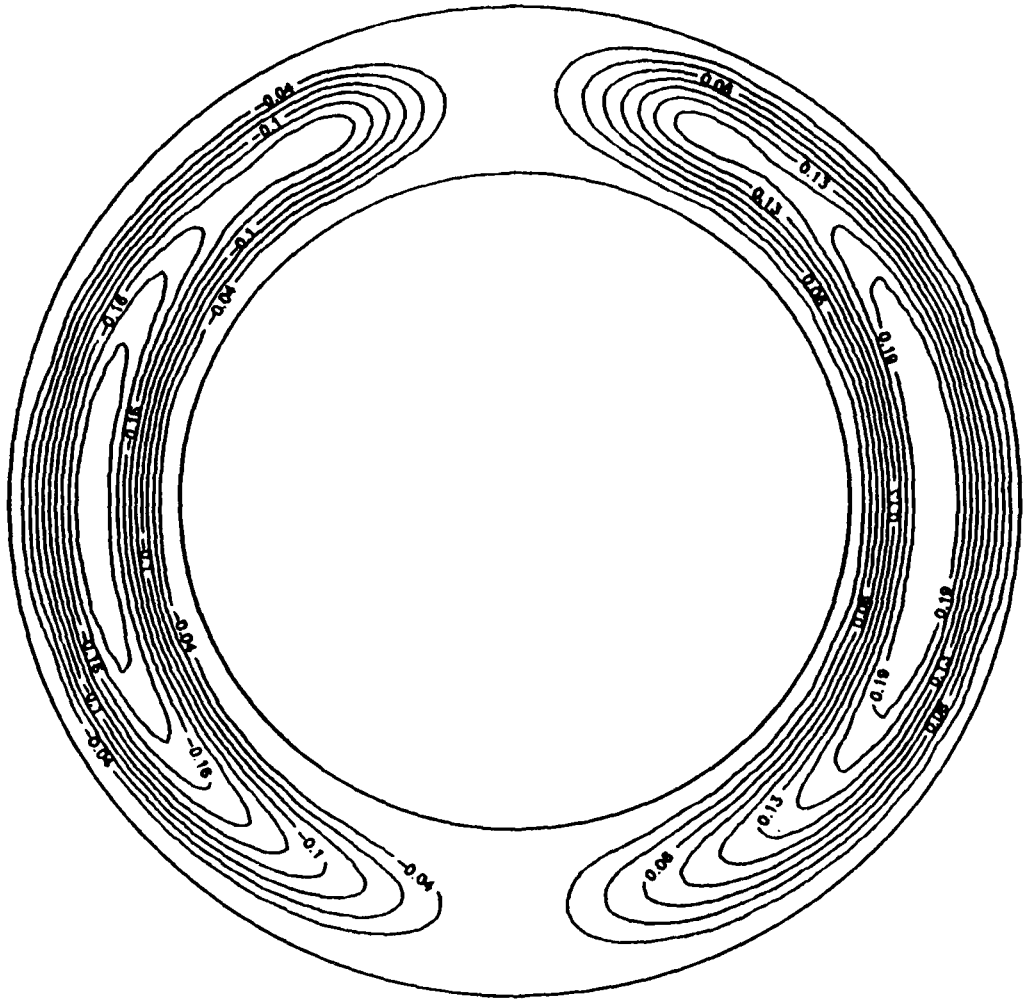


Figure A6d. Analytical streamlines for $\hat{G}$ = 4.40 for the dual hot spot condition

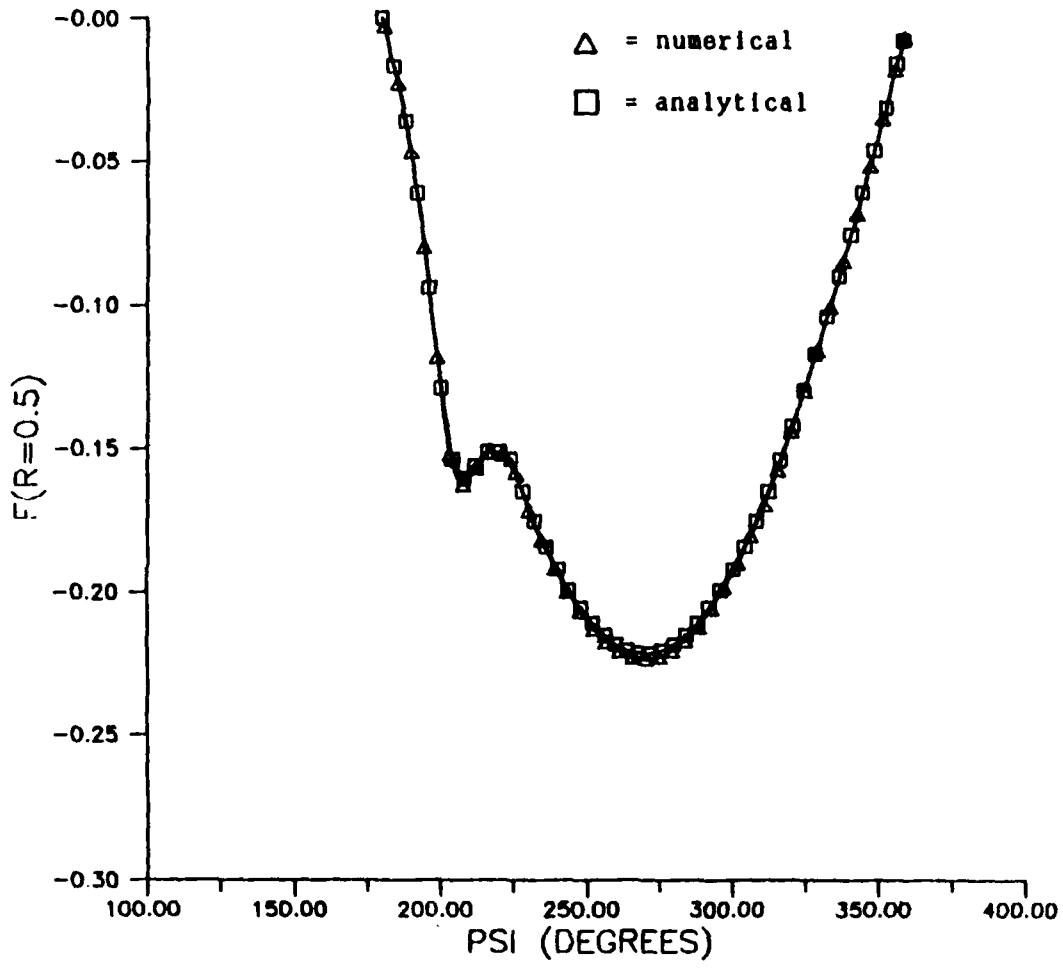


Figure A6e. Angular variation of the center-line stream function for $\hat{G}$ = 4.40 for the dual hot spot condition

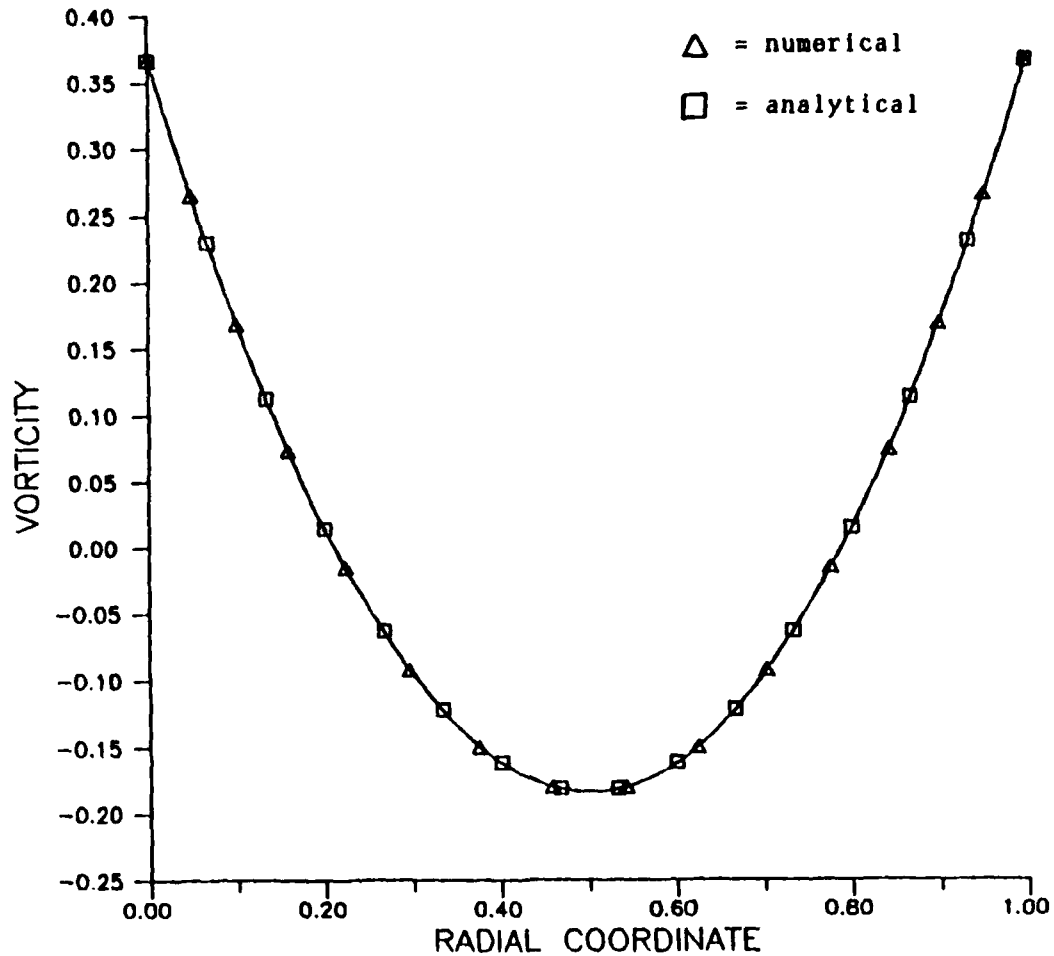


Figure A6f. Radial variation of vorticity at 90° for $\hat{G}$ = 4.40 for the dual hot spot condition

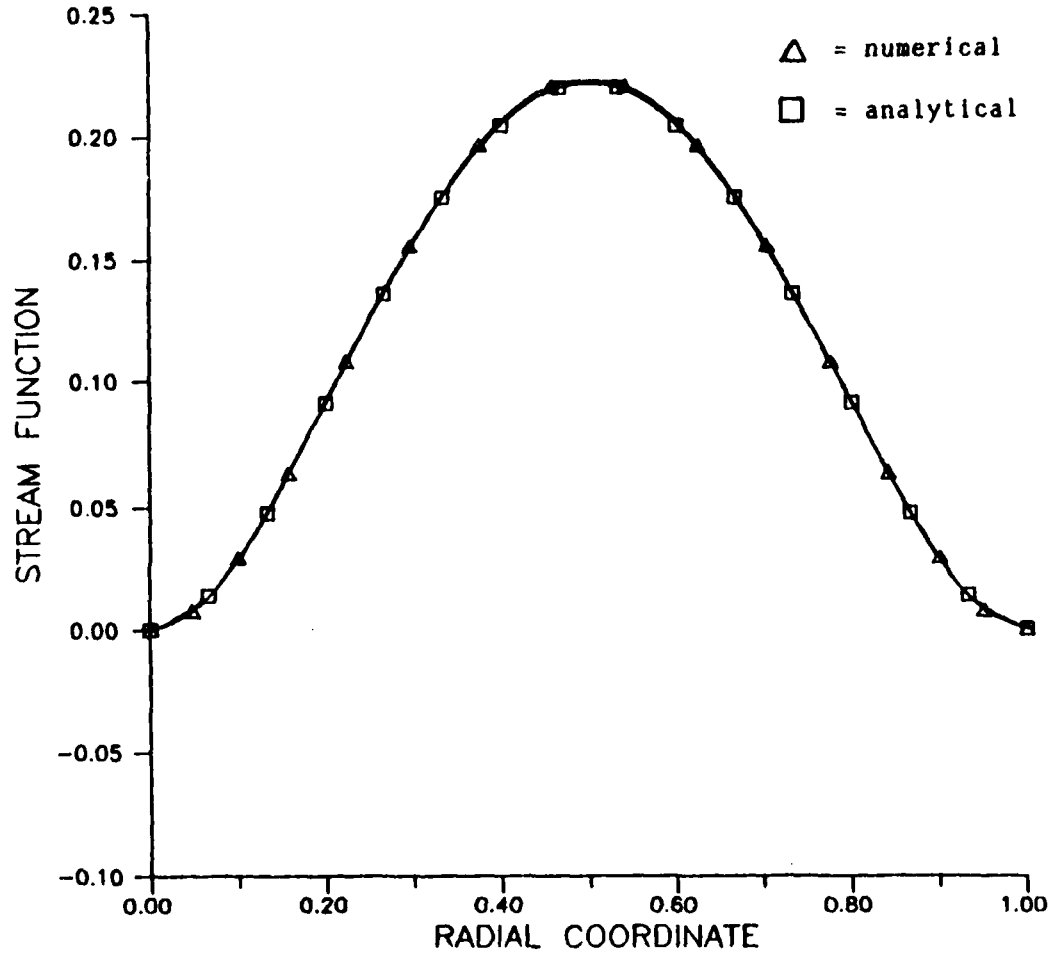


Figure A6g. Radial variation of the stream function at 90° for $\hat{G}$ = 4.40 for the dual hot spot condition
hot spot condition

## Bibliography


1. Anderson, R. and G. Lauriat. "The Horizontal Natural Convection Boundary Layer Regime in a Closed Cavity," Proceedings of the Eighth International Heat Transfer Conference, 4:1453-1458 (1986).

2. Chao, P., H. Ozoe and S. Churchill. "The effect of a Non-Uniform Surface Temperature on Laminar Natural Convection in aRectangular Enclosure," Chemical Engineering Communications, 9: 245-254 (1981).

3. Chappidi, P. R. and B. E. Eno. "Natural Convection in a Heated Parallel Plate Vertical Channel; Influence of Inlet Conditions," Proceedings of the 1988 National Heat Transfer Conference, 135-143. New York: American Society of Mechanical Engineers, New York, 1988.

4. Charrier-Mojtabi, M. C., A. Mojtabi and J. P. Caltagirone. "Numerical Solution of a Flow Due to Natural Convection in Horizontal Cylindrical Annulus," Journal of Heat Transfer, 101: 171-173 (February 1979).

5. Cheng, K. C. and J. Ou. "Convective Instability and Finite Amplitude Convection in the Thermal Entrance Region of Horizontal Rectangular Channels Heated from Below," Proceedings of the Seventh International Heat Transfer Conference, 2: 189-194 (1982).

6. Custer, J. R. and E. J. Shaughnessy. "Thermoconvective Mtion of Low Prandtl Number Fluids Within a Horizontal Cylindrical Annulus," Journal of Heat Transfer, 99: 596-602 (November 1977).

7. Date, A. W. "Numerical Prediction of Natural Convection Heat Transfer in Horizontal Annulus," International Journal of Heat Transfer, 29: 1457-1464 (1986).

8. Fant, D. B. "Unsteady Multicellular Natural Convection in a Narrow Horizontal Cylindrical Annulus," First National Fluid Dynamics Congress, Cincinnati: American Institute of Aeronautics and Astronautics, Ohio, July 25-28, 1988.

9. Farouk, B. and S. I. Guceri. "Laminar and Turbulent Natural Convection in the Annulus Between Horizontal Concentric Cylinders," Journal of Heat Transfer, 104: 631-636 (November 1982).

10. Fusegi, T. and B. Farouk. "A Three-Dimensional Study of Natural Convection in the Annulus Between Horizontal Concentric Cylinders," Proceedings of the Eighth International Heat Transfer Conference, 4: 1575-1579 (1986).

11. Giel, P. W. and F. W. Schmidt. "An Experimental Study of High Rayleigh Number Natural Convection in an Enclosure," Proceedings of the Eighth International Heat Transfer Conference, 4: 1459-1464 (1986).

12. Hung, Y. H. and S. W. Perng. "An Experimental Study of Local Steady-State Natural Convection in a Vertical Channel Heated on One Side Wall," Proceedings of the 1988 National Heat Transfer Conference, 2: 165-171. New York: The American Society of Mechanical Engineers, New York, 1988.

13. Karayiannis, T. G. and J. D. Tarasuk. "Natural Convection in an Inclined Rectangular Cavity With Different Thermal Boundary Conditions at the Top Plate," Journal of Heat Transfer, 110: 350-357 (May 1988).

14. Koster, J. N., U. Muller, C. Gunther and H. Frick. "Natural Convection in Vertical Gaps Heated at the Lower Side," Proceedings of the Seventh International Heat Transfer Conference, 2: 211-214. (1982).

15. Kuehn, T. H. and R. J. Goldstein. "An Experimental and Theoretical Study of Natural Convection in the Annulus Between Horizontal Concentric Cylinders," Journal of Fluid Mechanicals, 74: 695-719 (1976).

16. Kuehn, T. H. and R. J. Goldstein. "An Experimental Study of Natural Convection Heat Transfer in Concentric and Eccentric Horizontal Cylindrical Annuli," Journal of Heat Transfer, 100: 635-640 (November 1978).

17. Kuehn, T. H. and R. J. Goldstein. "A Parametric Study of Prandtl Number and Diameter Ratio Effects on Natural Convection Heat Transfer in Horizontal Cylindrical Annuli," Journal of Heat Transfer, 102: 768-770 (November 1980).

18. Kumar, R. "Study of Natural Convection in Horizontal Annuli," International Journal of Heat Transfer, 31: 1137-1148 (1988).

19. Kumar, R. "Experimental and Numerical Investigation of Natural Convective Flow in a Horizontal Cylindrical Annulus," Proceedings of the 1988 National Heat Transfer Conference, 2: 115-124. New York: The American Society of Mechanical Engineers, Texas, (1988).

20. Lee, S. and M. M. Yovanovich. "Laminar Natural Convection From a Vertical Plate with Variations in Surface Heat Flux," Proceedings of the 1988 National Heat Transfer Conference, 2: 197-205. New York: The American Society of Mechanical Engineers, Texas, (1988).

21. Lee, Y., S. A. Korpela and R. N. Horne. "Structure of Multicellular Natural Convection in a Tall Vertical Annulus," Proceedings of the Seventh International Heat Transfer Conference, 2: 221-226 (1982).

22. Mahony, D. N., R. Kumar and E. H. Bishop. "Numerical Investigation of Variable Property Effects on Laminar Natural Convection of Gases Between Two Horizontal Isothermal Concentric Cylinders," Journal of Heat Transfer, 108, 783-789 (November 1986).

23. Morcos, S. M. and M. M. M. Abou-Ellail. "Numerical Predictions of Flow and Heat Transfer in Emergency Cooling Systems of Gas-Cooled Nuclear Reactors," Proceedings of the 1988 National Heat Transfer Conference, 2: 229-236. New York: The American Society of Mechanical Engineers, New York (1988).

24. Nelson, J., R. Douglass and D. Alexander. "Natural Convection in a Spherical Annulus Filled with Heat Generating Fluid," Proceedings of the Seventh International Heat Transfer Conference, 2: 171-176 (1982).

25. Rao, Y., Y. Miki, K. Fukuda, Y. Takata and S. Hasegawa. "Flow Patterns of Natural Convection in Horizontal Cylindrical Annuli," International Journal of Heat and Mass Transfer, 28: 705-714 (1985).

26. Sun, R. and X. Zhang. "An Experimental Study of the Natural Convection Within the Horizontal Cylindrical Annular Enclosures," Proceedings of the Eighth International Heat Transfer Conference, 4: 1569-1574 (1986).

## Vita

Captain David L. Bennett was born on [redacted] He graduated from Springfield Shawnee High School in 1979 and attended the University of Cincinnati, from which he received the degree of Bachelor of Science in Aerospace in June 1984. Upon graduation, he received a commission in the USAF through OTS at Lackland AFB, Texas. He served as an escape systems engineer with the Deputy for Aeronautical Equipment of the Aeronautical Systems Division, WPAFB, Ohio, until entering the School of Engineering, Air Force Institute of Technology, in May 1987.

[redacted]

SECURITY CLASSIFICATION OF THIS PAGE

# REPORT DOCUMENTATION PAGE

Form Approved
OMB No. 0704-0188

| | |
|---|---|
| 1a. REPORT SECURITY CLASSIFICATION<br>UNCLASSIFIED | 1b. RESTRICTIVE MARKINGS<br>N/A |
| 2a. SECURITY CLASSIFICATION AUTHORITY | 3. DISTRIBUTION/AVAILABILITY OF REPORT<br>Approved for public release; distribution unlimited |
| 2b. DECLASSIFICATION/DOWNGRADING SCHEDULE | |
| 4. PERFORMING ORGANIZATION REPORT NUMBER(S)<br>AFIT/GAE/AA/88D-01 | 5. MONITORING ORGANIZATION REPORT NUMBER(S) |
| 6a. NAME OF PERFORMING ORGANIZATION<br>School of Engineering<br>6b. OFFICE SYMBOL (If applicable)<br>AFIT/ENY | 7a. NAME OF MONITORING ORGANIZATION |
| 6c. ADDRESS (City, State, and ZIP Code)<br>Air Force Institute of Technology<br>Wright-Patterson AFB, OH 45433 | 7b. ADDRESS (City, State, and ZIP Code) |
| 8a. NAME OF FUNDING/SPONSORING ORGANIZATION<br>8b. OFFICE SYMBOL (If applicable) | 9. PROCUREMENT INSTRUMENT IDENTIFICATION NUMBER |
| 8c. ADDRESS (City, State, and ZIP Code) | 10. SOURCE OF FUNDING NUMBERS<br>PROGRAM ELEMENT NO. / PROJECT NO. / TASK NO. / WORK UNIT ACCESSION NO. |

11. TITLE (Include Security Classification)
VARIABLE WALL TEMPERATURE EFFECTS ON MULTICELLULAR NATURAL CONVECTION IN A HORIZONTAL ANNULUS (UNCLASSIFIED)

12. PERSONAL AUTHOR(S)
Bennett, David Loren

| 13a. TYPE OF REPORT | 13b. TIME COVERED | 14. DATE OF REPORT (Year, Month, Day) | 15. PAGE COUNT |
|---|---|---|---|
| MS Thesis | FROM _____ TO _____ | 1988 December | 133 |

16. SUPPLEMENTARY NOTATION

| 17. COSATI CODES | | | 18. SUBJECT TERMS (Continue on reverse if necessary and identify by block number) |
|---|---|---|---|
| FIELD | GROUP | SUB-GROUP | Natural Convection, Horizontal Annulus, Variable Wall Temperature Effects |
| 20 | 13 | | |
| | | | |

19. ABSTRACT (Continue on reverse if necessary and identify by block number)

(See reverse.)

| | |
|---|---|
| 20. DISTRIBUTION/AVAILABILITY OF ABSTRACT<br>☒ UNCLASSIFIED/UNLIMITED ☐ SAME AS RPT. ☐ DTIC USERS | 21. ABSTRACT SECURITY CLASSIFICATION<br>UNCLASSIFIED |
| 22a. NAME OF RESPONSIBLE INDIVIDUAL<br>Capt Daniel B. Fant, Instructor, AFIT | 22b. TELEPHONE (Include Area Code) 513-255-3708<br>22c. OFFICE SYMBOL AFIT/ENY |

DD Form 1473, JUN 86 Previous editions are obsolete. SECURITY CLASSIFICATION OF THIS PAGE

## Abstract

The purpose of this study was to examine natural convection within a narrow horizontal annulus subject to variable inner cylinder temperature distributions. Both numerical and analytical approaches were taken in determining the effects of variable temperature conditions imposed on the inner cylinder in triggering or suppressing multicellular flow instabilities.

The two-dimensional Navier-Stokes equations are simplified into boundary-layer equations for the assumptions of large Rayleigh number, small annular gap, and small Prandtl number. These 2-D unsteady boundary-layer equations are discretized using finite-differencing techniques. Numerical solutions to these governing equations are then obtained by using a stable second-order, fully-implicit, time-accurate, Gauss-Siedel iterative procedure. In addition, analytical steady-state solutions to these simplified equations are obtained using perturbation methods. theses. (Mgm) ←

For most inner cylinder temperature distributions considered in the steady flow regime, these analytical results yield excellent agreement with numerical results. Although both schemes predict the formation of thermal-like instabilities induced by localized hot and cold spots in the horizontal annular regions, the analytical model failed to predict the steady-state multicellular hydrodynamic instabilities found numerically for the sin $\psi$ temperature distribution at $\hat{G} = 4.95$ in the vertical portions of the annulus. The analytical model also fails to capture unsteady multicellullar flow behavior found numerically for the sinusoidal temperature distribution at $\hat{G} = 4.99$.